Conjugate Heat Transfer Analysis of an Impingement/Effusion Cooled Combustor Liner

by
Matthew Jonathan Yoko

Thesis presented in partial fulfilment of the requirements for the degree of Master of Engineering (Mechanical) in the Faculty of Engineering at Stellenbosch University

Supervisor: Prof. S.J. van der Spuy
Co-supervisor: Dr V Sethi (Cranfield University)

March 2020

Declaration

By submitting this thesis electronically, I declare that the entirety of the work contained therein is my own, original work, that I am the sole author thereof (save to the extent explicitly otherwise stated), that reproduction and publication thereof by Stellenbosch University will not infringe any third party rights and that I have not previously in its entirety or in part submitted it for obtaining any qualification.

Date: March 2020

Abstract

Conjugate Heat Transfer Analysis of an Impingement/Effusion Cooled Combustor Liner

M.J. Yoko

Department of Mechanical and Mechatronic Engineering,
University of Stellenbosch,
Private Bag X1, Matieland 7602, South Africa.

Thesis: MEng (Mech)

March 2020

The design of gas turbine combustors is a costly, iterative process which is heavily reliant on empirical modelling. To facilitate the design of novel low emissions combustors, a multi-fidelity design process has been proposed. In this process, physics-based low order models are built; calibrated by high fidelity simulations and then used in multi-objective optimisation studies.

The current work contributes to this process by providing a method of performing high fidelity multiphysics simulations of an impingement/effusion cooling scheme for a combustor liner wall. A conjugate heat transfer CFD model was used to capture details of the combusting flow field and its interaction with the liner wall. While this method has been successfully applied to pure effusion cooling, it had not yet been used to study impingement/effusion cooling in a representative combustor. Further to this, the impact of radiation modelling was investigated as this had not been considered in previous work.

The method was validated against a simple experimental case study before being applied to a representative gas turbine combustor. It was shown that this method is capable of predicting impingement/effusion cooling performance to within 1% for a simple case. The combustor case study revealed a number of 3D effects which had not been captured by the low order model, most notably a strong interaction between the swirling flame and the cooling film. This informed recommendations for improvements to the low order model. It was further shown that radiative heat flux contributed up to 33% of the total flux, justifying the inclusion of radiation modelling in these studies. Finally, a strong sensitivity to the level of soot fouling was shown, with a potential doubling of radiative heat flux as a result. Further work is required to estimate the level of soot fouling on the liner walls, allowing the liner emissivity distribution to be more reliably constructed.

Uittreksel

Gekoppelde Warmte-Oordrag Analise van 'n Impak/Effusie Verkoelde Verbrander

("Conjugate Heat Transfer Analysis of an Impingement/Effusion Cooled Combustor Liner")

M.J. Yoko

Departement Meganiese en Megatroniese Ingenieurswese,
Universiteit van Stellenbosch,
Privaatsak X1, Matieland 7602, Suid Afrika.

Tesis: MIng (Meg)

Maart 2020

Om gasturbiene verbranders te ontwerp is 'n duur en iteratiewe proses wat afhanklik is van empiriese modellering. Die ontwerp van nuwe, lae emissie verbranders kan vergemaklik word deur 'n ontwerpsproses te volg wat op verskeie vlakke van akkuraatheid staat maak. Hierdie proses behels die ontwikkeling van lae orde fisika modelle, wat gekalibreer word met hoë akkuraatheid simulasies, en dan gebruik word in veeldoelige optimeringsstudies.

Die huidige werk dra by tot hierdie proses deur 'n metode vir hoë akkuraatheid multi-fisika simulasies van 'n impak/effusie verkoelingsskema van 'n verbrander voering te verskaf. Die besonderhede van die ontbrandende vloeiveld en dié se interaksie met die voering word vasgevang in 'n gekoppelde warmte-oordrag berekeningsvloeidinamika model. Hierdie metode is in die verlede reeds suksesvol gebruik om suiwer effusie verkoeling te bestudeer, maar is tot dusver nog nie gebruik om impak/effusie verkoeling in 'n verteenwoordigende verbrander te ondersoek nie.Die bydrae van straling word ook in die modelering ondersoek, wat nog nie voorheen bestudeer is nie.

Die geldigheid van die metode word bevestig deur dit te vergelyk met 'n eenvoudige eksperimentele gevallestudie voor dit op 'n verteenwoordigende gasturbiene verbrander aangewend word. Die huidige studie bewys dat hierdie metode die impak/effusie verkoelingsprestasie binne 1% kan voorspel vir 'n eenvoudige geval. Die verbrander gevallestudie bring verskeie 3D effekte wat nie in die lae orde model vasgevang word nie, aan die lig. Die merkwaardigste van hierdie effekte is 'n sterk interaksie tussen die kolkende vlam en die verkoelingsfilm. Hierdie waarnemings verskaf inligting ten einde aanbevelings te maak vir verbeteringe aan die lae orde model. Daar word verder gewys dat die stralings-warmtevloed

tot en met 33% van die totale warmtevloed bydrae, en dus is die insluiting van stralingsmodelering in hierdie studie geregverdig. Laastens word ‘n sterk sensitiwiteit vir roetneerslag aangedui, wat kan lei tot ‘n potensiële verdubbeling van die warmtevloed as gevolg van straling. ‘n Verdere ondersoek word benodig om die vlak van roetneerslag op die voering te beraam. So ‘n raming sal toelaat dat die emissiwiteit verspreiding van die voering meer betroubaar bereken kan word.

Acknowledgements

I owe a great debt of gratitude to many people and institutions who have supported me in this study. I would particularly like to give thanks to the following:

To ΔV Aerospace for providing funding and adjusting my work schedule to accommodate my studies. It is a privilege to work for an employer that provides the opportunity for further education.

To Hannes and my thermofluids colleagues at ΔV Aerospace. Thank you for all the encouragement and advice. Hannes, thank you for planting the seed and pushing me to take on this challenge, and for the mountains of support along the way.

To Prof van der Spuy, thank you so much for facilitating a study outside of your field of interest. Thank you for initiating and organising the collaboration with Cranfield - I'm sorry for the extra admin it incurred! Without you I am not sure this would have happened. Thank you for sharing your knowledge and wisdom, it has been a pleasure to study under you.

To Dr Sethi, Dr Sun and Prof Gauthier from Cranfield University, thank you for providing your valuable technical insight. Most importantly, thank you for opening your projects to me. You allowed me to complete my master's degree in a field that I love. Dr Sun, thank you especially for the extensive support you provided to me throughout this study.

To the CHPC and specifically Andrew Gill, thank you for your assistance in solving my rather large problem - and all the patience which came with it. I truly appreciate the special arrangements to get me the computational resources required. Without them I'd probably still be waiting for convergence.

Most importantly, to my wife Jess. Thank you for the patience and understanding in enduring this obsession. Thank you for sacrificing evenings, weekends and all the moments in between. Thank you for supporting me, encouraging me and making sure I ate. You kept me going.

Contents

Declaration i

Abstract ii

Uittreksel iii

Acknowledgements v

Contents vi

List of Figures viii

List of Tables xi

Nomenclature xii

1 Introduction 1
- 1.1 Background . . . 1
- 1.2 Motivation . . . 7
- 1.3 Research Objectives . . . 10
- 1.4 Summary . . . 10

2 Literature Review 11
- 2.1 Impingement/Effusion Cooling . . . 11
- 2.2 Conjugate Heat Transfer . . . 14
- 2.3 Radiation . . . 17
- 2.4 Summary . . . 20

3 Validation and Mesh Study 22
- 3.1 Experimental Case Study . . . 22
- 3.2 Benchmark Simulation . . . 25
- 3.3 Mesh Sensitivity Study . . . 32
- 3.4 Meshing Trade-off . . . 41

4 Representative Combustor Analysis 43
- 4.1 Geometry . . . 43
- 4.2 Mesh . . . 44
- 4.3 Boundary Conditions . . . 45

4.4 Material Properties 47
4.5 Solution 47
4.6 Results 49
4.7 Summary 57

5 Impact of Radiation Modelling 59
5.1 Boundary Conditions 59
5.2 Material Properties 60
5.3 Solution 61
5.4 Results 62
5.5 Summary 70

6 Conclusions & Recommendations 71
6.1 Conclusions 71
6.2 Future Work 73
6.3 Improvements to Low Order Model 75

Appendices 76

A Material Properties 77
A.1 Validation Study 77
A.2 Combustor Case Study 77

B Additional Plots 79

List of References 84

List of Figures

1.1 Generic 2D layout of combustor (Lefebvre and Ballal, 2010). 2
1.2 Range of suitable combustion temperatures for low emissions (Lefebvre and Ballal, 2010). 3
1.3 Adiabatic flame temperature curve. 4
1.4 Schematic of lean direct injection combustor (Crocker *et al.*, 2000). . 5
1.5 Effusion cooling configurations. 6
1.6 Impingement/effusion cooling. 6
1.7 Segment of combustor studied by Gent (2018) 9

2.1 Schematic of typical wind tunnel configuration for testing of impingement/effusion cooled plates (Xiao-ming *et al.*, 2015). 12
2.2 Transverse averages of cooling effectiveness at various Biot numbers, with and without impingement jets (Jung *et al.*, 2017). 13
2.3 Contours of cooling effectiveness in a representative LDI combustor (Andreini *et al.*, 2015*a*). 14
2.4 Source-based approximation to effusion cooling in a CHT CFD simulation (Andreini *et al.*, 2013). 15
2.5 Local overall cooling effectiveness at y/d=1.5 using various turbulence models (Liu *et al.*, 2018). 17
2.6 Circumferentially averaged temperature distribution with and without radiation modelling (Saygin *et al.*, 2016). 20

3.1 Schematic of setup used by (Jung *et al.*, 2017). 23
3.2 Transverse averages of cooling effectiveness vs non-dimensional axial distance. 25
3.3 Contours of cooling effectiveness on a portion of the effusion plate (Jung *et al.*, 2017). 25
3.4 Single periodic repeat of CFD geometry. 26
3.5 Comparison of transverse averaged cooling effectiveness for different plate edge boundary conditions. 28
3.6 Comparison of transverse averaged cooling effectiveness from single sector and three sector meshes. 28
3.7 Contours of cooling effectiveness from single sector (a) and three sector (b) meshes. 29
3.8 Contours of cooling effectiveness from experimental study (above colour scale)(Jung *et al.*, 2017) and benchmark CFD (below colour scale). . 29

3.9 Typical blending function employed in the EWT approach. 31
3.10 Comparison of transverse averaged cooling effectiveness for turbulence closures. 31
3.11 Contours of cooling effectiveness from experimental study (above colour scale)(Jung *et al.*, 2017) and CFD using Realizable k-ε (below colour scale). 32
3.12 Comparison of meshes with and without inflation layers. 33
3.13 Comparison of transverse averaged cooling effectiveness with and without an inflation layer. 33
3.14 Comparison of meshes used in hole resolution sensitivity study. 34
3.15 Comparison of transverse averaged cooling effectiveness for various hole resolutions 35
3.16 Near-wall velocity profiles for three meshes, at three non-dimensional axial positions on the discharge side of the effusion plate. 35
3.17 Contours of normalised vorticity through the mid-plane. 37
3.18 Isosurface of Q-criterion, arbitrary colouring for clarity (top). Contours of normalised Nusselt number on suction side of effusion plate (bottom). 37
3.19 Comparison of polyhedral meshes with and without inflation layers. . 38
3.20 Comparison of polyhedral meshes used in hole resolution sensitivity study. 38
3.21 Comparison of transverse averaged cooling effectiveness for polyhedral mesh with and without inflation layer. 39
3.22 Comparison of transverse averaged cooling effectiveness for polyhedral meshes with various hole resolutions. 39
3.23 Near-wall velocity profiles for three meshes, at three non-dimensional axial positions on the discharge side of the effusion plate. 40
3.24 Contours of cooling effectiveness from experimental study (above colour scale)(Jung *et al.*, 2017) and CFD with source/sink approach (below colour scale). 41
3.25 Relative time to convergence vs temperature prediction error for various meshes. 42

4.1 Geometry of combustor to be studied. 44
4.2 Cross section of mesh with locations of bodies of influence highlighted. 45
4.3 Detail of the combustor case study mesh showing the impact of gap resolution. 46
4.4 Locations used for reporting combustor simulation results. 49
4.5 Combustion characteristics of the combustor under consideration. . . 50
4.6 Velocity vectors on combustor mid-plane. 51
4.7 Line integral convolution of near wall velocity. 52
4.8 Contours of absolute total pressure on the combustor mid-plane. . . . 53
4.9 Temperature contours on the discharge side of the effusion wall. . . . 54
4.10 Effusion wall heat flux. 55
4.11 Circumferentially averaged temperature on the discharge side of the effusion wall. 55

4.12 Impingement wall temperature and heat flux. 57

5.1 Angular coordinate convention used in the DO model. 61
5.2 Contours of volumetric emitted radiation on the combustor mid-plane. 63
5.3 Temperature contours on the discharge side of the effusion wall with and without radiation modelling. 64
5.4 Radiative heat flux through the effusion wall. 65
5.5 Circumferentially averaged temperature on the discharge side of the effusion wall showing impact of radiation modelling. 66
5.6 Temperature contours on the discharge side of the effusion wall with coarse radiation modelling and soot fouled walls. 67
5.7 Absorbed radiative heat flux contours on the discharge side of the effusion wall with coarse radiation modelling and soot fouled walls. . 67
5.8 Circumferentially averaged temperature on the discharge side of the effusion wall showing sensitivity to liner emissivity. 68
5.9 Temperature contours on the discharge side of the effusion wall with fine radiation modelling and soot covered walls. 69
5.10 Radiative heat flux contours on the discharge side of the effusion wall with fine radiation modelling and soot covered walls. 69
5.11 Circumferentially averaged temperature on the discharge side of the effusion wall showing sensitivity to DO discretisation. 70

B.1 Circumferentially averaged thermodynamic quantities on the suction side of the impingement wall. 80
B.2 Circumferentially averaged thermodynamic quantities on the discharge side of the impingement wall. 81
B.3 Circumferentially averaged thermodynamic quantities on the suction side of the effusion wall. 82
B.4 Circumferentially averaged thermodynamic quantities on the discharge side of the effusion wall. 83

List of Tables

3.1 Geometric parameters of experimental case 23
3.2 Test conditions of experimental case (Jung *et al.*, 2017) 24
3.3 Summary of results from hole resolution sensitivity study 36
3.4 Summary of results from polyhedral hole resolution sensitivity study 40

5.1 Summary of computational requirements for radiation modelling. . . 62

A.1 Material properties of AISI 304 77
A.2 Summary of combustion gas material modelling 77
A.3 Temperature dependent material properties of Haselloy X 78

Nomenclature

Abbreviations

BSL	Baseline (k-ω adaption)
CFD	Computational fluid dynamics
CHPC	Centre for High Performance Computing
CHT	Conjugate heat transfer
CO_2	Carbon dioxide
CO	Carbon monoxide
DO	Discrete ordinates
EWT	Enhanced Wall Treatment
FEA	Finite element analysis
FGM	Flamelet generated manifold
H_2O	Water / water vapour
LDI	Lean direct injection
LES	Large eddy simulation
MSE	Mean square error
NO_x	Oxides of nitrogen
NREC	Northern Research and Engineering Corporation
PM	Particulate matter
ppmv	Parts per million by volume
RANS	Reynolds averaged Navier-Stokes
RNG	Re-normalisation group (k-ε adaption)
RTE	Radiative transfer equation
SAS	Scale adaptive simulation
SO_x	Oxides of sulphur
SSG	Speziale, Sarkar and Gatski (Reynolds stress model adaption)
SST	Shear stress transport (k-ω adaption)
UDF	User Defined Function
UHC	Unburned hydrocarbons
WSGG	Weighted-sum-of-grey-gasses

Variables

A	Area	$[\,\mathrm{m}^2\,]$
Bi	Biot Number	$[\,-\,]$
a_k	WSGG weighting factor	$[\,-\,]$
C_p	Specific heat	$[\,\mathrm{J\,kg^{-1}\,K^{-1}}\,]$
d	Hole diameter	$[\,\mathrm{m}\,]$
H	Hole length / Plate gap	$[\,\mathrm{m}\,]$
I	Radiative intensity	$[\,\mathrm{W\,sr^{-1}\,Hz^{-1}}\,]$
L	Hole length	$[\,\mathrm{m}\,]$
M	Blowing ratio	$[\,-\,]$
P	Hole pitch	$[\,\mathrm{m}\,]$
$\dot{q}$	Heat flux	$[\,\mathrm{W\,m^{-2}}\,]$
s	Path length	$[\,\mathrm{m}\,]$
S	Hole spacing	$[\,\mathrm{m}\,]$
t	Plate thickness	$[\,\mathrm{m}\,]$
T	Temperature	$[\,\mathrm{K}\,]$
U	Velocity	$[\,\mathrm{m\,s^{-1}}\,]$
w_j	DO weighting factor	$[\,-\,]$
x	Axial distance along plate	$[\,\mathrm{m}\,]$
y^+	Non-dimensional wall distance	$[\,-\,]$
z	Plate gap	$[\,\mathrm{m}\,]$
α	Absorptivity	$[\,-\,]$
β	Extinction coefficient	$[\,\mathrm{m^{-1}}\,]$
ΔP	Pressure Drop	$[\,\%\,]$
ε	Emissivity	$[\,-\,]$
κ	Absorption coefficient	$[\,\mathrm{m^{-1}}\,]$
λ	Blending function	$[\,-\,]$
ρ	Density	$[\,\mathrm{kg\,m^{-3}}\,]$
σ_s	Scattering coefficient	$[\,\mathrm{m^{-1}}\,]$
Φ	Scattering phase function	$[\,-\,]$
ϕ	Cooling effectiveness / equivalence ratio	$[\,-\,]$
ψ	Generic quantity	$[\,-\,]$
Ω	Solid angle	$[\,\mathrm{sr}\,]$

Vectors

$\vec{r}$	Position vector
$\hat{s}$	Unit direction vector

Subscripts

b	Black body conditions
c	Coolant conditions
i, j	Indices in DO model
k	Index in WSGG model
m	Mainstream conditions
w	Wall conditions

Chapter 1

Introduction

This chapter aims to provide background information to the project. This includes brief primers on gas turbine combustors, their emissions and how these are being addressed through novel designs. Advanced cooling methods are briefly introduced, followed by a description of the conjugate heat transfer method of cooling analysis.

In addition to this, the motivation for the research is provided. The current study falls under a larger group of work being conducted at Cranfield University. The context of the current work within this group is provided.

Finally, the objectives of the research are outlined.

1.1 Background

Combustor Anatomy[1]

The gas turbine combustor is essentially a reaction vessel in which a fuel is burned in order to energise a gas stream. A portion of this energy is then utilised to sustain the cycle, with any surplus energy being extracted for useful work or thrust.

There are currently numerous combustor designs and configurations, each tailored to their application. Here the most common configuration for aero-engine combustors - the annular combustor with a perforated liner - is briefly described as an introduction to the anatomy of a combustor. The typical layout of such a combustor is shown in Figure 1.1. The combustor is defined by four main components: the diffuser, inner and outer casings, and the liner (or flame tube).

Air from the compressor is guided through the diffuser, which reduces flow velocity in order to minimise pressure loss. The diffused air is then incrementally introduced into the liner, inside which the combustion process takes place. The air is introduced through a variety of hole types at different axial locations. These

[1] It should be noted that this discussion of combustor anatomy is a condensed and modified extract from work previously submitted by the author as part of a subject on gas turbine combustion.

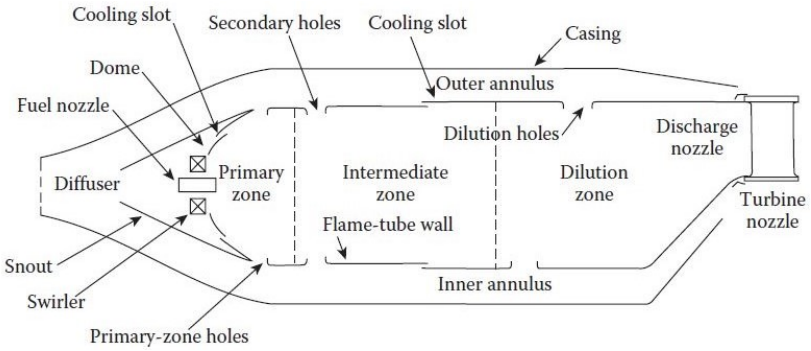

Figure 1.1: Generic 2D layout of combustor (Lefebvre and Ballal, 2010).

are sized and positioned in such a way as to stabilise and control the combustion process, as well as cool the liner and tailor the outlet temperature profile.

The combusting region contained within the liner is separated into three zones: the primary, intermediate and dilution zones, as shown in Figure 1.1. These zones must each fulfil a specific role in order for the entire combustor to meet its performance requirements.

The primary zone is responsible for providing ideal conditions for stable, self-sustained combustion. The conditions must be such that incoming fuel is rapidly vaporised, mixed with air and combusted to near-completion. This requires high temperatures (often up to 2500 K), good mixing and sufficient volume. The requirement for a stable, self-igniting flame is typically achieved through flow-recirculation in the primary zone. This anchors the flame by continuously drawing a portion of the combusting mixture back towards the fuel injector, reigniting the fresh air-fuel mixture (Saravanamuttoo *et al.*, 2006).

The air introduced in the intermediate zone allows for the combustion reaction to be brought to completion. This is usually not possible in the primary zone due to insufficient oxygen or mixing (NREC, 1980). The reaction must be complete by the end of the intermediate zone for effective operation of the dilution zone. Care must be taken in intermediate zone design, as the incoming cold air can cause flame quenching (Saravanamuttoo *et al.*, 2006). This would result in unburned fuel and intermediate reactants leaving the engine, significantly reducing efficiency and increasing pollutant emissions.

The dilution zone is responsible for bringing the overall outlet temperature down to a level acceptable for the turbine. Thorough mixing is essential in the dilution zone in order to avoid an uneven outlet temperature distribution, as local hotspots can significantly reduce turbine life. With careful design, the dilution zone air addition can be used to tailor the outlet profile in order to maximise turbine life.

Combustion Emissions

The intention of this section is a brief primer on combustion emissions. For more detail, the reader is referred to Lefebvre and Ballal (2010), Warnatz *et al.* (2006) and Kuo (2005).

The major gas turbine combustion emissions are carbon dioxide (CO_2), water vapour (H_2O), carbon monoxide (CO), particulate matter (PM, primarily smoke and soot), unburned hydrocarbons (UHC), oxides of sulphur (SO_x) and oxides of nitrogen (NO_x). CO_2 and H_2O are products of ideal combustion, and as such can only be reduced by minimising fuel burn. Good control over CO, PM and UHC formation has already been attained through careful design of the primary zone and liner cooling. SO_x formation is dependent on sulphur levels in the fuel and can therefore not be reduced by combustor design activities. NO_x emissions have historically been the most challenging to control and are therefore the main focus of current emissions reduction targets.

NO_x are formed through four main mechanisms: thermal NO_x, the nitrous oxide mechanism, prompt NO_x and fuel NO_x. Thermal NO_x formation is the most significant for the current work and will therefore be described briefly.

At high temperatures, atmospheric nitrogen begins to oxidise and form NO which further oxidises to NO_2. This endothermic reaction occurs more rapidly as temperature increases. A combustor will produce significant amounts of NO_x when the reaction time is in the same order as combustor residence time. Lefebvre and Ballal (2010) have stated that this typically occurs at around 1850 K. The obvious solution to NO_x emissions is therefore reduction of combustion temperatures, particularly in the hot primary zone. This is met by a number of challenges such as a reduction in stability, ignition problems, thermo-acoustic problems and, most annoyingly, an increase in other pollutant emissions. This particular problem gives the designer a narrow window of suitable flame temperatures to work within, as shown in Figure 1.2.

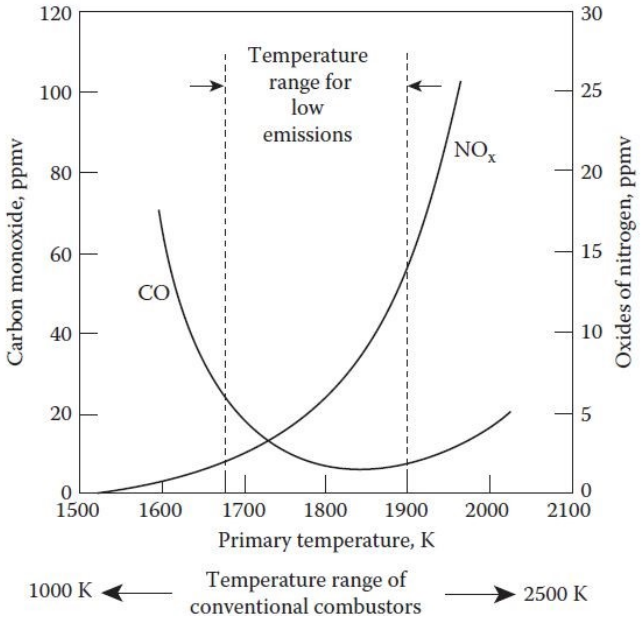

Figure 1.2: Range of suitable combustion temperatures for low emissions (Lefebvre and Ballal, 2010).

Low Emissions Combustors

A number of combustor configurations have been proposed to control flame temperatures and thereby reduce NO_x emissions. These can be generally categorised as rich dome and lean throughout.

Rich dome designs exploit the shape of the adiabatic flame temperature rise curve, as illustrated in Figure 1.3. Combustion temperatures are kept low by maintaining a fuel-rich primary zone, then rapidly and thoroughly mixing sufficient air to transition directly to lean combustion. These combustors are similar to those shown in Figure 1.1, in that air is added incrementally at different axial locations.

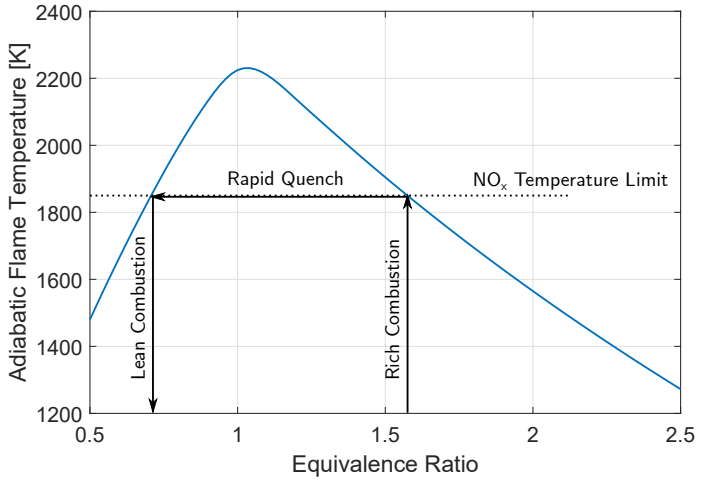

Figure 1.3: Adiabatic flame temperature curve.

Lean throughout designs avoid the fuel rich primary zone and limit temperature by maintaining fully lean combustion. These combustors admit almost all of the air into the combustor dome, except that used for liner cooling. As such, lean throughout designs do not have primary, secondary and dilution zones. There are a number of lean throughout concepts, but the focus of this research is the lean direct injection (LDI) combustor, so this will be described further.

Lean Direct Injection

LDI combustors admit 60-70% of the air through the swirler in order to ensure lean combustion throughout. The remaining air is typically required for liner cooling, leaving no air for dilution. As such, LDI combustors typically have no air admission holes other than the swirler. One possible LDI configuration is shown in Figure 1.4. Fuel is admitted through a pilot atomiser (202) for stability at low power settings. A simplex pressure atomiser is typically used for this. At higher power settings, additional fuel is admitted through the main injector (210), which is typically an air-blast atomiser. The ratio of pilot to main fuel varies throughout operation and peaks at 10%:90% at the maximum power setting. Air

is admitted through three vaned swirlers (204, 208 and 212). These produce the necessary shear for droplet breakup and rapid air and fuel mixing, as well as vortex breakdown leading to large scale recirculation for flame stability.

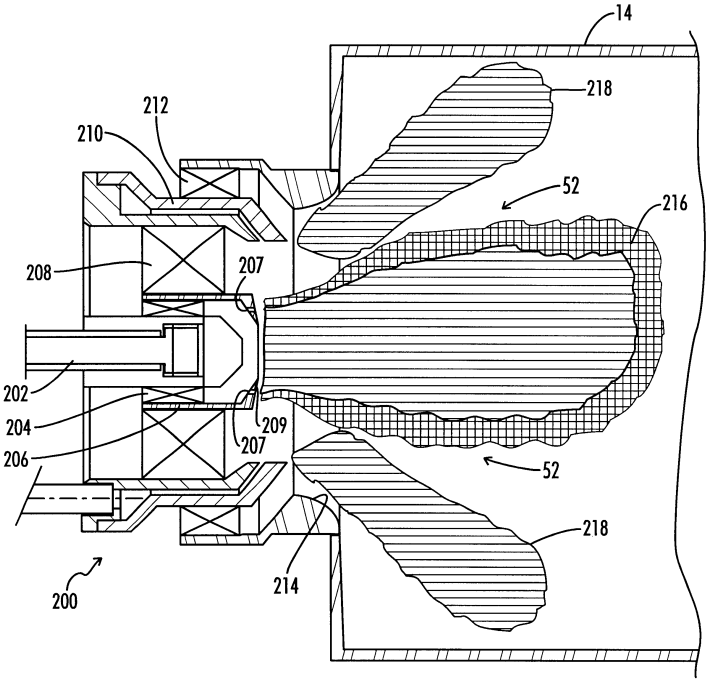

Figure 1.4: Schematic of lean direct injection combustor (Crocker *et al.*, 2000).

The pilot flame (216) burns near stoichiometric immediately downstream of the injector. This widens stability limits at the expense of some NO_x production, but this is not significant as only 10% of the total fuel flow is admitted through the pilot injector at full power. With downstream progression, the pilot flame is quickly leaned out by the air admitted through the inner main swirler (208). This limits the stoichiometric combustion, and therefore NO_x production, to a very small region near the pilot injector. The main flame (218) burns entirely lean, apart from localised regions of stoichiometric combustion which are characteristic of diffusion flames. These can be minimised by designing the injector and swirler for rapid evaporation and thorough mixing.

The ever-increasing requirement for lean combustion has led to very little air being available for liner cooling. This has dictated the development of advanced cooling methods. The two most relevant to this work, effusion and impingement/effusion cooling, will be described briefly.

Effusion Cooling

Effusion cooling involves perforating the liner wall with many small, evenly spaced holes. This is illustrated in Figure 1.5a. Each hole admits a small amount of cool air through the liner with minimal jet penetration. The thousands of small

jets quickly coalesce into a coherent film which flows along the liner wall. As such, the cooling potential of effusion cooling is twofold:

1. Heat is removed from the liner via convection as the cool air flows through the small holes.
2. The film of cool air creates a protective barrier between the liner and the combusting gas.

To further improve the effectiveness of effusion cooling, the holes are typically drilled at a shallow angle, as shown in Figure 1.5b. This increases the internal surface area of the hole, thereby increasing heat extraction. Furthermore the jet penetration is reduced, minimising separation and promoting a strong, coherent film.

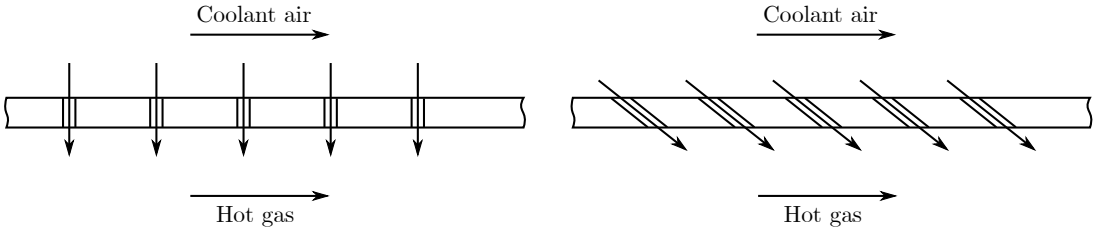

(a) Effusion cooling. **(b)** Angled effusion cooling.

Figure 1.5: Effusion cooling configurations.

Impingement/Effusion Cooling

Impingement/effusion cooling, as shown in Figure 1.6, is a hybrid liner cooling topology which requires a double-skin liner wall. The outer impingement wall is perforated with small holes which are drilled normal to the surface. These holes produce jets which impinge on the inner effusion wall, augmenting the convective cooling. The air is then passed through effusion holes in the inner wall, which is directly exposed to the combusting gas.

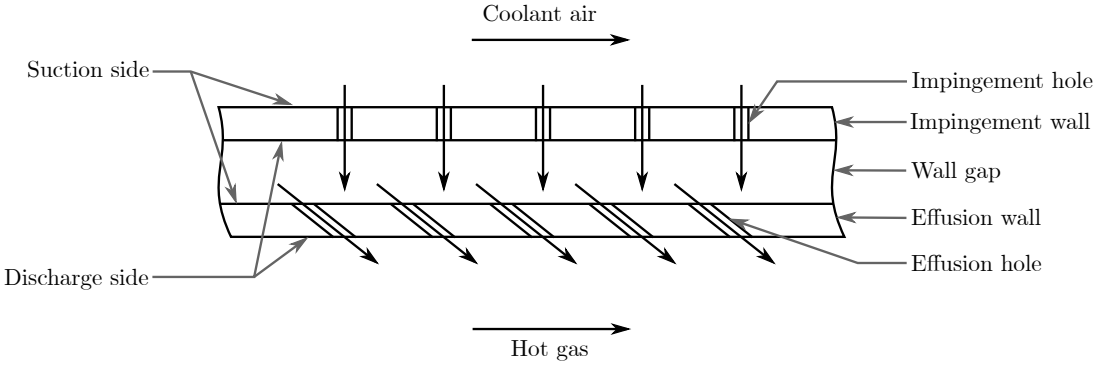

Figure 1.6: Impingement/effusion cooling.

Conjugate Heat Transfer

Conjugate heat transfer (CHT) is a general term for heat transfer between a fluid and a solid body, where the solid body conduction plays a significant role. These types of problems can be modelled in most computational fluid dynamics (CFD) packages. This typically requires the solid body to be included in the geometry and meshed, preferably with a conformal interface.

In CHT CFD simulations, the fluid transport equations are solved in the usual manner. These equations account for the fluid motion and heat transfer, both in the fluid domain and at the fluid-solid interface. In addition, the heat transfer by conduction in the solid domain is modelled using Fourier's law.

As will be shown in Section 2.2, three approaches have been taken to CHT CFD simulations involving advanced cooling methods:

- Explicit resolution of the cooling holes.
- Modelling the cooling heat and mass transfer using a combination of heat and mass sources and sinks. This will be referred to as the source-based approach.
- Decoupling the problem and solving the fluid domain in CFD and the solid domain in a finite element package.

The last approach is cumbersome and has demonstrated limited benefit. As such only the first two will be considered for this research.

1.2 Motivation

Gas turbine combustion is a complex problem which presents severe analysis challenges. Current combustor design tools are largely based on empirical correlations. The lack of reliable modelling techniques and demanding performance requirements have made combustor development an iterative and expensive process. In this process, the designer must negotiate a series of trade-offs between highly coupled conflicting parameters. For example, thorough mixing is desirable as it promotes rapid burning rates, ensuring high combustion efficiency and low pollutant formation. Unfortunately, mixing comes at the cost of pressure loss, and overall cycle efficiency demands that the hard-won compressor pressure rise be used sparingly. As such, the designer must tread a fine line of achieving sufficient mixing without compromising cycle efficiency. These design challenges have historically led to an evolutionary design approach. Proven designs are typically altered to meet new requirements, as revolutionary design is prohibitively expensive given the current design tools.

Poor modelling capability has additionally resulted in many problematic phenomena only being discovered after prototype testing. A prime example of this is thermo-acoustic instabilities, which are typically not captured by analysis. Such a discovery demands drastic design intervention at a mature stage of the

design cycle. The lack of predictive capability for these phenomena can have a significant impact on project cost and schedule.

Design difficulties are further compounded by increasingly stringent emissions targets, which cannot be achieved by current combustion topologies. As such, novel combustor designs are required in order to move forward. The current design process, however, does not cater for novel designs due to the reliance on empirical data from historic configurations. While the combustor designer could rely entirely on high fidelity simulation, this would be prohibitive from a time-line and cost perspective. The drive for novel, ultra-low emissions combustors dictates that the combustor development process must be revised.

Context

Cranfield University has proposed a multi-fidelity approach to combustor modelling. This process involves combining high and low order models to create a tool for rapid design space exploration. The high order model, typically CFD, has good predictive capability but is computationally expensive. The low order model, a 1D or 2D physics-based approximation, sacrifices accuracy for computational speed. In the multi-fidelity method, the high order model is to be used to inform and calibrate the low order model, which is then used for design optimisation. Such a tool will facilitate detailed multi-objective optimisation studies, allowing complex trade-offs to be analysed. These studies will be essential if the emissions targets are to be met.

Significant contributions to this design tool have been made in PhD studies by Liu (2018) and Sun (2018). Liu created a low order tool for novel combustor design. This tool was validated against a commercial combustor and then applied to the design of an LDI combustor for a high bypass ratio turbofan. Sun utilised high order modelling in the form of CFD simulations to perform parametric studies on the combustor generated by the low order tool.

One of the critical design activities identified was ensuring combustor durability. The extreme temperatures in the combustor require that the liner be cooled in order to achieve sufficient service life. The cooling scheme is required to maintain acceptable metal temperatures while preventing severe thermal gradients. The liner cooling design problem is subject to a number of unique challenges. A few of these are summarised below:

- The majority of air used for liner cooling will not partake in combustion. For this reason its use is largely wasteful and as such the minimum amount of air should be used.
- Poorly designed liner cooling can lead to an increase in intermediate species emissions, as poor mixing of the cool air leads to reaction quenching.
- The high airflow requirements of lean burn combustors leave very little air available for cooling. This calls for highly efficient cooling designs.

- The drive to increase cycle efficiency has led to the use of higher overall pressure ratios. As a consequence of this, compressor outlet temperatures (and thus coolant temperatures) have increased, leading to a reduction in cooling effectiveness.

In addition to these design challenges, the analysis of cooling designs is not trivial. Prediction of the heat loading on the combustor liner walls is dependent on detailed knowledge of the combusting flow field. The heat transfer to the liner will vary based on local near wall temperatures and velocities. In the swirling, turbulent, combusting flow, the near wall conditions vary dramatically over the liner surface. These 3D effects cannot be accounted for in a low order model, yet they will have an important impact on an optimisation study. This makes liner cooling a prime candidate for multi-fidelity modelling.

History

Gent (2018) assessed the suitability of CHT CFD simulations as a potential high fidelity model for liner cooling. Gent employed this technique to assess the liner cooling design generated by the low order model of Liu. The design employed angled effusion cooling on the inner liner wall and impingement/effusion cooling on the outer liner wall, as seen in Figure 1.7. Due to computational limitations, Gent only analysed the effusion cooled inner wall. In spite of this, it was shown that the cooling design generated by the low order model was ineffective when considering 3D effects. Gent's work demonstrated the importance of involving high order models in the liner cooling optimisation process.

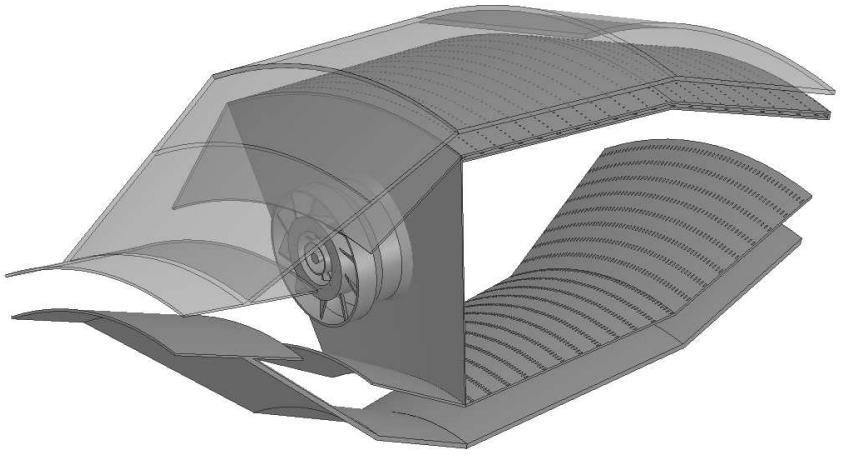

Figure 1.7: Segment of combustor studied by Gent (2018)

A number of gaps were identified in Gent's research, prompting further work. Primarily, as previously mentioned, the investigation was limited to the portion of the wall which employs angled effusion cooling. Further work was proposed to analyse the outer liner wall, which is cooled with impingement/effusion cooling.

In addition to this, the study was conducted with the assumption of negligible radiative heat flux. This warrants further study to quantify the impact of the inclusion of radiation modelling on liner wall temperature predictions. Furthermore, Gent's work relied on wall-functions for boundary layer modelling. Best practice dictates boundary layer resolution when studying heat transfer. The impact of this decision should be quantified.

1.3 Research Objectives

This study aims to develop a methodology for analysing double skin impingement/effusion cooled combustor liners in order to contribute to the Cranfield University multi-fidelity preliminary design tool. Additionally, the proposed work aims to address the following research gaps:

- To investigate the use of CHT CFD simulations as a tool for wall temperature predictions of an impingement/effusion cooled combustor liner.
- To assess the impact of boundary layer treatment on liner wall temperature predictions.
- To investigate the trade-off between mesh resolution and predictive capability in order to ease the computational expense.
- To assess the impact of radiation modelling on liner wall temperature predictions.

1.4 Summary

The design of gas turbine combustors is an iterative and expensive process, largely due to a lack of modelling tools. Cranfield University has proposed a multi-fidelity modelling approach to address this issue and improve the preliminary design process. The current work falls within this overarching effort.

Combustor durability has been identified as an area which could benefit from the multi-fidelity approach. It has been proposed that high fidelity CHT CFD simulations be used to study liner wall temperatures. The insights gained can then be used to calibrate low-order models and make more informed durability predictions.

The CHT CFD method has demonstrated value when applied to effusion cooled walls. The current study aims to extend this to impingement/effusion cooled walls. This must be achieved in a manner which is computationally feasible in the context of the preliminary design phase. In addition to this, the impact of radiation modelling is to be assessed.

Chapter 2

Literature Review

In this chapter, three key topics relating to the current research are introduced and recent research activities are reviewed. First, current studies on impingement/effusion cooling are presented and discussed. This is followed by a review of recent work on conjugative heat transfer simulation of combustors and impingement/effusion cooled walls. Finally, relevant literature on radiation modelling is discussed.

2.1 Impingement/Effusion Cooling

A number of impingement/effusion cooling design parameters have been experimentally investigated. These include geometric, flow and heat transfer parameters. Commonly studied geometric parameters are the hole spacing S, or pitch P (typically non-dimensionalised by hole diameter, S/d or P/d), the gap between the plates (typically z/d), hole length or plate thickness (typically t/d, H/d or L/d), and the angle of the effusion holes. The main flow parameter that has been studied is the blowing ratio, which is the mass flux ratio between coolant and mainstream flow. The final significant parameter is the Biot number, which is the ratio of convective to conductive heat transfer.

The most commonly used performance metric in these studies is cooling effectiveness, typically denoted as ϕ or η. This is defined as per Equation 2.1:

$$\phi = \frac{T_m - T_w}{T_m - T_c} \tag{2.1}$$

which is the ratio of differences between the mainstream and wall temperatures, and the mainstream and coolant temperatures.

The experimental investigation of impingement/effusion cooled combustor liners is still in its infancy. Current literature is limited to the testing of flat impingement/effusion cooled plates, typically in wind tunnels with heated main flow and a secondary supply for coolant air. Due to energy limitations, the differential temperature is typically limited to around 20 K.

An example of such a testing configuration is shown in Figure 2.1. This particular facility was used by Xiao-ming *et al.* (2015) to assess the adiabatic

and overall cooling effectiveness of impingement/effusion plates. Pure effusion cooling was also studied in order to assess the benefit of the impingement/effusion configuration. Additionally, the effects of using different blowing ratios and pitch to diameter ratios were assessed. Wall temperatures were measured using infrared thermography in order to assess cooling effectiveness.

Xiao-ming *et al.* showed that for large hole spacings, impingement/effusion cooling out-performed pure effusion cooling. This suggests that impingement/effusion cooling can provide superior cooling with reduced coolant mass flow rates.

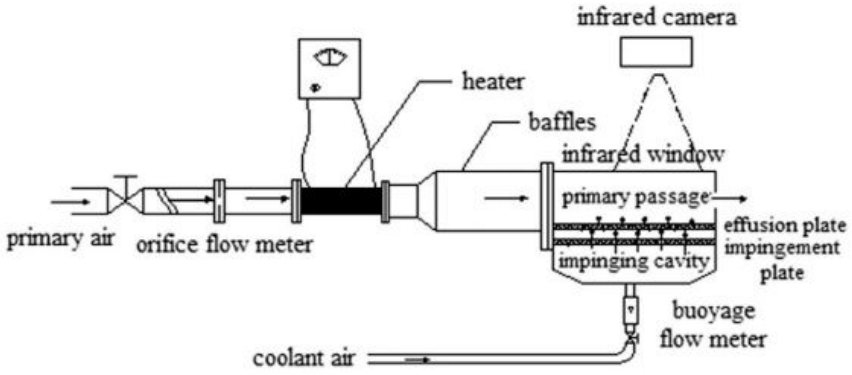

Figure 2.1: Schematic of typical wind tunnel configuration for testing of impingement/effusion cooled plates (Xiao-ming *et al.*, 2015).

Similar facilities have been used by Rogers *et al.* (2017), Ligrani *et al.* (2017) and Ligrani *et al.* (2018) to assess various cooling parameters. The facilities used in these experiments had a third air supply to provide cross flow in the gap between the plates and assess its impact.

Ligrani *et al.* (2017) collected experimental data for impingement/effusion cooled plates at various blowing ratios. It was found that cooling effectiveness increased with blowing ratio up to the point where the effusion jet momentum was sufficient to cause lift-off from the inner wall. At this point no further effectiveness was gained.

Rogers *et al.* (2017) extended this study by testing the plates under more realistic conditions. In particular, the effusion plate was fed with cross-flow rather than from a plenum as in previous work. Ligrani *et al.* (2018) furthered the tests of Rogers *et al.* (2017) by imposing a streamwise pressure gradient in the mainstream flow, as is typically encountered in a combustor.

Singh and Ekkad (2017) studied impingement/effusion cooling in flat plates with an emphasis on the effects of spent air removal from the gap between the plates. The wall temperature on the discharge side of the effusion plate was assessed using an optically clear wall backed with a thermochromic liquid crystal. In addition to heat transfer data, the pumping power was recorded for each flow condition. This showed that allowing for spent air removal via crossflow ducts reduced cooling performance, but simultaneously reduced pumping requirements. This would correspond to a lower pressure drop in a combustor. It was shown

that a small allowance for cross flow air removal is desireable for optimal cooling performance.

Jung *et al.* (2017) assessed the impact of thermal conductivity by using impingement/effusion cooled plates constructed from various materials. Pure effusion cooled plates were also studied for comparison. Jung *et al.* showed that the improved effectiveness offered by impingement/effusion cooling increased with decreasing Biot number (i.e. increasing plate conductivity). The averaged total cooling effectiveness was increased by over 8% in the lowest Biot number case, as shown in Figure 2.2.

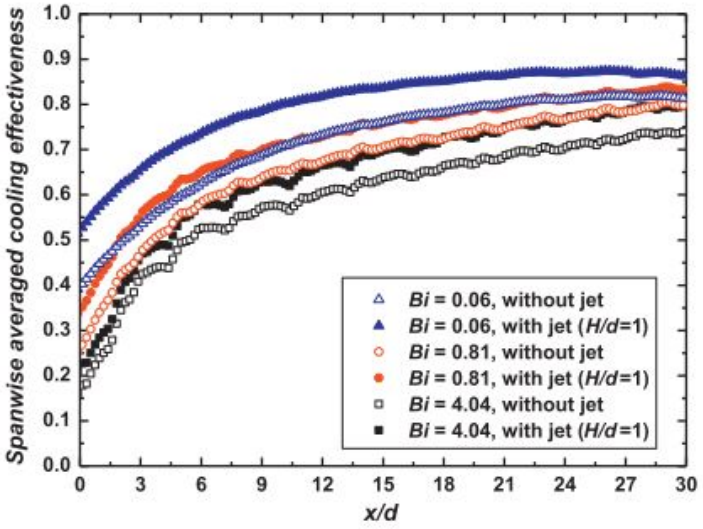

Figure 2.2: Transverse averages of cooling effectiveness at various Biot numbers, with and without impingement jets (Jung *et al.*, 2017).

As a step towards more representative impingement/effusion cooling studies, Shrager *et al.* (2018*a*) and Shrager *et al.* (2018*b*) studied the cooling effectiveness and flowfield characteristics of impingement/effusion cooled plates in the vicinity of dilution holes. Three hole layouts were assessed, with changes being made only to the effusion holes near the dilution hole. The layouts tested were: blocked effusion holes, holes pointing radially into the dilution jet and holes pointing radially away from the dilution jet. The study showed that the region around the dilution hole was best cooled with the addition of effusion holes. It was however found that the interaction between the dilution jet and the inward effusion holes compromised downstream cooling effectiveness.

These studies have highlighted valuable interactions between the various design parameters available for impingement/effusion cooling. Their value is, however, limited by the simplifications that have been made. The effect of curved combustor walls, reacting flow and a highly swirling mainstream are yet to be investigated.

By comparison, pure effusion cooling studies are relatively advanced. Andreini *et al.* (2015*a*), Andreini *et al.* (2017*a*) and Andreini *et al.* (2017*b*) have performed isothermal studies of representative LDI combustor segments. These

studies have shown a strong interaction between the cooling film and the swirling flow produced by the injector. More specifically, the swirling jet has a destructive effect on the cooling film and thereby reduces local cooling effectiveness. This is illustrated in Figure 2.3, in which the swirl impingement zone is evident as a region of low cooling effectiveness. It was further shown by Andreini *et al.* (2017*b*) that highly angled effusion cooling holes produce a strong, coherent film which is more resistant to the destructive effect of the swirling flow. These effects will have a similar, but yet unquantified effect on the impingement/effusion configuration.

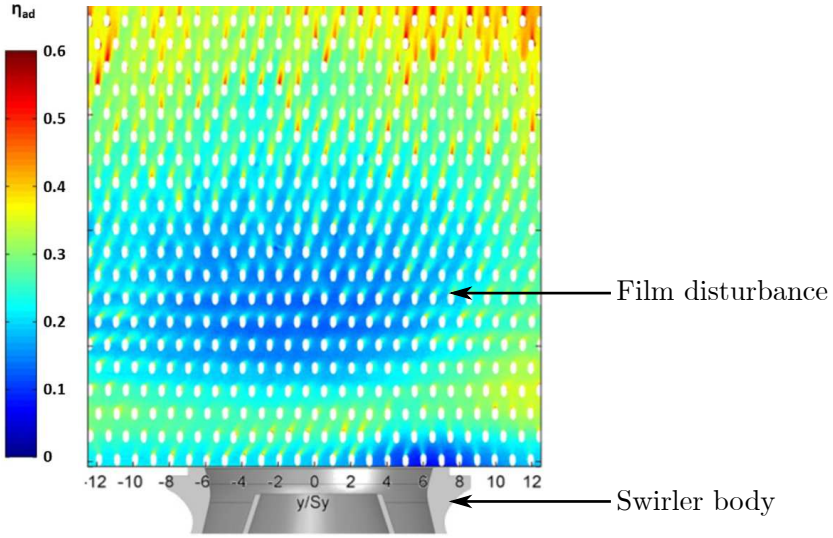

Figure 2.3: Contours of cooling effectiveness in a representative LDI combustor (Andreini *et al.*, 2015*a*).

Ge *et al.* (2017) and Ji *et al.* (2018) have studied the effectiveness of effusion cooling in a representative combustor under reacting flow conditions. In both cases a three-injector segment of a lean direct injection combustor was studied in a test rig with optical access facilitating infrared thermography of the liner walls. The methane-fueled combustor was run at various operating conditions, and different effusion cooling configurations were studied. Both Ge *et al.* and Ji *et al.* noted the impact of the swirling flow on cooling effectiveness in the reacting case, as Andreini *et al.* did in the isothermal case.

2.2 Conjugate Heat Transfer

The conjugate heat transfer method has been applied to combustor liners for many years. Early studies, such as Bailey *et al.* (2002) and Bahador and Sundén (2006), applied the method to industrial gas turbine combustors. Computational limitations dictated significant geometry simplification and no cooling details were studied.

Jeromin *et al.* (2008) performed CHT CFD simulations on an angled effusion cooled plate to assess the predictive capability for subsequent application to combustor liners. Jeromin *et al.* showed good predictive capability of the CHT method when applied to effusion cooled plates.

Still limited by computational resources, Andreini *et al.* (2013) developed a source-based approximation to effusion cooling and applied it to a CHT CFD simulation of a representative combustor. The method used a combination of mass sources and sinks to approximate the transfer of mass across the liner. Heat sinks in the solid domain were used to approximate the convective cooling in the effusion passage. This is shown schematically in Figure 2.4. Mazzei *et al.* (2017) used this method to replicate the experimental work by Andreini *et al.* (2015*a*), as discussed in Section 2.1, which revealed the interaction between the swirl and cooling film. Mazzei *et al.* showed that the source-based approach was able to capture the interaction between the swirling jet and cooling film, and predict the impact on cooling effectiveness.

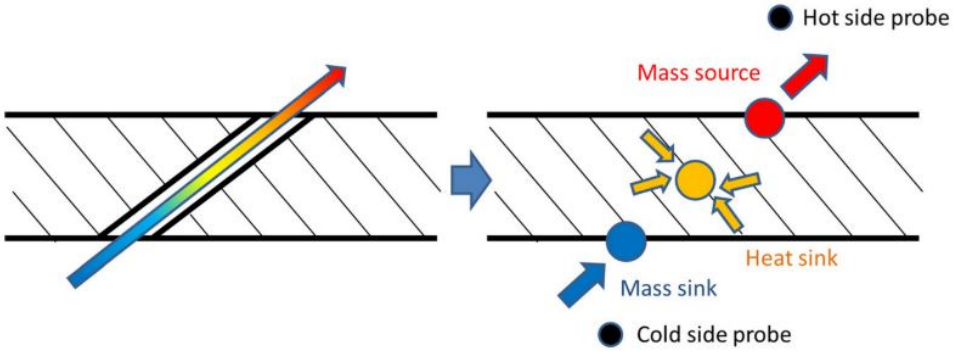

Figure 2.4: Source-based approximation to effusion cooling in a CHT CFD simulation (Andreini *et al.*, 2013).

Da Soghe *et al.* (2016) applied the CHT CFD method to a realistic combustor geometry. The analysis was performed at various operating conditions and the results were compared to experimental data. Da Soghe *et al.* was able to reproduce the trends from experimental data, as well as achieving quantitative accuracy within 7.5%. The geometry analysed by Da Soghe *et al.* did not, however, utilise any advanced cooling techniques. Similar results have been obtained by Jaure *et al.* (2013) and De Santis *et al.* (2016) on vastly different combustor geometries, neither of which employed advanced cooling.

A different approach was taken by Piskin and Topal (2016), who simulated the fluid domain in CFD and the solid domain using finite element analysis (FEA). Fluid temperatures and heat transfer data from the CFD model were used as boundary conditions in the FEA model. This, in turn, was used to predict solid body temperatures. The CFD model was then rerun with the new wall temperatures as boundary conditions. A number of these iterations were performed until wall temperatures converged to a stable solution. Experimental data were reasonably well reproduced with this method.

Dauptain and Duchaine (2017) performed a rigorous numerical study of an angled effusion cooled plate in which LES turbulence modelling was employed. Dauptain and Duchaine noted complex flow structures in the vicinity of the cooling holes which played an important role in plate temperature prediction. These structures were highly sensitive to changes in hole geometry. It was postulated that these details would not be captured by RANS turbulence modelling or the source-based approach and therefore more thorough verification of the use of these approaches was recommended.

Gent (2018) analysed an effusion cooled wall of a representative combustor under reacting flow conditions. The study utilised the CHT CFD methodology with RANS turbulence modelling. The angled effusion cooling holes were resolved rather than modelled with a source-based approach. Gent showed the ability of the CHT CFD method to predict detailed flow interactions.

As with experimental studies, the numerical investigations of impingement/effusion cooling are limited to studies of flat plates. The bulk of the available work has been performed by El-jummah *et al.*, who have numerically studied various impingement/effusion cooling parameters on flat plate geometries. El-jummah *et al.* (2013) applied the CHT CFD method to the analysis of impingement cooled flat plates with no effusion holes. El-Jummah *et al.* (2014) then expanded this study to assess the impact of impingement hole spacing. El-jummah *et al.* (2016) assessed impingement/effusion cooled plates with normal effusion holes.

Kim *et al.* (2014) used CHT CFD simulations to study a single impingement/effusion hole set. The goal of this study was to optimise the impingement jet for minimal thermal stress. Kim *et al.* showed that well positioned impingement cooling holes can result in a significant reduction in thermal stress.

Liu *et al.* (2018) performed a broad study of impingement/effusion cooled plates using CHT CFD simulations. Multiple plate configurations were studied under various operating conditions. A grid and turbulence model sensitivity study was also performed and the results were compared to experimental data. Liu *et al.* showed a strong sensitivity to the turbulence model used, as shown in Figure 2.5. It can be seen that only the k-ω based closure models produced results representative of the experimental data. This is expected given their well-documented advantages in the near-wall region.

The effect of turbulence modelling in impingement/effusion CHT CFD simulations was further studied by Andreini *et al.* (2018). This study assessed the predictive capability of RANS turbulence modelling against the scale adaptive simulation (SAS) method, which is a hybrid RANS-LES model. Andreini *et al.* showed that while RANS models could not capture the same level of detail as SAS, they were capable of predicting area averaged heat transfer values to within 10%.

In addition to turbulence modelling, the effect of various other simulation assumptions have been evaluated. Most notable for the current work are the studies of Mazzoni *et al.* (2015) and Hwang *et al.* (2016). Mazzoni *et al.* studied the feasibility of utilising thermal wall functions with the CHT CFD approach in order to avoid having to resolve the thermal boundary layer. The simulations which employed wall functions were shown to compare well with experimental

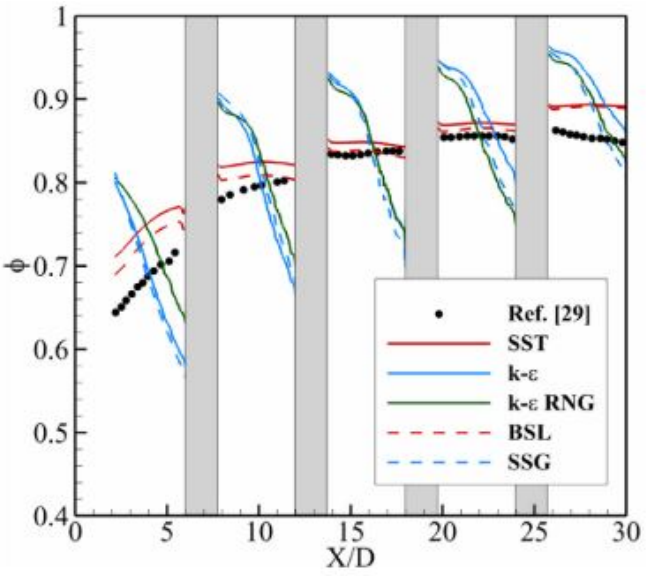

Figure 2.5: Local overall cooling effectiveness at y/d=1.5 using various turbulence models (Liu *et al.*, 2018).

data. While this work is not directly relevant as it was carried out on turbine blades and used a non-commercial code, it prompts further investigation. Hwang *et al.* studied the impact of using steady state simulations to predict cooling performance on turbine blades. This study showed that the unsteady effects had a notable impact on the overall cooling performance.

2.3 Radiation

Radiative heat transfer in gas turbine combustors falls into two categories: non-luminous and luminous. Non-luminous radiation is primarily emitted by CO_2 and H_2O, and occurs entirely in the infra-red spectrum, hence the name non-luminous. Luminous radiation is emitted by particulate matter in the flame. The hot particles emit radiation in the visible spectrum as well as infra-red. Luminous radiation is typically the dominant heat transfer mechanism in combustors with a fuel-rich primary zone, particularly at high pressure ratios (Lefebvre and Ballal, 2010).

Two main problems arise with the analytical modelling of radiative heat transfer. The first is the estimation of the radiative properties of the participating medium. The second is determining the radiation intensity. Radiation modelling is a broad field, and many solutions to both problems exist. These solutions make varying degrees of simplifying assumptions, focusing their application on specific problems. Only the approaches most applicable to combustion problems are discussed here.

Many gasses and gas mixtures, such as oxygen and nitrogen at room temperature, will not participate in radiative heat transfer. However certain species, including combustion products like CO_2, H_2O and soot, do participate. These

species will emit, absorb and scatter radiation as it passes through the medium. The fraction of radiative intensity which is emitted, absorbed or scattered, as well as the wavelength in which the participation takes place, depends on temperature and species concentration. In order to estimate radiative properties of a gas mixture in a computationally feasible manner, a number of assumptions must be made.

In combustion, the most common approach is the weighted-sum-of-grey-gasses (WSGG), which assumes an absorbing and emitting medium surrounded by black walls. This is often the case in combustors where walls are blackened by soot, but may not be accurate in modern lean burning combustors. The WSGG model approximates the emissivity and absorptivity of the combustion gasses as the weighted sum of the properties of constituent species, as shown in Equation 2.2. While this model accounts for different absorption and emission coefficients for each of the species, it assumes that each of the species radiates as a grey gas. This means that absorption and emission occurs uniformly across the radiation spectrum. This assumption severely limits the applicability of the WSGG model, but makes the computational requirements feasible for industrial application. The WSGG model has been shown to work well in combustion cases, provided the relative concentrations of CO_2 and H_2O remain within the limits of ideal combustion (Modest, 2013).

$$\varepsilon(T,s) = \alpha(T,s) \approx \sum_{k=0}^{K} a_k(T)(1 - e^{-\kappa_k s}) \tag{2.2}$$

In the above equation, the emissivity ε (and equally absorptivity α) of the fluid mixture is modelled as a weighted sum of the grey gas absorption coefficients for each of the species, κ_k. The weighting coefficient a is temperature and species dependent, which is necessary in combustion modelling where wide spacial variations in the temperature and species fields are expected.

Analytical modelling of radiative heat transfer intensity requires the solution of an integro-differential equation known as the radiative transfer equation (RTE), shown in Equation 2.3 (Modest, 2013). This equation essentially models how radiation emitted in each direction is attenuated by absorption, augmented by emission and diverted by scattering. The RTE models both scattering out of the direction of concern (out-scattering), as well as scattering from all other directions into the direction of concern (in-scattering).

$$\frac{dI}{ds} = \kappa(\vec{r})I_b(\vec{r}) - \beta(\vec{r})I(\vec{r},\hat{s}) + \frac{\sigma_s(\vec{r})}{4\pi}\int_{4\pi} I(\vec{r},\hat{s}')\Phi(\vec{r},\hat{s}',\hat{s})d\Omega' \tag{2.3}$$

The above equation models the change in radiative intensity in a particular direction $\hat{s}$. Augmentation by emission at point $\vec{r}$ is accounted for in the first term on the right of Equation 2.3. The second term on the right accounts for attenuation by absorption, as well as out-scattering at point $\vec{r}$ and in direction $\hat{s}$. The final term on the right considers augmentation by in-scattering from all

other directions into the direction $\hat{s}$. This requires integration over a unit sphere in order to account for every possible direction $\hat{s}'$.

For most problems the analytical solution of the radiative transfer equation is not possible and simplified models are required. The most commonly applied model in combustion cases is the discrete ordinates (DO) model. This model discretises continuous space into a finite set of solid angles along which the RTE is solved. Under this assumption, Equation 2.3 simplifies to the set of coupled differential equations shown in Equation 2.4 (Modest, 2013). This essentially reduces the RTE into a radiative intensity transport equation which can readily be implemented in a finite volume solver.

$$\frac{dI}{ds_i} = \kappa(\vec{r})I_b(\vec{r}) - \beta(\vec{r})I(\vec{r},\hat{s}_i) + \frac{\sigma_s(\vec{r})}{4\pi}\sum_{j=1}^{n} w_j I(\vec{r},\hat{s}_j)\Phi(\vec{r},\hat{s}_j,\hat{s}_i) \tag{2.4}$$

In the above equation, the subscript i refers to the direction under consideration and the subscript j can refer to any of the other discrete directions from which radiation has been scattered. The weighting factor w_j acts to ensure that the full 4π steradians of the unit sphere are accounted for in the numerical quadrature.

Studies of radiative heat transfer in combustors are incredibly rare. There are, however, a few studies which have made exceptional contributions to the field.

Jones and Paul (2005) performed a numerical study on the radiative heat transfer in a representative combustor. This study began with the validation of the DO model. An ideal furnace was modelled with the DO model and the results were compared to available data. The DO model was shown to be capable of predicting both gas temperatures and wall fluxes with fair accuracy. Following validation, the model was applied to an LES simulation of a representative gas turbine combustor. This analysis, reported in Jones and Paul (2005) and Paul and Jones (2006), considered only non-luminous radiation, as soot formation was not modelled.

Porter *et al.* (2010) studied radiative heat transfer from oxy-fuel combustion. The study included an assessment of different radiation models as well as radiative property models. It was shown that the DO model is most applicable for combustion problems. Porter *et al.* showed considerable error (up to 50%) when using the WSGG method when compared to a benchmark model. It was, however, noted that this was likely due to the significantly higher concentrations of CO_2 in the oxy-fuel combustion system which rendered the WSGG model invalid.

The WSGG model was further studied by Wang *et al.* (2014) with CO_2 concentrations more representative of those in gas turbine combustors. A maximum error of 23% was noted when compared to results generated with a benchmark model. Similar error levels were noted by Johansson *et al.* (2011).

Saygin *et al.* (2016) investigated the effects of radiation modelling on liner temperatures predicted by CHT CFD simulations of a combustor. The inclusion

of radiation modelling significantly reduced predicted liner temperatures, and brought them more in line with experimental data as shown in Figure 2.6.

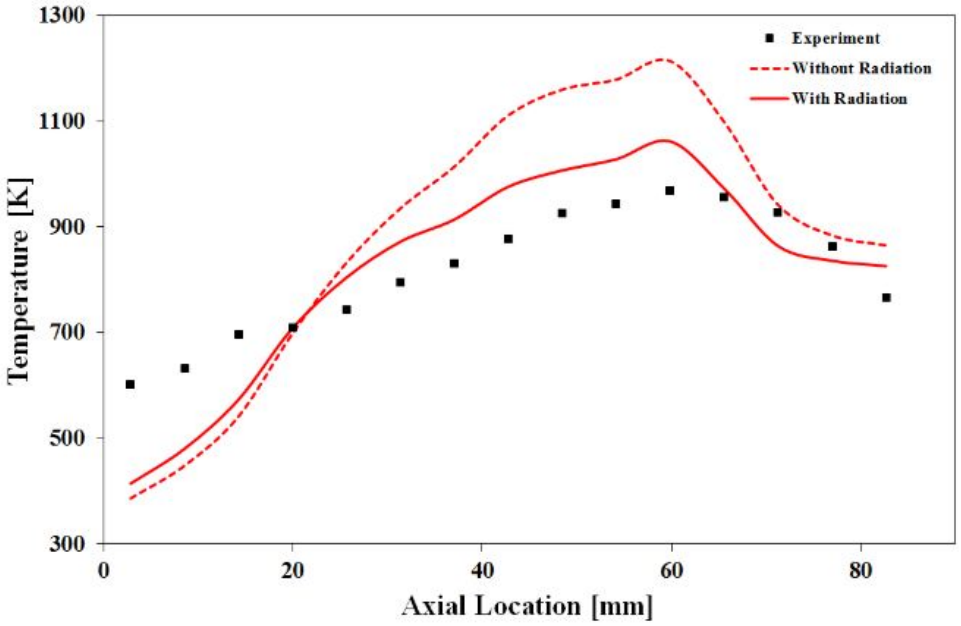

Figure 2.6: Circumferentially averaged temperature distribution with and without radiation modelling (Saygin *et al.*, 2016).

2.4 Summary

The literature review has highlighted the state of the art in three key fields relevant to the current work. It was shown that experimental investigation of impingement/effusion cooling has not progressed as far as other cooling schemes. Experimentation has been limited to flat plates in wind tunnels with moderate temperature differentials. This will be a limitation in the current work, as experimental data is required for model validation. High order effects such as complex fluid interactions and reacting main flow have not yet been studied. These will be revealed through the current work. The experimental work has, however, identified key physical phenomena which must be captured by the numerical model. This informed the simulation approach in the sections to follow.

Conjugate heat transfer simulations have been successfully applied to combustor liners and impingement/effusion cooled plates. In both cases, reasonable predictive capability was shown, with results often within 10% of experimental or reference data. The configuration of an impingement/effusion cooled combustor liner, as is proposed for the current research, has not yet been studied. Three main methods have been used for conjugate heat transfer analysis. The first method, in which the cooling holes are geometrically resolved, simulates in detail the flow through the cooling holes. As such the heat and mass transfer

is explicitly resolved to within the accuracy limits of the CFD code. In the second method, the cooling holes are modelled using a combination of heat and mass sources and sinks. This methodology has the potential to reduce computational expense, but introduces the uncertainty of additional abstraction. The final method decouples the problem and solves the fluid domain using CFD and the solid domain using FEA. This approach is cumbersome and offers limited benefit. It will therefore not be considered in the present research.

Limited research has been published on radiation modelling in combustors, but a few highly relevant papers were found. These papers identified the best modelling approach for combustion problems. Further to this, model validity has been demonstrated and accuracy limitations have been identified. The available research neglected luminous radiation due to a lack of reliable soot modelling techniques. This is not a limitation for the current research, as the LDI combustor to be assessed will produce very little soot at design point, and therefore negligible luminous radiation. Finally, the benefit of radiation modelling when predicting liner temperatures has been demonstrated for a conventional combustor with no wall cooling. The case of an LDI combustor with advanced wall cooling has not yet been studied.

Chapter 3

Validation and Mesh Study

This chapter covers the details of the validation study, in which an experimental case was reproduced using CHT CFD simulations. Due to the complexity and cost of combustor rig testing, very little test data is available in the public domain. For this reason, a generic experimental study of an impingement/effusion cooled plate had to be used for validation. The validation study included an investigation of uncertain boundary conditions, the impact of assuming periodic symmetry, as well as a study of the sensitivity to turbulence model selection.

Once the method was shown to be valid, a parametric mesh sensitivity study was performed. In this study, a number of critical meshing parameters were varied to assess the impact on predictive capability. This included the necessity of boundary layer resolution, the sensitivity to resolution in both the cooling holes and the plate gap, and the sensitivity to mesh topology. These studies allowed for the trade-off between accuracy and computational cost to be assessed in a systematic manner. This was necessary as the computational cost of applying this method to a representative combustor was expected to be extremely high. The result of this study was a set of meshing parameters which could be applied to a similar cooling configuration, regardless of the specific geometry.

3.1 Experimental Case Study

Following a review of current literature, the work of Jung *et al.* (2017) was identified as a suitable experimental case on which validation studies could be performed. The experimental work assessed the impact of conductive heat transfer on the cooling effectiveness of impingement/effusion cooled plates. As such, the data will prove useful in validating and assessing mesh sensitivity of the CHT CFD analysis of such cooling configurations.

The study was briefly described in Chapter 2. The relevant details required for replicating the experiment in CFD are provided below.

3.1.1 Geometry

The experimental setup used by Jung *et al.* is shown in Figure 3.1. Detail of the plate cross section is shown in the inset. Jung *et al.* further state that the holes were staggered in the transverse direction. Additional geometric parameters are summarised in Table 3.1.

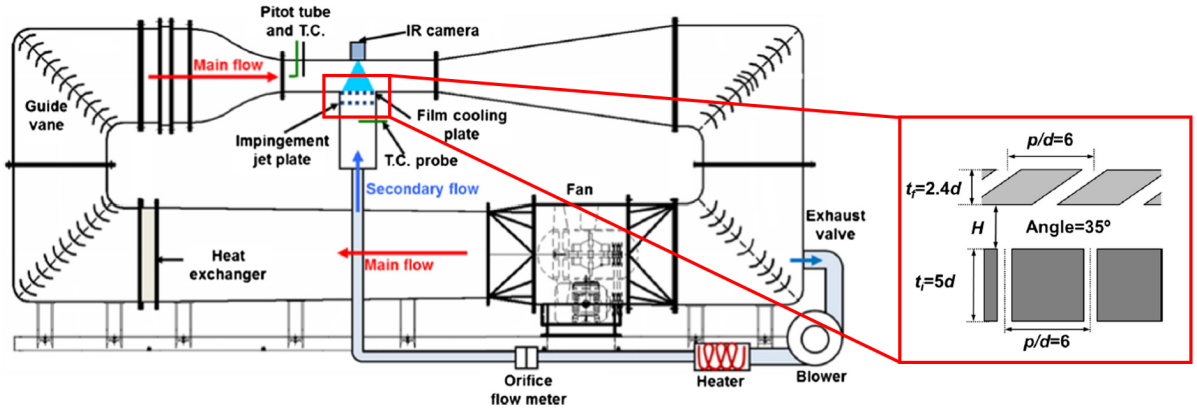

Figure 3.1: Schematic of setup used by (Jung *et al.*, 2017).

Table 3.1: Geometric parameters of experimental case

Parameter	Value
Test section dimensions	240 mm x 300 mm x 200 mm (l x w x h)
Plate dimensions	240 mm x 240 mm (l x w)
Number of holes	13 rows of 12 or 13 holes (stagger dependent)
Hole diameter (d)	5 mm
Plate spacing (H)	5 mm

3.1.2 Test Conditions

The momentum and thermal conditions provided by Jung *et al.* (2017) are summarised in Table 3.2. Additionally, the following non-typical conditions should be noted. The first is that the secondary flow was fed perpendicular to the impingement plate. This is not the case in a gas turbine combustor, where the annulus flow is parallel to the impingement plate. The second is that the secondary flow was heated, while the main flow was cooled. Again, this is opposite to the combustor.

No detail is provided in Jung *et al.* (2017) regarding the edge conditions of the plates. As such, a further initial study was required in order to determine the thermal boundary condition at the plate edges.

Table 3.2: Test conditions of experimental case (Jung *et al.*, 2017)

Parameter	Unit	Value
Main flow:		
Temperature	K	300
Velocity	$\mathrm{m\,s^{-1}}$	34
Reynolds number[1]		10 000
Turbulence intensity	%	1.5
Secondary flow:		
Temperature	K	323
Jet velocity	$\mathrm{m\,s^{-1}}$	11
Jet Reynolds number[1]		3 000

[1] Based on hole diameter.

3.1.3 Material Properties

Plates manufactured from stainless steel AISI 304, Corian and polycarbonate were studied by Jung *et al.* The stainless steel case was selected for the validation study, as it is most representative of a combustor liner. The material properties of the plates were published by Jung *et al.* as per Table A.1 in Appendix A. It should be noted that these values differ from those published in most materials databases. In spite of this, the values reported by Jung *et al.* were used.

3.1.4 Results

For the purpose of evaluating the predictive capability of the CFD simulations, an evaluation metric and set of experimental results were required. For this study, a convenient metric was the cooling effectiveness, as defined in Section 2.1 and repeated in Equation 3.1 for convenience.

$$\phi = \frac{T_m - T_w}{T_m - T_c} \tag{3.1}$$

Jung *et al.* plotted transverse averages of cooling effectiveness against axial position, as is shown in Figure 3.2. This served as a convenient quantitative comparison between CFD and experimental data. In addition to this, Jung *et al.* captured contours of cooling effectiveness using infra-red thermography. These contours, shown in Figure 3.3, served for qualitative comparisons.

It should be noted that the results reported by Jung *et al.* were collected from the discharge side of the effusion plate. Further to this, it should be noted that only a portion of the plate was surveyed. The data collection region covered only the first eight rows of the central three columns of the plate. This was mimicked in the numerical study described below.

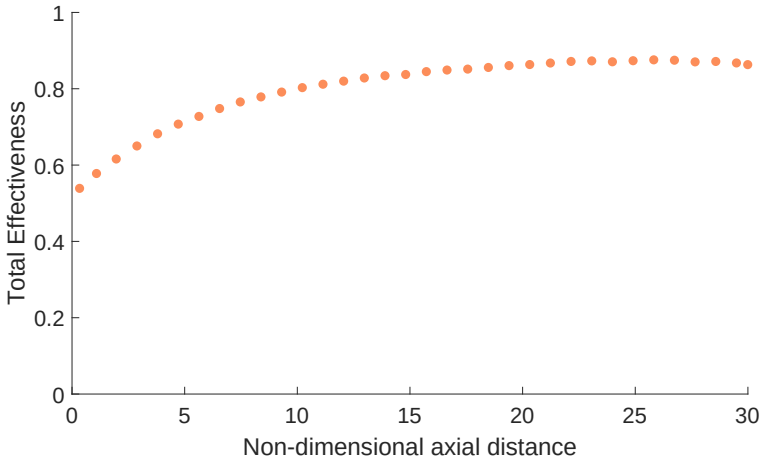

Figure 3.2: Transverse averages of cooling effectiveness vs non-dimensional axial distance.

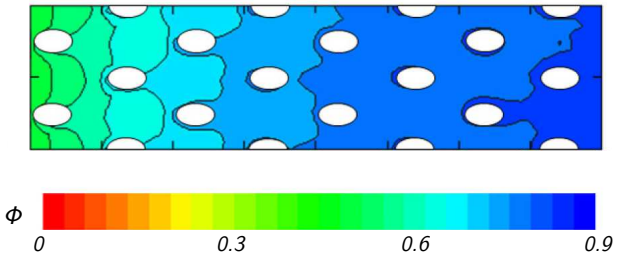

Figure 3.3: Contours of cooling effectiveness on a portion of the effusion plate (Jung *et al.*, 2017).

3.2 Benchmark Simulation

As a point of departure, a benchmark simulation was performed. In this simulation, best practice (as advised in ANSYS (2019*a*)) was applied as far as possible in order to obtain a reference result. This provided additional data which was not reported by Jung *et al.*, but could be used to assess how predictive capability was affected by various meshing parameters.

3.2.1 Geometry

The geometry described in Section 3.1.1 was reproduced, taking advantage of the translational periodic symmetry. Best practice dictates that three periodic sectors be resolved, with data being collected from only the central section. This reduces the impact of the assumption of periodic flow. Considering the number of simulations to be performed, the necessity of this was investigated, as it would triple the size of each mesh. The results of this investigation, presented in Section 3.2.4, showed that a single sector was satisfactory for this case. The geometry for a single periodic sector is shown in Figure 3.4.

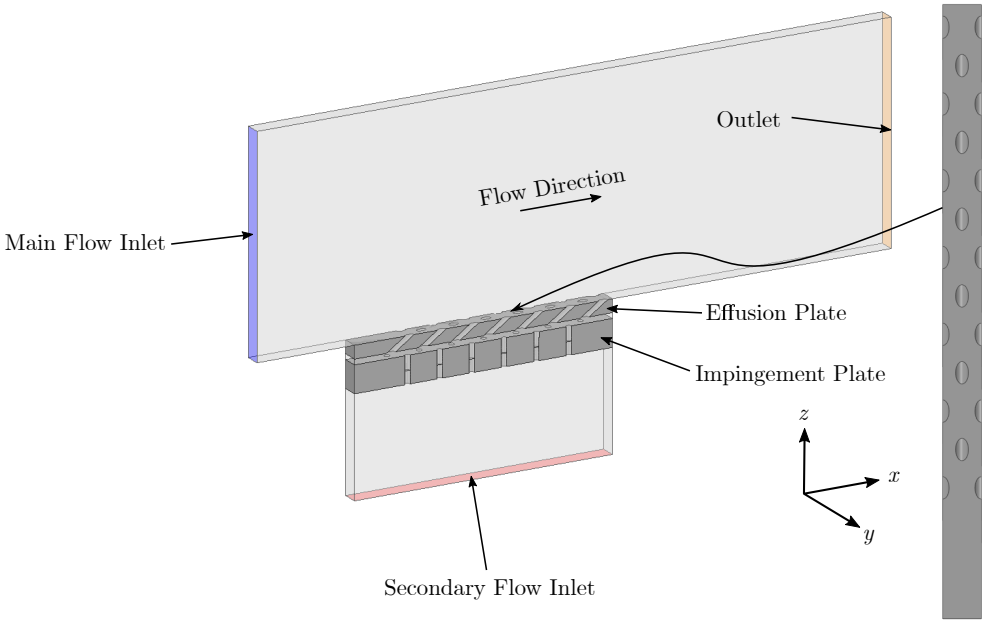

Figure 3.4: Single periodic repeat of CFD geometry.

3.2.2 Mesh

The benchmark mesh was a tetrahedral mesh with an inflation layer. The inflation layer parameters were iteratively determined to achieve acceptable boundary layer resolution. The first cell height was iteratively reduced until $y^+ < 1$ was achieved throughout the domain. The number of cells in the inflation layer was iteratively increased until free-stream velocity was attained within the inflation layer. This was achieved with 12 cells starting from a first cell height of 6×10^{-6} m and at a growth rate of 1.2.

Each hole was discretised with 25 cells defining the perimeter. This ensured that at least 12 cells were placed across the diameter of the hole (not including inflation layer cells). The mesh in the gap between the plates was refined to ensure that a minimum of 10 cells spanned the gap.

The benchmark mesh consisted of 5.5 million cells. Images of critical portions of the benchmark mesh are presented throughout the remainder of this chapter and will not be shown here.

3.2.3 Solution & Convergence

The viscous Navier-Stokes equations were solved using a pressure-based solver. The k-ω SST RANS turbulence closure was used to model the Reynolds stresses. This was selected due to its broad applicability and its good performance in both near-wall and free shear regions. Further to this, Liu *et al.* (2018) showed that only k-ω closures performed well in similar studies.

A coupled, pressure-based solver was used and all equations were solved with second order spacial discretisation. Minimal under-relaxation was applied to the solution so as to avoid false indications of convergence.

Given that the purpose of this investigation was to trade off solution quality for a reduction in computational effort, it was expected that residuals would not be a useful convergence criterion. This is due to the fact that problem conditioning typically deteriorates with a reduction in resolution. As such, the following convergence criteria were set:

- Mass flux imbalance, averaged over the previous 10 iterations, to drop below 1% of the mass flux through the secondary inlet.
- Heat flux imbalance, averaged over the previous 10 iterations, to drop below 1% of the heat flux through the discharge side of the effusion plate.
- Area average of cooling effectiveness on the discharge side of the effusion plate to have a standard deviation below 1×10^{-3} over a period of 10 iterations.
- Maximum of cooling effectiveness on the discharge side of the effusion plate to have a standard deviation below 1×10^{-3} over a period of 10 iterations.
- Minimum of cooling effectiveness on the discharge side of the effusion plate to have a standard deviation below 1×10^{-3} over a period of 10 iterations.

The solution was deemed converged once all of these conditions were met. These criteria allowed for consistent judgement of convergence, even on poor meshes where residual error remained relatively large. This facilitated the recording of time to convergence, a convenient metric for computational cost.

3.2.4 Results

Effect of Edge Condition

In order to address the uncertainty regarding the thermal boundary conditions at the plate edges, two extreme cases were studied. The first was adiabatic edges, representing perfectly insulated plate edges. The second was isothermal edges, where the leading and trailing edge temperatures were set to that of the main and secondary flow respectively. The results for these two cases are compared with experimental data in Figure 3.5.

It is clear from Figure 3.5 that the adiabatic case is not representative and should not be pursued further. The isothermal case, however, shows excellent agreement with experimental results.

The experimental data shows a slight reduction in cooling effectiveness towards the plate trailing edge. This is likely due to heat flux from the plate to the cooler wind tunnel structure (recall that the secondary stream is heated, so this would result in cooling effectiveness reduction). The trailing edge temperature imposed in the CFD did not account for this, leading to a loss of accuracy at a non-dimensional axial position of about 27. The model could be tuned by adjusting the trailing edge temperature until ideal correlation is obtained. It was however decided that sensible boundary conditions had been applied and the correlation was sufficient for the purpose of a mesh sensitivity study.

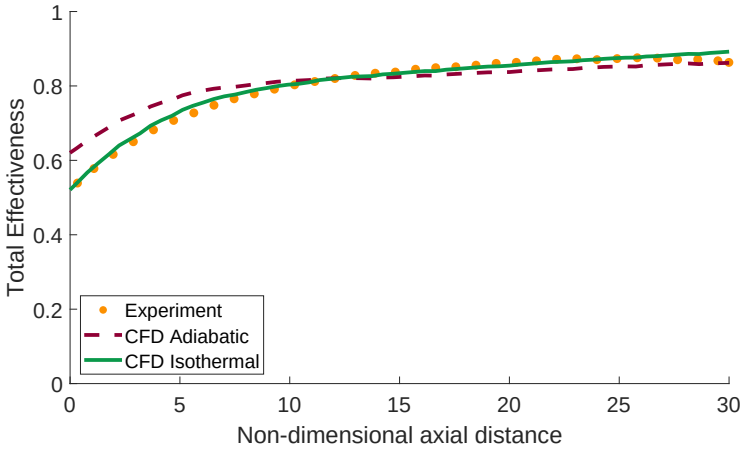

Figure 3.5: Comparison of transverse averaged cooling effectiveness for different plate edge boundary conditions.

Effect of Periodicity

In order to investigate the necessity of resolving three periodic sectors, two cases were simulated. The first resolved three sectors, and the second resolved only one. The results of the two cases are compared with experimental data in Figure 3.6. It can be seen that the results from the two meshes are practically identical. The similarity is further evident in the contours of cooling effectiveness shown in Figure 3.7.

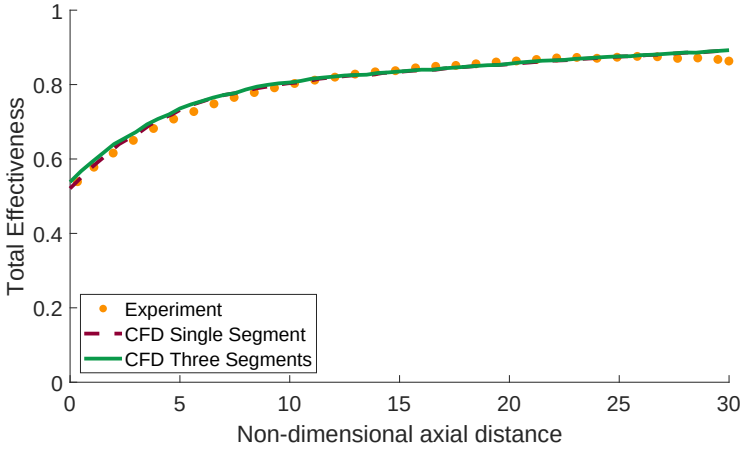

Figure 3.6: Comparison of transverse averaged cooling effectiveness from single sector and three sector meshes.

The close similarity is largely due to the absence of gradients in the transverse direction. The flow is axially-dominant, and fluxes across the periodic boundary are negligible. As a result, the periodic boundary had no significant effect on the flow field in this case.

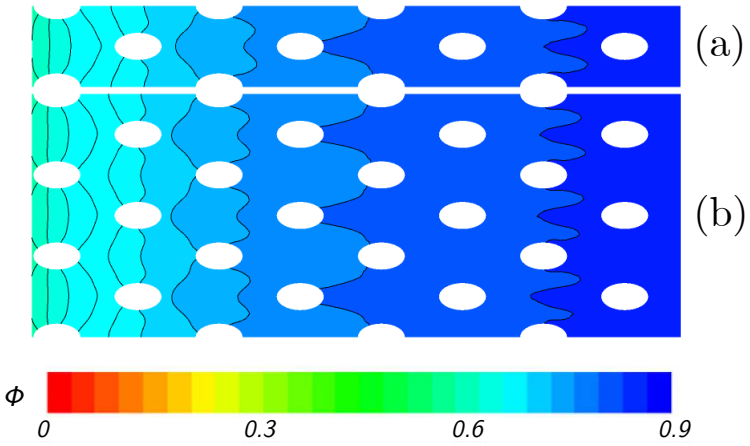

Figure 3.7: Contours of cooling effectiveness from single sector (a) and three sector (b) meshes.

Benchmark Results

Following these preliminary investigations, the benchmark simulation was defined as a single periodic section with isothermal edge conditions. The transverse averaged cooling effectiveness of this simulation had a mean squared error (MSE) of 0.562% compared to experimental data. This exceptional agreement shows that, provided good practice is applied, the CHT method can accurately predict the performance of impingement/effusion cooled walls.

The contours of cooling effectiveness from experiment and the benchmark simulation are compared in Figure 3.8. As with the transverse averaged data, the contours from experiment and simulation compare well.

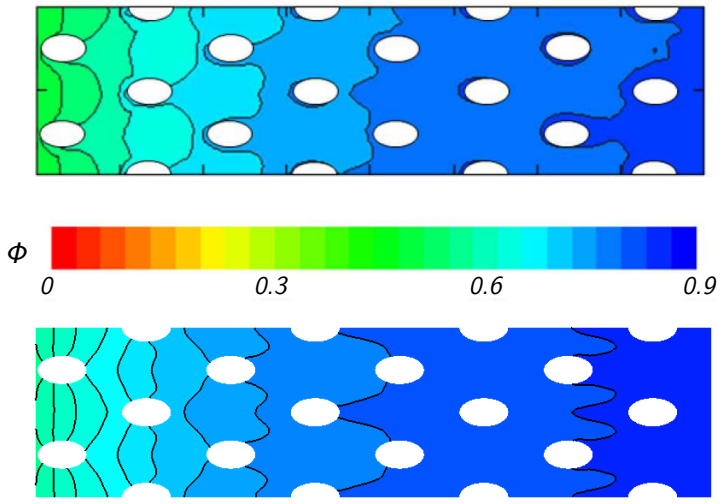

Figure 3.8: Contours of cooling effectiveness from experimental study (above colour scale)(Jung *et al.*, 2017) and benchmark CFD (below colour scale).

The total pressure drop across the plate was also monitored, as it is an important metric for any cooling system. This provided an additional metric to assess how predictive capability was affected by various meshing approaches. The total pressure drop predicted in the benchmark simulation was 0.206% of the secondary inlet total pressure. This data was not presented by Jung *et al.*, so this served as the reference value against which further simulations were compared.

Effect of Turbulence Model

With the benchmark performance defined, the sensitivity to turbulence modelling was assessed. This was necessary as many combustion models perform poorly with the k-ω SST closure model. The Realizable k-ε model is typically recommended for combustion modelling, but the k-ε family of models are known to have poor predictive capability in the near-wall region. As such, there is a disconnect in turbulence modelling requirements in the pursuit of performing CHT simulations with reacting flow.

Like any turbulence model, the k-ε equations require special treatment in the near-wall region. If the first grid node is sufficiently far from the wall, a wall function can be used to determine the turbulence parameters at the first node. These semi-empirical models also attempt to estimate the interaction at the wall, including quantifying the heat transfer. This however requires that the first node be placed in the fully turbulent region ($y^+ \geq 30$). This approach is referred to as the high-Reynolds solution.

For a fine mesh resolution ($y^+ \leq 1$), the k-ε equations must account for the viscosity-affected zone close to the wall. This is typically achieved through the use of a near-wall model, or a damping function which accounts for the viscous effects. This approach is referred to as the low-Reynolds solution, as the first node is placed in the laminar viscous sublayer.

Neither of these two approaches are robust when applied to meshes with incorrect near-wall resolution. This is problematic, as it is sometimes difficult or undesirable to maintain $y^+ \leq 1$ or $y^+ \geq 30$ throughout the domain. As such, a y^+ insensitive approach, called Enhanced Wall Treatment (EWT), was developed by ANSYS®. The EWT approach calculates both the high and low-Reynolds solutions throughout the domain. The two solutions are then combined by passing them through a blending function which weights each solution based on the local y^+ value. This blending process is shown in Equation 3.2 for a generic quantity ψ (ANSYS, 2019*b*).

$$\psi_{EWT} = \lambda\psi_{HR} + (1 - \lambda)\psi_{LR} \tag{3.2}$$

The blending function λ is typically a shifted inverse hyperbolic tangent function, such as the one shown in Figure 3.9. It is structured such that the low-Reynolds solution dominates at low y^+ values, with the high-Reynolds solution becoming increasingly dominant as the y^+ of the first node increases.

The benchmark case was repeated with the Realizable k-ε closure model to assess the impact on predictive capability. Enhanced Wall Treatment was used in these simulations to improve near-wall treatment. The results from the two

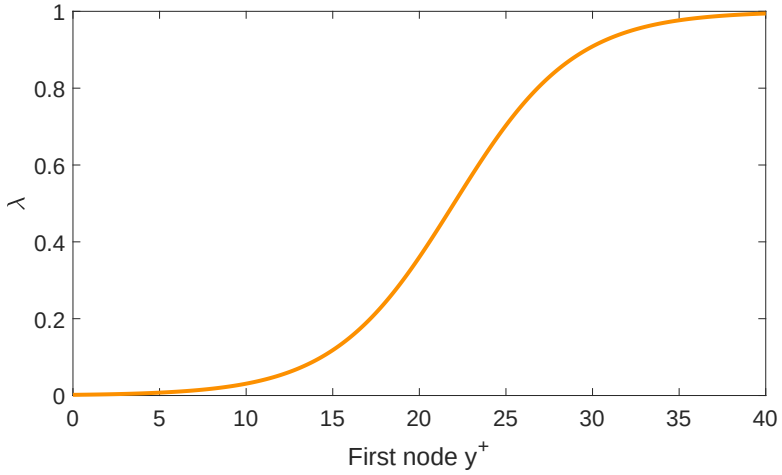

Figure 3.9: Typical blending function employed in the EWT approach.

turbulence models are shown in Figure 3.10. It is clear that there is a significant reduction in predictive capability when switching to k-ε. The k-ε closure produced a MSE of 1.62% compared with 0.562% for k-ω. This difference is significant, and limits the accuracy of this analysis method when applied to a reacting flow.

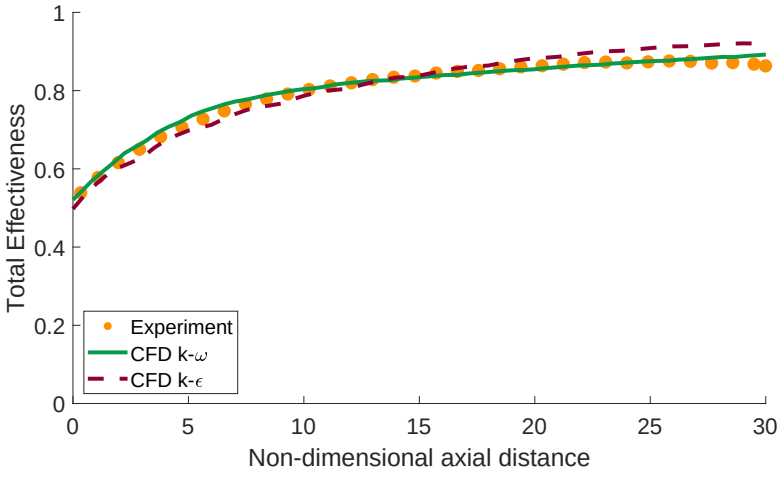

Figure 3.10: Comparison of transverse averaged cooling effectiveness for turbulence closures.

The difference in pressure drop prediction was less pronounced. The k-ε closure predicted 0.198% pressure drop compared to 0.206% predicted by k-ω.

The qualitative effect of changing the turbulence model is illustrated in Figure 3.11. As expected, the location of each iso-contour differs from that of the experiment. In spite of this, it can be seen that the general behaviour is captured. As such, the k-ε closure remains a valid choice for turbulence model, albeit less accurate.

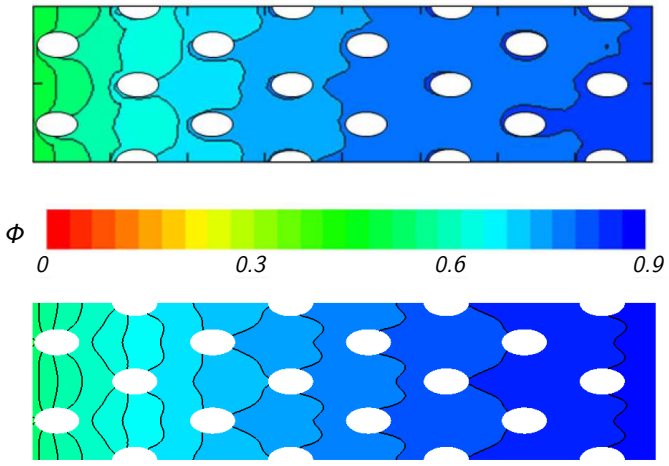

Figure 3.11: Contours of cooling effectiveness from experimental study (above colour scale)(Jung *et al.*, 2017) and CFD using Realizable k-ε (below colour scale).

Considering the objective of applying this method to a representative combustor, the remaining work was undertaken using the k-ε closure. While this has been shown to be inferior in predicting cooling performance, it was necessitated by convergence difficulties encountered when using the k-ω model in conjunction with combustion modelling.

3.3 Mesh Sensitivity Study

The performance of an impingement/effusion cooling system is driven by three key processes: augmented convection due to impingement jets, convection within the cooling channels and convection due to the film. In order to adequately capture these phenomena, it was proposed that good resolution would be required in the near wall region, the cooling channels and the gap between the walls. As such, the mesh resolution was systematically altered in these regions to quantify the individual sensitivities.

3.3.1 Effect of Inflation Layer

In order to assess the necessity of an inflation layer, the benchmark mesh was reproduced without one. This reduced the total cell count by more than 50%. Detail images of the benchmark mesh and mesh without inflation layer are presented in Figure 3.12. These show details of the mesh through the cooling channels, captured on the periodic boundary.

The transverse averaged cooling effectiveness is plotted in Figure 3.13 with the experimental data overlaid. CFD results obtained using the k-ε closure with the benchmark mesh have also been included for comparison. It can be seen that removing the inflation layer has negligible impact on the simulation results. The mean square error between experiment and CFD was 1.89% without an inflation layer. This is a marginal degradation from 1.62% with an inflation layer.

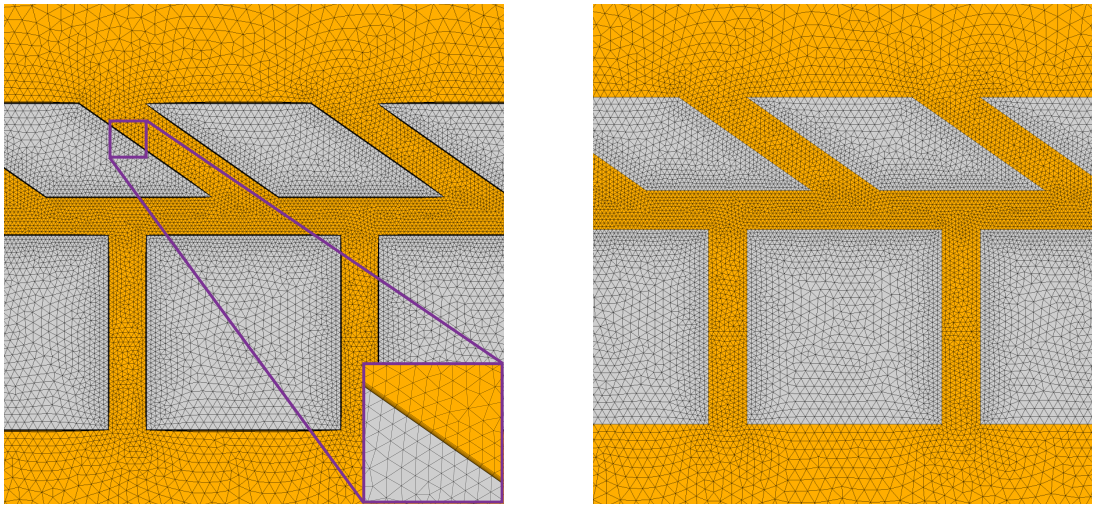

(a) Benchmark mesh with inflation layer, inflation layer detail inset.

(b) Mesh without inflation layer.

Figure 3.12: Comparison of meshes with and without inflation layers.

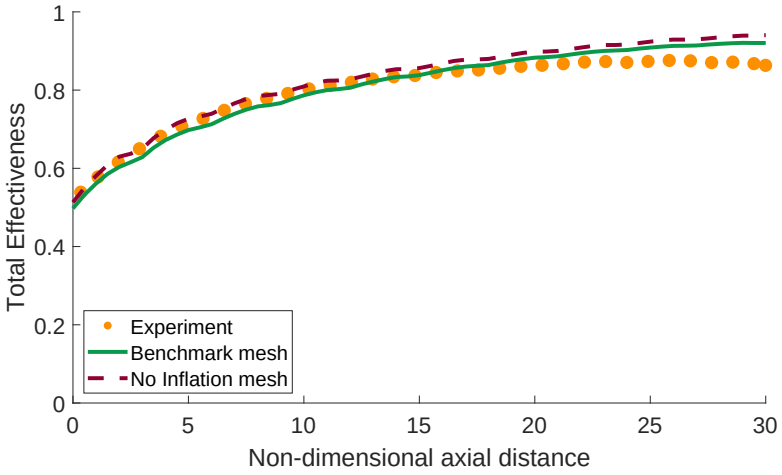

Figure 3.13: Comparison of transverse averaged cooling effectiveness with and without an inflation layer.

The total pressure drop predicted without an inflation layer was 0.176% of the secondary inlet total pressure. This is somewhat lower than the benchmark value of 0.206%, perhaps due to an under-prediction of viscous losses in the boundary layer.

It should be noted that removal of the inflation layer did not result in a drastic increase in y^+. In this case the requirement for good hole resolution, coupled with slow mesh growth, lead to an average y^+ of around 9. In this region the enhanced wall treatment still favours the low-Reynolds solution. As such, the turbulence model was attempting to resolve the boundary layer, in spite of a lack of grid resolution in the viscous sub-layer. While this is poor practice in general, it has yielded acceptable results in this case.

3.3.2 Effect of Hole Resolution

In order to assess the sensitivity to hole resolution, three additional meshes were created. In addition to the benchmark case where holes were discretised by 25 cells, cases with holes discretised by 18, 12 and 9 cells were run.

Hole resolution has three major impacts on the mesh. Firstly, it determines the geometric resolution of the holes. The circumference of each discretised hole is described by an inscribed polygon, the order of which is defined by the hole resolution. A poorly defined hole will not only lose geometric detail, but also incur an error in cross sectional area. Secondly, the hole resolution defines the number of cells spanning the diameter of the hole. It is vital that there are sufficient cells across the diameter to accurately describe the velocity profile in the channel. Finally, in the absence of an inflation layer, the hole resolution directly affects the y^+ value in the cooling channel, as well as the surrounding surfaces. All of these effects can be seen in the detailed images of the meshes, shown in Figure 3.14. These show the mesh in a cross section through the fluid domain of a single impingement hole.

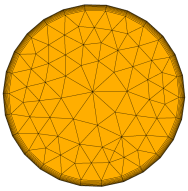

(a) Benchmark mesh.

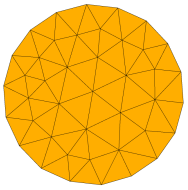

(b) 18 cells per hole.

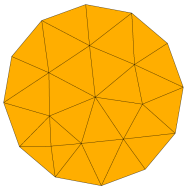

(c) 12 cells per hole

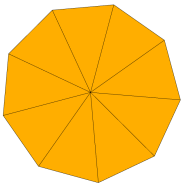

(d) 9 cells per hole

Figure 3.14: Comparison of meshes used in hole resolution sensitivity study.

The transverse averaged cooling effectiveness for these cases are plotted in Figure 3.15. This shows a clear trend of degradation of accuracy with reduction in hole resolution, worsening with axial position. The trend continues until complete failure to capture the cooling effectiveness in the coarsest mesh.

Loss of accuracy with increasing axial position suggests a failure in prediction of the film cooling mechanism, as the impingement mechanism is expected to be constant with axial position. This is supported by the near-wall velocity profiles in Figure 3.16, which show a reduced ability to describe the film behaviour as hole resolution is reduced. This can likely be attributed to two main shortcomings. The first is poor modelling of the jets exiting the hole due to insufficient detail being captured in the channel. The second is poor resolution in the region occupied by the film, due to an overall reduction in near-wall resolution. In the

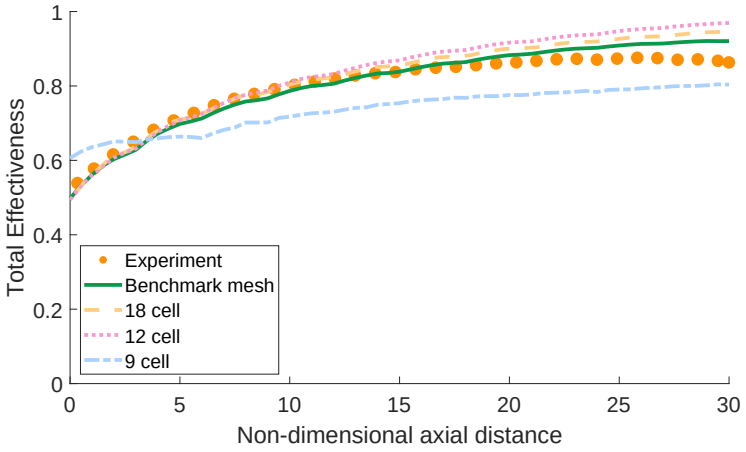

Figure 3.15: Comparison of transverse averaged cooling effectiveness for various hole resolutions

case of the coarsest mesh, the former was likely the main cause of the severely diminished predictive capability. As seen in Figure 3.14d, this mesh contained no cells in the core of the channel which would have resulted in nonsensical velocity profiles.

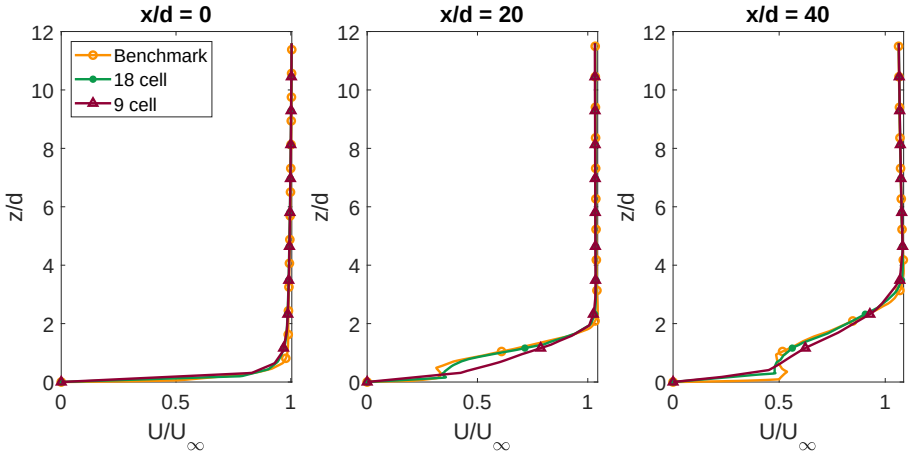

Figure 3.16: Near-wall velocity profiles for three meshes, at three non-dimensional axial positions on the discharge side of the effusion plate.

Quantitative performance data for this sensitivity study are presented in Table 3.3. The mean square error results reaffirm the degradation of predictive capability with decreasing hole resolution. The pressure drop results show interesting behaviour of under-prediction, transitioning to over-prediction as hole resolution is decreased. This is likely due to two competing factors, both of which change with hole resolution. One factor may be errors in the prediction of viscous losses due to incorrect near-wall velocity gradients. This would act to decrease pressure drop as hole resolution is decreased (Figure 3.16 above is an example of how reduced near-wall resolution can result in an under-prediction

of near-wall velocity gradient). A second factor may be the under-prediction of hole cross-sectional area with decreasing hole resolution, as is seen in Figure 3.14 above. This would act to increase pressure drop as hole resolution is decreased.

The increasing values of y^+ seen in Table 3.3 result in increasing dominance of the high-Reynolds wall treatment. This is not ideal for detailed assessment of heat transfer. Furthermore, the first node was placed deeper into the buffer layer as hole resolution was decreased. This would further contribute to a degradation of predictive capability.

Table 3.3: Summary of results from hole resolution sensitivity study

Mesh	Mesh Size	Average y^+	MSE	ΔP
Benchmark	1	0.441	1.62%	0.206%
18 cells per hole	0.251	14.6	1.95%	0.196%
12 cells per hole	0.154	22.0	2.76%	0.228%
9 cells per hole	0.119	28.3	4.33%	0.270%

3.3.3 Effect of Plate Gap Resolution

The sensitivity to the number of cells spanning the plate gap was explored. It was found that both the mesh count and the solution stability were highly sensitive to gap resolution.

Reducing the gap resolution below 10 cells resulted in an oscillating solution which never met the convergence criteria. It is proposed that this sensitivity is due to the complex vortex generation and interaction resulting from the array of staggered impinging jets. Each impinging jet forms a toroidal vortex, half of which is disturbed by the downstream effusion hole. This is illustrated in the plot of normalised vorticity in Figure 3.17.

The vortices from each hole interact, forming secondary and tertiary structures, as seen in the isosurface of Q-criterion in the upper half of Figure 3.18. These structures influence the heat transfer on the suction side of the effusion plate, as is shown in the contours of normalised Nusselt number in the lower half of Figure 3.18. The contours of Nusselt number reveal a honeycomb-like patternation imparted by the vortex structures. This characteristic of impingement/effusion cooling was also pointed out by El-jummah *et al.* (2016), Andreini *et al.* (2018) and others.

From this it was concluded that little compromise could be attained with gap resolution. As such, no fewer than 10 cells were used to span the plate gap in further studies.

3.3.4 Effect of Mesh Topology

The studies in Sections 3.3.1 and 3.3.2 were repeated with polyhedral meshes. In certain cases, polyhedral meshes can deliver high quality results at lower cell

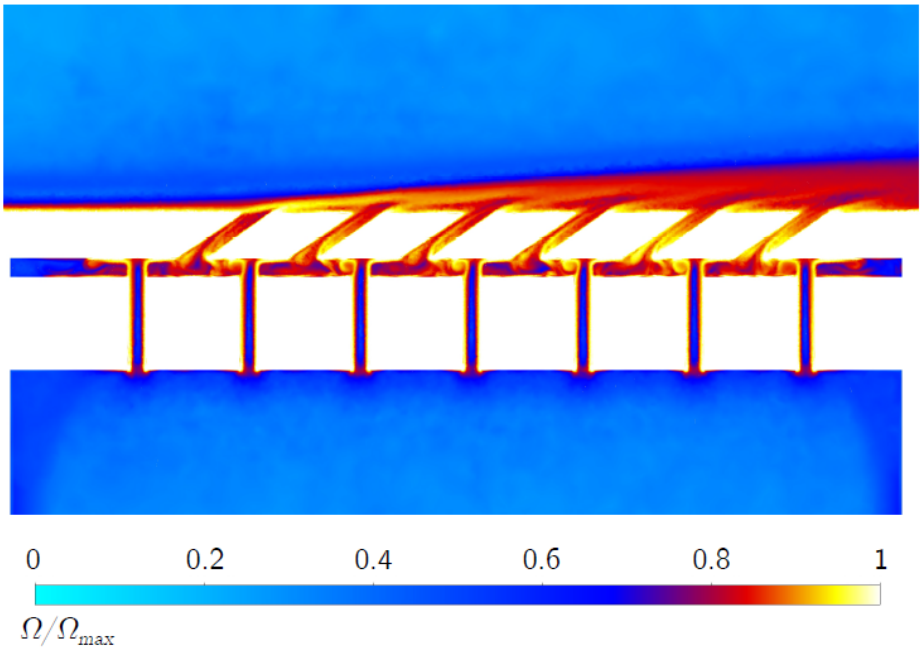

Figure 3.17: Contours of normalised vorticity through the mid-plane.

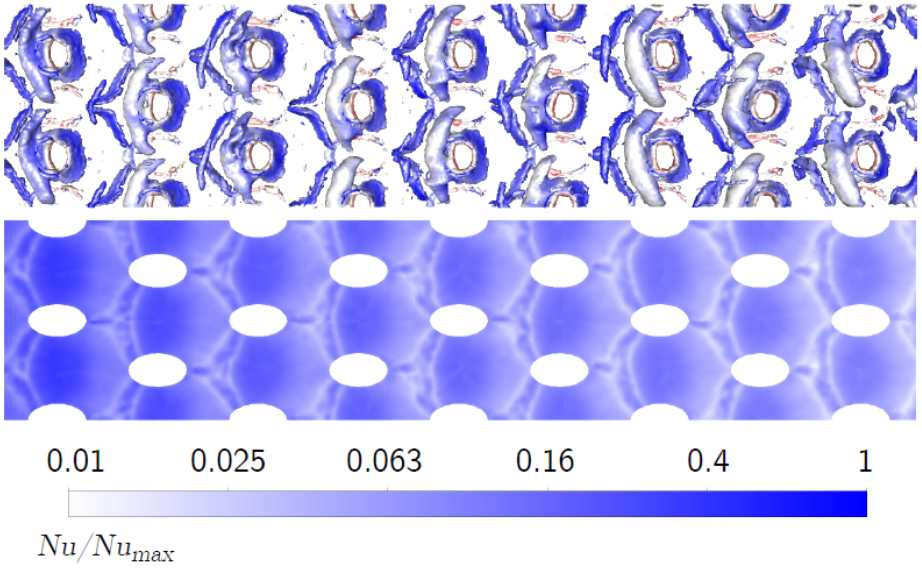

Figure 3.18: Isosurface of Q-criterion, arbitrary colouring for clarity (top). Contours of normalised Nusselt number on suction side of effusion plate (bottom).

counts than tetrahedral meshes. As such, the applicability of this topology to the impingement/effusion cooling configuration was assessed.

Polyhedral meshes were created using the native polyhedral meshing feature of Fluent Meshing®. The meshes were created from the same surface meshes as each of the cases described previously, including the benchmark case. The benchmark polyhedral mesh with and without an inflation layer are compared in Figure 3.19. The hole sensitivity meshes are compared in Figure 3.20.

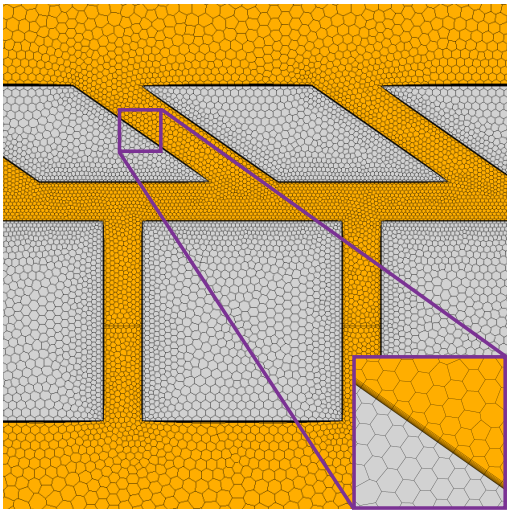

(a) Benchmark mesh with inflation layer, inflation layer detail inset.

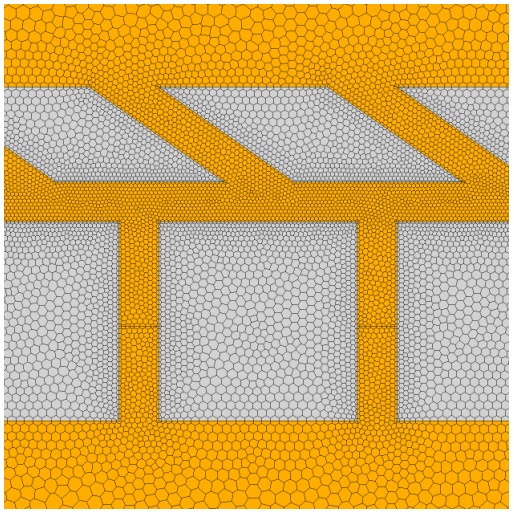

(b) Mesh without inflation layer.

Figure 3.19: Comparison of polyhedral meshes with and without inflation layers.

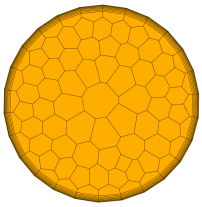

(a) Benchmark mesh.

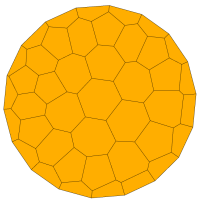

(b) 18 cells per hole.

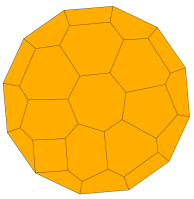

(c) 12 cells per hole

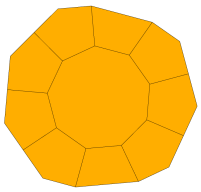

(d) 9 cells per hole

Figure 3.20: Comparison of polyhedral meshes used in hole resolution sensitivity study.

Figure 3.21 shows transverse averaged cooling effectiveness for the benchmark polyhedral mesh, and mesh without inflation. The benchmark polyhedral mesh shows similar characteristics to a poorly resolved tetrahedral mesh. This is expected, as larger polyhedra will provide less resolution than tetrahedra when seeded from the same surface mesh. Removing the inflation layer on the polyhedral mesh results in a significant reduction in predictive capability. The mean square error increases from 1.89% with the inflation layer to 3.50% without. This significant increase is due to the fact that the large polyhedral cells rely on the inflation layer to provide near-wall resolution.

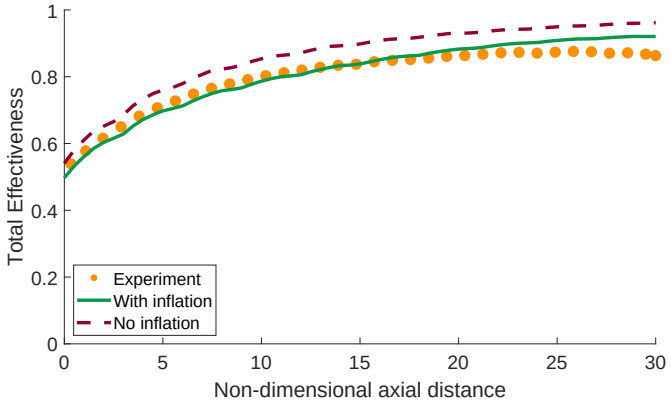

Figure 3.21: Comparison of transverse averaged cooling effectiveness for polyhedral mesh with and without inflation layer.

The effect of decreasing hole resolution is shown in the plots of transverse averaged cooling effectiveness in Figure 3.22. Unlike the tetrahedral mesh, limited reduction in predictive capability is seen with decreasing hole resolution. This is shown quantitatively in Table 3.4. A likely reason for this can be found in the near-wall velocity contours, shown in Figure 3.23. Unlike the tetrahedral meshes, the polyhedral meshes failed to capture the film behaviour with even 18 cells per hole. Further reduction of hole resolution from 18 cells to 9 cells did not significantly change the near-wall flow field, resulting in similar predictions for cooling effectiveness.

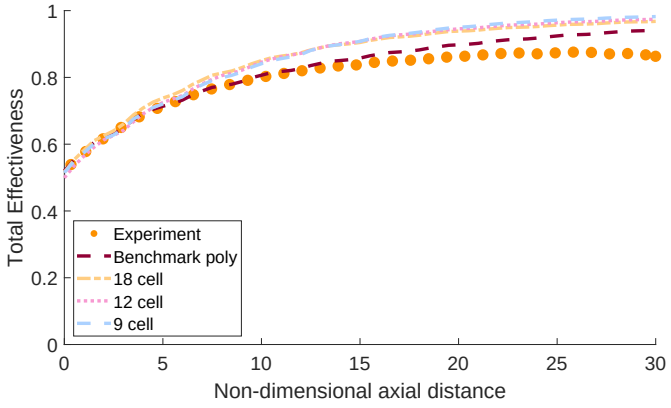

Figure 3.22: Comparison of transverse averaged cooling effectiveness for polyhedral meshes with various hole resolutions.

The reliance of polyhedral meshes on an inflation layer for near-wall resolution is evident from the y^+ values in Table 3.4. This shows a dramatic increase in y^+ once the inflation layer is removed. Furthermore, the y^+ is significantly higher for each polyhedral mesh than for the corresponding tetrahedral mesh. This further explains the poor performance of the polyhedral mesh without an inflation layer.

Table 3.4: Summary of results from polyhedral hole resolution sensitivity study

Mesh	Mesh Size	Average y^+	MSE	ΔP
Benchmark	0.305	0.405	1.89%	0.209%
18 cells per hole	0.0509	21.4	3.61%	0.190%
12 cells per hole	0.0398	26.0	3.79%	0.227%
9 cells per hole	0.0273	34.8	3.97%	0.235%

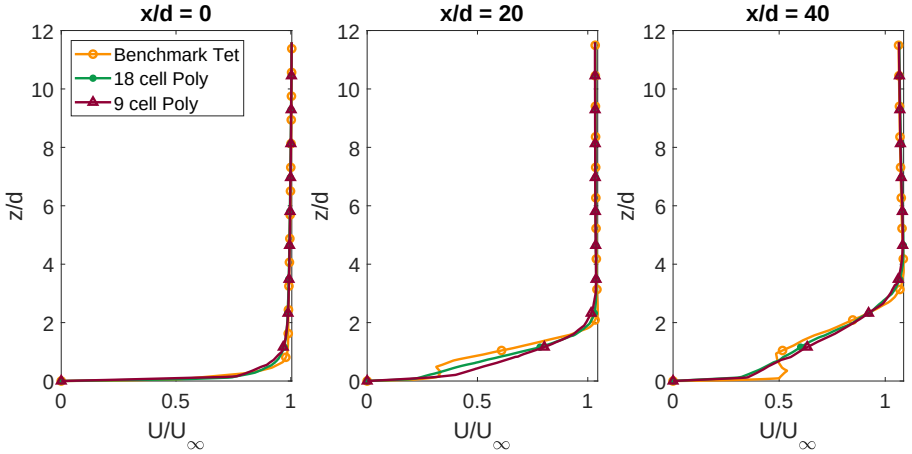

Figure 3.23: Near-wall velocity profiles for three meshes, at three non-dimensional axial positions on the discharge side of the effusion plate.

Table 3.4 also reveals that the polyhedral meshes behave similarly to the tetrahedral meshes in terms of pressure drop prediction. Decreasing hole resolution initially results in under-prediction of pressure drop, but this transitions to over-prediction with further reduction in resolution.

3.3.5 Source/Sink Approach

The approach of Andreini *et al.* (2013), introduced in Section 2.2, was applied to the impingement/effusion plates to assess its applicability to this case. From the literature review it appears that this approach has not yet been applied to the cooling configuration under consideration.

Ansys Fluent® does not have native support for the inclusion of point sources, as required for this method. While Ansys CFX® does support point sources, it lacks the radiation and combustion models required for the remainder of this study. As such, a user defined function (UDF) was written to incorporate point sources in Fluent®. The UDF was written to accept a set of coordinates corresponding to the centres of each cooling hole inlet and outlet. The cell closest to each point was then identified, and a set of source terms were applied to each of these cells. In this preliminary study, it was assumed that the cooling flow was split equally amongst the channels. In addition to this, the heat flux in the cooling channels was ignored. In spite of this, the source/sink model produced promising results, as illustrated by the contour comparison in Figure 3.24.

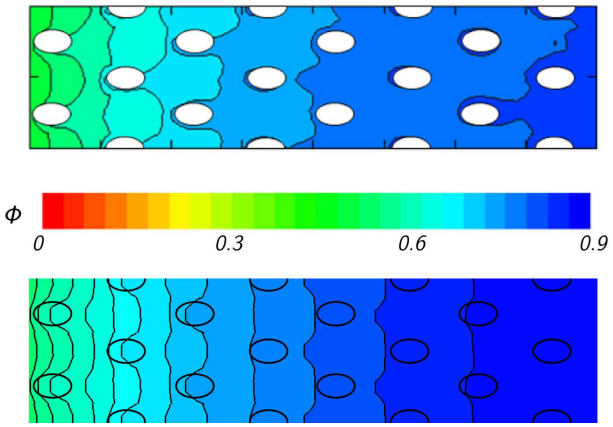

Figure 3.24: Contours of cooling effectiveness from experimental study (above colour scale)(Jung *et al.*, 2017) and CFD with source/sink approach (below colour scale).

While this method showed promise in the validation case, Gauthier (2019) revealed that this would be incompatible with the combustion model to be used in the remainder of this study. According to Gauthier, previous attempts had been made to reconcile point sources and the flamelet generated manifold (FGM) combustion model. After significant effort it was concluded that this was not feasible, and Gauthier advised that the process not be continued in this study.

3.4 Meshing Trade-off

The goal of this study was to identify the most efficient means of meshing an impingement/effusion cooled wall. The ideal meshing parameters would result in the optimal trade-off between computation time and mean square error in cooling effectiveness prediction. In order to assess this trade-off, relative time to convergence was plotted against mean square error for each of the simulations discussed above. This is shown in Figure 3.25.

In Figure 3.25, the optimal meshing parameters would yield a result closest to the origin - simultaneously minimising computation time and error. The case which achieves this is the tetrahedral mesh with 18 cells per hole and no inflation layer, solved with k-ω SST. Interestingly, the same mesh solved with Realizable k-ε is the nearest competitor. The Euclidian norms for the two cases are 1.89 and 1.94 respectively. While the k-ε closure yields less accurate results, it was consistently quicker to converge than the k-ω closure.

With the key objective of this study being wall temperature prediction, the above method was deemed the best means of determining ideal meshing parameters. It should be noted, however, that the optimal mesh identified above displayed notable under-prediction of pressure drop. Though it is not the primary focus of the study, this is a very important performance metric of liner cooling. As such, this shortcoming should be kept in mind when interpreting the results obtained from the combustion simulations.

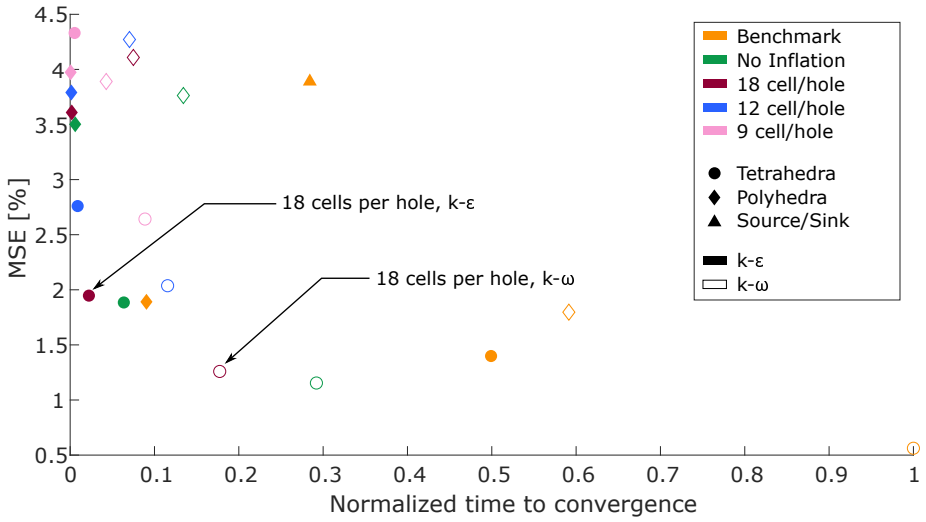

Figure 3.25: Relative time to convergence vs temperature prediction error for various meshes.

It is further clear from Figure 3.25 that polyhedra are unsuitable for this case, unless an inflation layer is used. While they are computationally effective, the predictive capability is too greatly hampered by their poor resolution in the near-wall region.

Finally, it should be noted that the source/sink method is not without promise for this cooling configuration, but its development was abandoned before many assumptions had been removed. It is felt that this method will scale very well and yield computational cost savings when applied to larger problems.

Chapter 4

Representative Combustor Analysis

With the CHT method verified and meshing sensitivities understood, it could be applied to a representative gas turbine combustor. This chapter presents an initial study in which a representative combustor was analysed in the absence of radiation modelling. This is in line with previous work performed in the overarching project. The combustor studied was identical to that studied by Gent (2018), however the current work focused on the impingement/effusion cooled outer liner wall.

This chapter begins with a detailed presentation on the geometry, mesh and simulation parameters. Key assumptions are stated and shortcomings are disclosed where relevant. Following this, the simulation results are presented and discussed. The combusting flow field and liner heat transfer are discussed, with interesting 3D effects noted. Most significantly, a strong interaction between wall cooling and the swirling flow was noted - as shown by Andreini *et al.* (2017*b*) and Gent (2018) for the pure effusion case. Finally, the CFD results were compared with those of the low order code, allowing discrepancies to be investigated.

4.1 Geometry

The geometry studied was an LDI combustor for a high bypass ratio turbofan, designed by Liu (2018). A single swirler segment of the combustor is shown in Figure 4.1a. Being an LDI combustor, air admission takes place through the swirler and cooling holes alone. Details of the swirler are shown in Figure 4.1b.

The inner liner wall is effusion cooled, while the outer liner wall is impingement/effusion cooled. This study considered only the outer liner wall cooling, allowing the computational domain to be simplified as shown in Figure 4.1c. Detail surrounding the diffuser, inner annulus, swirler vanes and inner wall cooling was removed.

In spite of the geometric simplifications made, with over 2000 sub-millimetre holes to keep track of, the geometric processing for this case was extremely challenging. ANSYS SpaceClaim® was unable to create the geometry and share topology between the fluid and solid domains. As such, the geometry had to be created in SolidWorks®. This does not, however, support the creation of multiple

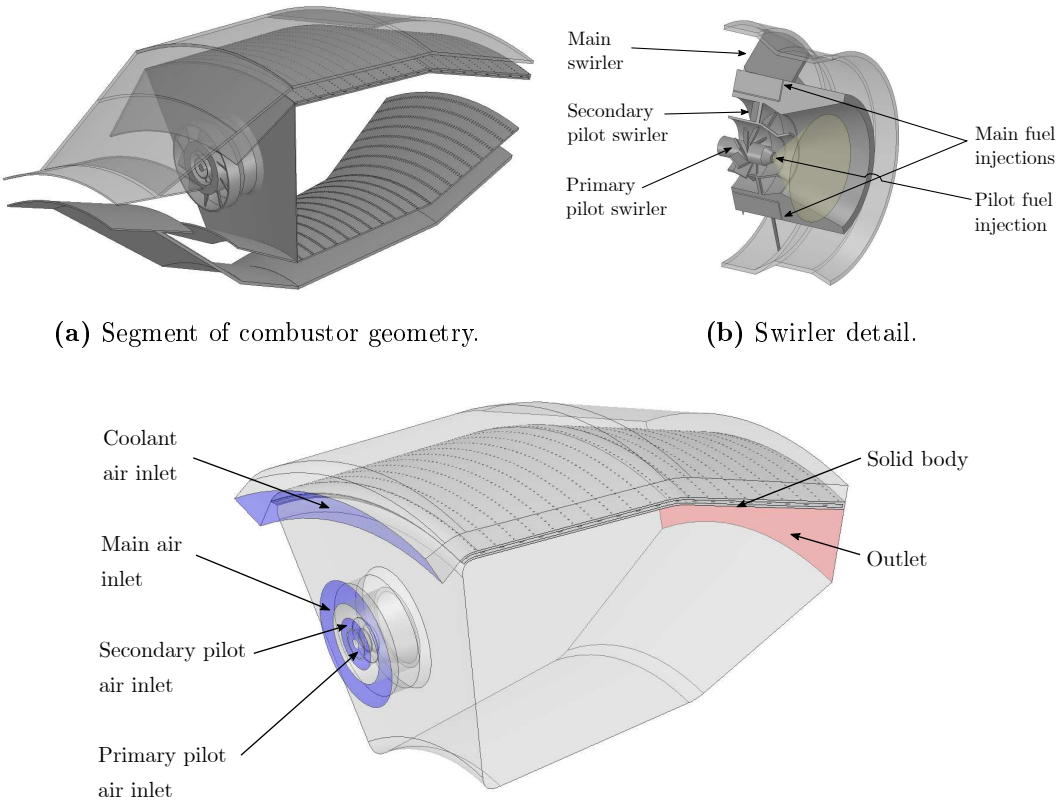

(a) Segment of combustor geometry.

(b) Swirler detail.

(c) Simplified computational domain.

Figure 4.1: Geometry of combustor to be studied.

zones with shared topology, as required by the CHT method. The solution was to draw the fluid zone in SolidWorks®, and create a series of patches in Fluent Mesher® to enclose the solid zone volume without explicitly importing CAD geometry for it.

4.2 Mesh

Sun (2018) performed a detailed mesh independence study on the geometry under consideration. This study informed the volume mesh generation for the current work. The impingement/effusion cooled wall was meshed in accordance with the parameters defined in Chapter 3.

The volume mesh was created using a series of bodies of influence to achieve local refinement where steep gradients were expected. Five bodies of influence were used to tailor the sizing near the injector in order to capture the complex physics taking place. The locations of these are highlighted in the mesh cross section shown in Figure 4.2.

As with geometric pre-processing, severe challenges were faced with mesh generation for this case. Fluent Mesher® was unable to generate a complete surface mesh for the fluid zone and reverted to the parasolid tessellation in a number of

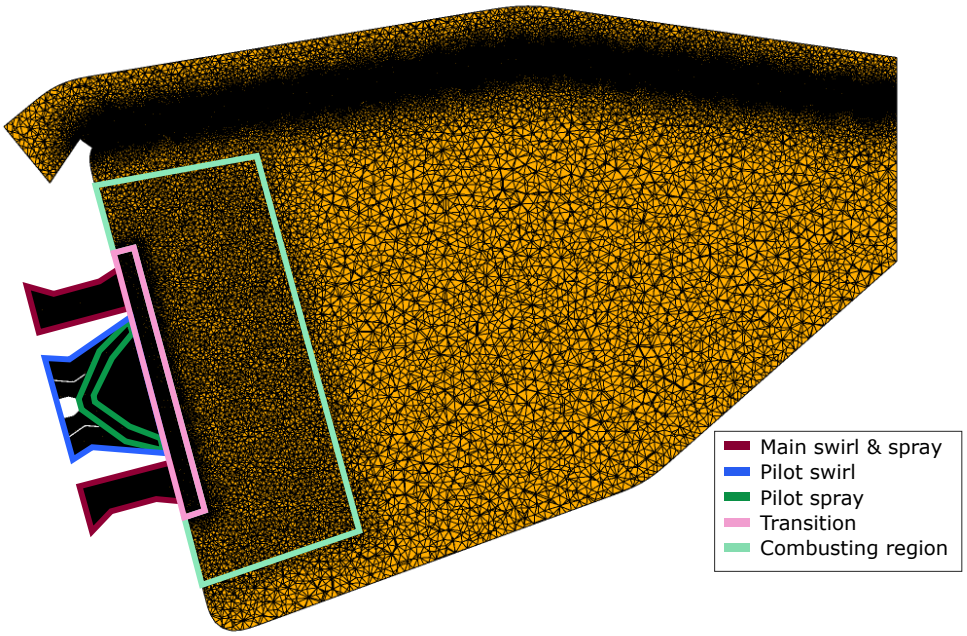

Figure 4.2: Cross section of mesh with locations of bodies of influence highlighted.

localised regions. The faces in these regions had to be deleted, manually patched and remeshed without losing geometric detail.

The volume mesh had a cell count just under 200 million, around 180 million of which were required for resolving the cooling detail. One of the largest penalties in cell count came from resolving the plate gap. Using 10 cells to span the gap enforced a cell size of 0.15 mm on the walls of the adjacent solid zones - far finer than required for hole resolution alone. This can be seen in Figure 4.3. Attempting to get 12 cells to span the gap increased the mesh size by 60 million cells, revealing the extreme sensitivity to this parameter. Unfortunately the validation study showed that this parameter could not be compromised on, so the mesh with 10 cells across the gap was used.

4.3 Boundary Conditions

Inlets

The swirler air was admitted via mass flow inlets on three boundary faces, as highlighted in Figure 4.1c above. Due to the geometric simplification of removing the swirl vanes, the swirler air was admitted as homogeneous, isotropic swirling flow. It should be noted that this simplification will place a limitation on the accuracy of the simulations performed. It was, however, necessary in order to make the computational problem tractable. Similarly, coolant air was admitted as homogeneous flow normal to the boundary.

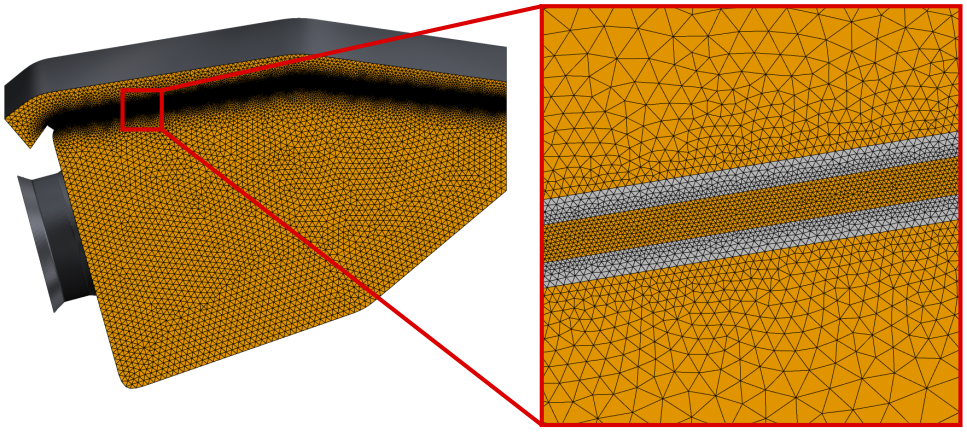

(a) Mesh on periodic boundary. Detail of mesh in plate gap inset.

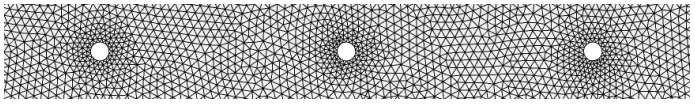

(b) Mesh on suction side of impingement wall showing natural cell growth.

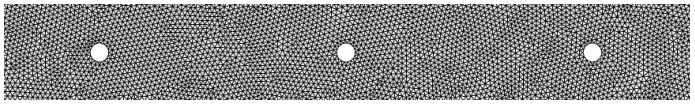

(c) Mesh on discharge side of impingement wall showing forced refinement due to gap resolution requirements.

Figure 4.3: Detail of the combustor case study mesh showing the impact of gap resolution.

Outlet

A static pressure outlet boundary condition was applied at the combustor outlet plane. The static pressure at the boundary was adjusted to achieve the required total pressure at the inlet.

Liner Edges

The selection of boundary conditions for the leading and trailing edges of the liner was somewhat more challenging than the experimental case.

It can be seen in Figure 4.1a above that the liner leading edge is connected to the snout and dome walls. It was assumed that these would remain well cooled, and have sufficient thermal mass to maintain a temperature near the compressor outlet temperature. As such, this was used for the thermal boundary condition at the liner leading edge.

No detail was provided for the interface at the liner trailing edge. As such, any assumption would be speculative, so the trailing edge was left adiabatic for this investigation.

4.4 Material Properties

Combustion Gas

The transport and thermodynamic properties of the combustion gas are summarised in Table A.2 in Appendix A.

Temperature and composition dependent properties were used throughout, with the exception of viscosity. This was done for consistency with previous modelling in this project. It is, however felt that the range spanned by the temperature field demands a temperature-dependent viscosity model. This should be investigated in subsequent research activities.

Hastelloy X

The temperature dependent material properties used to model Hastelloy X are summarised in Table A.3 Appendix A.

4.5 Solution

Turbulence Modelling

Turbulence modelling was a challenging issue for this case. As mentioned in Chapter 3, k-ω SST is desirable for CHT accuracy, but Realizable k-ε is preferred for stability when coupled with the FGM combustion model. An attempt was made to solve the combustor simulation using the k-ω SST model, but this was unsuccessful. As such, it was accepted that the Realizable k-ε model had to be used, albeit at a loss of accuracy.

Discrete Phase Modelling

The fuel spray was tracked transiently in the Lagrangian frame using the discrete phase model. Models for secondary break-up, evaporation and turbulent dispersion were used to improve the fidelity with which reactants were introduced into the combusting region.

Droplets were introduced with uniform diameter and velocity. While this is a limitation on the fidelity of the combustion simulation, it is unavoidable in the preliminary stage before injector characterisation has been carried out.

The pilot injector was modelled as a ring-cone injection. Secondary droplet breakup in the pilot spray was modelled with the wave breakup model. This is suited to modelling breakup in high Weber number sprays and is a commonly used model for cone injections, as shown by Guildenbecher *et al.* (2009) and Hossainpour and Binesh (2009). The model links the breakup of a droplet to the growth of Kelvin-Helmholtz instabilities due to aerodynamic forces.

To capture the main injector spray, a series of surface injections were used. Breakup in the main spray was modelled with the KHRT model, which is an adaption of the wave model. The KHRT model adds a second criterion for breakup, which is linked to the growth of Rayleigh-Taylor instabilities due to rapid droplet

acceleration. This is more suitable for the main injection, as the jet is injected into cross-flow, as shown by Guildenbecher *et al.* (2009) and Hossainpour and Binesh (2009). As such, the particles will be subject to both aerodynamic forces and rapid acceleration.

Combustion Modelling

The reacting flow was modelled as a partially premixed flame using the flamelet generated manifold model. A skeletal chemical mechanism developed by Vié *et al.* (2015) was used for reaction modelling. The mechanism uses 14 species and 18 reactions to represent the combustion of Jet A1, for which n-dodecane is used as a surrogate.

The FGM model takes a statistical approach to turbulent combustion, postulating that a turbulent flame brush can be represented as a conglomeration of laminar flamelets. The chemistry of these laminar flamelets is pre-calculated, and a probability density lookup table is generated. This allows the chemical reactions to be represented with just four transport equations: the mean mixture fraction, mean reaction progress and their respective variances.

The FGM model has been validated against experimental data collected from laboratory combustors, the geometries of which are representative of the LDI combustor under consideration (Proch and Kempf (2015); Puggelli *et al.* (2016); Oijen *et al.* (2016)). Andreini *et al.* (2015*b*) compared the predictive capability of the FGM model when combined with both RANS and LES turbulence modelling. The umerical results were compared to experimental data collected from a three-segment LDI combustor test rig. While the LES results were more accurate, the RANS approach was able to reconstruct temperature profiles with an average normalised error of 14%. Discrepancies in the RANS temperature profiles were largely attributed to errors in the velocity field and droplet distributions.

Numerical Treatment

The simulations were conducted with a coupled pressure based solver and second order spacial discretisation for all equations. Due to the nature of the physics being simulated, a fair amount of under-relaxation was required to maintain solution stability. It was found that momentum, eddy dissipation, eddy viscosity and discrete phase sources required significant under-relaxation - a factor of 0.3. The remaining relaxation factors were maintained above 0.5, with temperature at 0.6 and energy at 0.9.

Convergence

Convergence was monitored via residuals, surface monitors and visual inspection of contours at regular intervals. All residuals were required to reduce by at least three orders of magnitude. The energy residual was required to reduce by at least six. In some cases this was insufficient, and the solution continued to change once this was reached. In these cases, surface monitors were used to judge convergence with mean, maximum and minimum wall temperature, as well as heat and mass

flux imbalances monitored. In addition to this, contours of temperature and reaction progress were plotted at regular intervals and compared with prior plots to assess qualitative changes in the flow field.

Computation

The simulation was run on 480 cores at the CHPC. The baseline simulations without radiation modelling required around 800 GB of RAM. The computation took approximately 50 wall clock hours to perform 10 000 iterations, at which point the solution had converged.

4.6 Results

In order to provide context for the results, the combusting flow field will first be introduced. Following this, a detailed investigation of the liner heat transfer will be presented.

Plots presented in this section will be extracted from two locations, shown in Figure 4.4a. Contours plotted on the combustor mid-plane will be used to investigate the flow field. Contours plotted on the liner walls will be used for detailed heat transfer investigations. These plots will be presented as per Figure 4.4b, which shows the discharge side of the effusion wall as viewed from the combustor axis. Air flow is from left to right, and the swirler body will be shown in order to provide context.

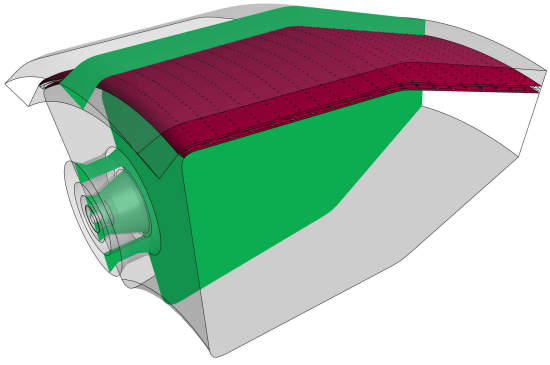

(a) Reporting surfaces: combustor mid-plane in green, liner walls in red.

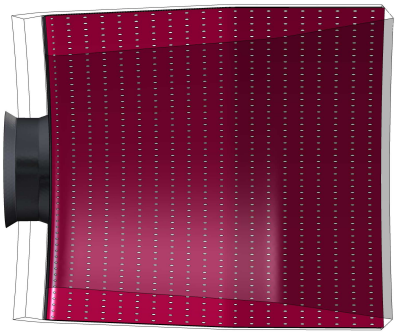

(b) Typical view used to report liner wall details.

Figure 4.4: Locations used for reporting combustor simulation results.

4.6.1 Flow Field

A slice of the temperature field is shown on the combustor mid-plane in Figure 4.5a. Reading this in conjuction with contours of mean mixture fraction and progress variable, shown in Figures 4.5b and 4.5c respectively, reveals the behaviour of the combustor.

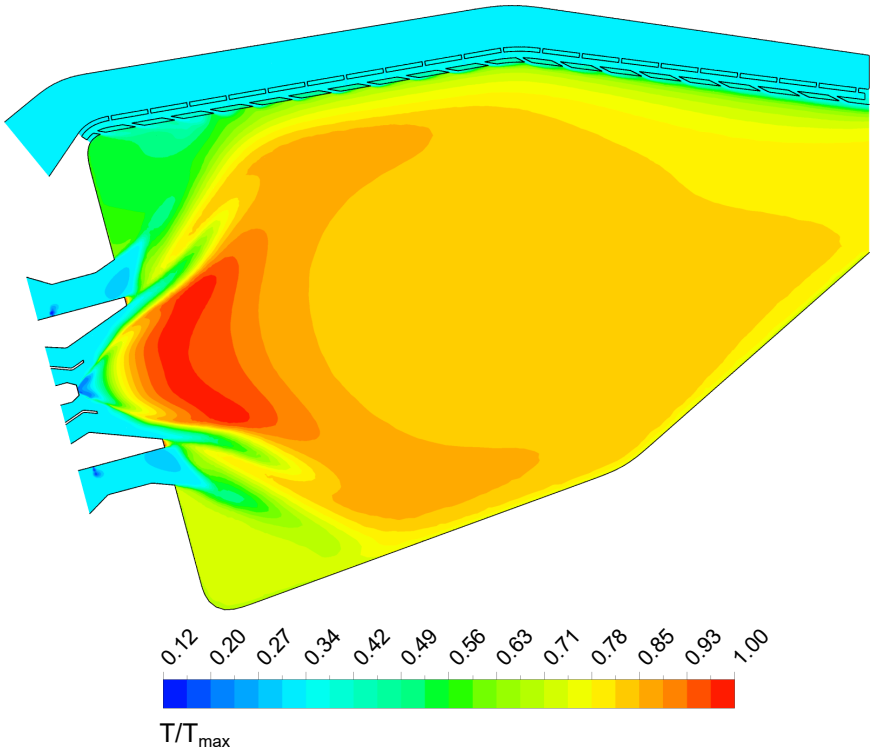

(a) Temperature field on combustor mid-plane.

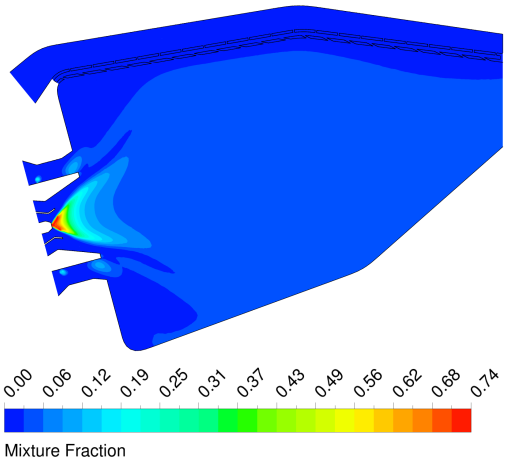

(b) Mixture fraction on combustor mid-plane.

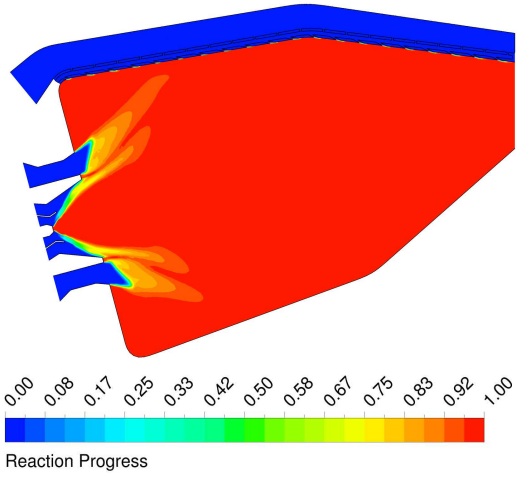

(c) Reaction progress on combustor mid-plane.

Figure 4.5: Combustion characteristics of the combustor under consideration.

Immediately downstream of the pilot injection, rapid evaporation of atomised fuel results in an extremely rich region. While reactions are locally complete in this region, the high mixture fraction and heat removed due to evaporation result in low temperatures. Moving downstream, the mixture is leaned out allowing more of the fuel to react, and the temperature increases rapidly. The result is a small region of extremely high temperature, anchored to the swirler. This characterises the pilot flame.

Similarly in the main burner, cold spots can be seen at the injection locations due to droplet evaporation. These cold trails quickly move out of plane as the swirling flow carries the droplets along a helical path. Droplets from the neighbouring injector are brought into plane just at the swirler outlet, leaving a second set of cold spots. Unlike the pilot flame, combustion does not take place immediately downstream of the main burner injectors. This is due to the fact that the turbulent flame speed is insufficient for the flame to propagate up the swirler. This feature of the LDI combustor allows for a limited amount of pre-mixing to take place, facilitating more even combustion which is vital for emissions control.

Downstream of the swirler assembly, as the swirling flame spreads it is eventually confined by the liner walls. Here it is important to note the differences between the behaviour at the inner and outer walls. At the outer wall, the air entering the liner through the cooling holes leans out the mixture, resulting in a local temperature reduction. This confines the high temperature region to a central bubble. With the inner liner cooling features omitted, this behaviour could not be resolved. Instead it was forced using an isothermal wall boundary condition (this is presented and justified in Chapter 5). As such, the flame behaviour at the inner wall is likely not completely realistic. The impact of this was not studied in the current work.

The temperature contours provide a misleading representation of the interaction between the swirling flow and the wall. From Figure 4.5a above, one may assume that the cooling film is able to offset the swirling flow, preventing it from impinging on the wall. This is not the case, as is revealed by the velocity vectors in Figure 4.6. The swirling flow clearly spreads until it impinges on the outer wall, unrestricted by the cooling film.

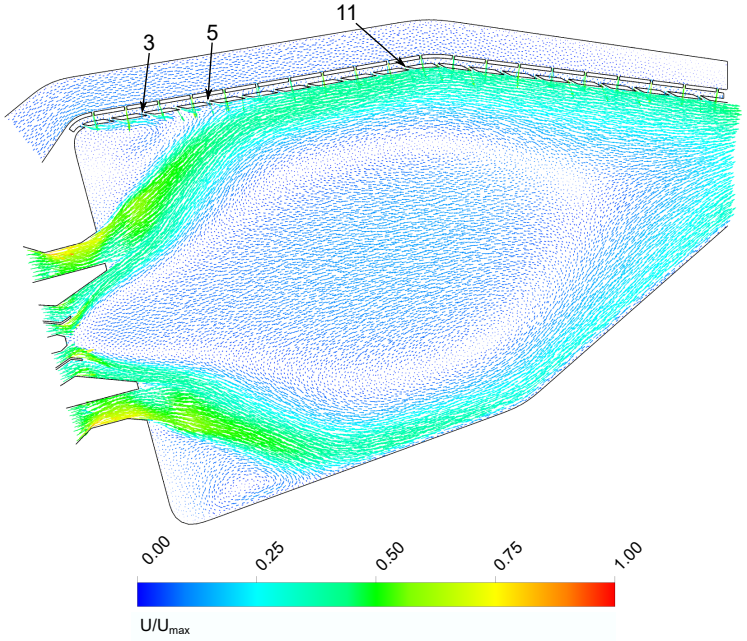

Figure 4.6: Velocity vectors on combustor mid-plane.

As pointed out by both Andreini *et al.* (2017*b*) and Gent (2018), the impingement of the swirling flow was expected to have an adverse effect on the cooling film. The interaction can be seen in the line integral convolution (LIC) of near wall velocity shown in Figure 4.7. For reference, the undisturbed progression of the cooling film can be seen at the periodic extremities. Ideally, near wall velocity would gradually increase from zero to maximum as additional air is injected and the film strengthens.

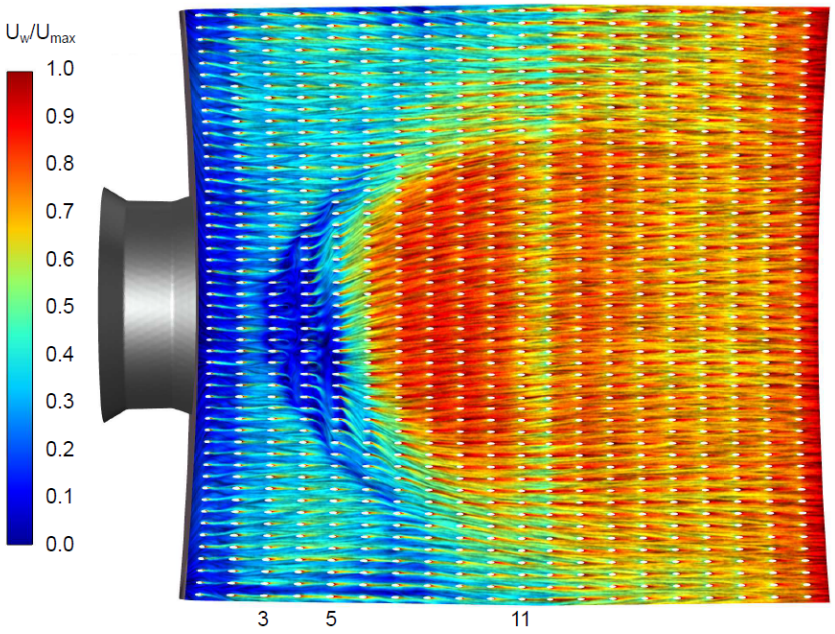

Figure 4.7: Line integral convolution of near wall velocity.

The swirl interaction can be seen beginning at row 3 and in line with the swirler shroud. Between rows 3 and 5 there exists a parabolic region of low velocity. Cross-referencing the velocity contours in Figure 4.6 above, it is clear that this is upstream of the impingement point. It appears that the film is entrained as the swirling flow approaches the wall, leading to the film detaching from the wall. This is evidenced by the chaotic and incomplete LIC streaks in this region, coupled with negligible near wall velocity.

At row 5, the swirling flow impinges on the wall. This results in a region of high near wall velocity which is most noticeable up to row 11. Beyond row 11 the disturbance is present, though far less severe. The high near wall velocity, coupled with the elevated temperature of the swirling flow, is expected to result in a region of high wall temperatures due to increased convective heat transfer.

A final interesting note regarding the flow field is the total pressure distribution on the mid-plane, presented in Figure 4.8. Having adjusted the outlet static pressure to achieve the correct total pressure at the swirler inlet, the annulus pressure was allowed to rise to the level required to drive the coolant mass flow through the liner. It was noted that the total pressure in the annulus implied an 11.3% pressure drop over the combustor. While the expected value could not be

obtained, it can be speculated with fair confidence that this was not the design intent, as the design goal for pressure drop is usually below 7% (Lefebvre and Ballal, 2010).

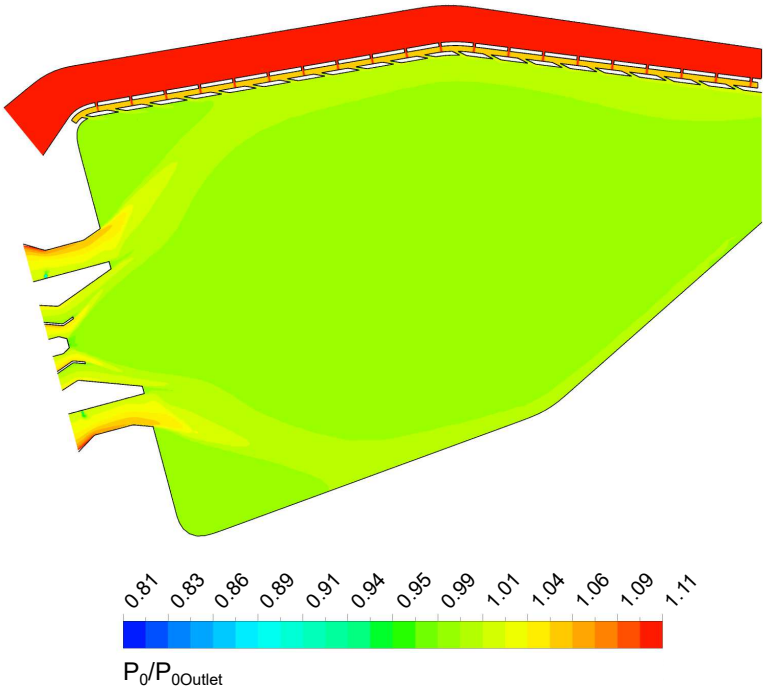

Figure 4.8: Contours of absolute total pressure on the combustor mid-plane.

Considering that it was shown in Chapter 3 that the pressure drop is under-predicted using this analysis method, it can be said that the true pressure drop is even greater than 11%. As such, it is speculated that the low order code is significantly under-predicting the pressure drop across the cooling mechanism. This should be investigated further, as it will reduce the service life of a combustor designed using this tool. In a complete system, the coolant mass flow rate delivered would be lower than the design value, resulting in liner walls operating at higher temperatures.

4.6.2 Outer Liner Thermal Study

Temperature contours are plotted on the discharge side of the effusion wall in Figure 4.9. The thermal effect of the swirl interaction is immediately evident from the central high temperature region. An iso-contour of the limit temperature for the liner material has been overlaid in black. It can be seen that a sizeable portion of the liner exceeds the limit temperature due to the swirl impingement.

Before investigating the swirl interaction further, the severe thermal gradient should be noted at the leading edge of the liner wall. This reveals that the selection of leading edge thermal condition was perhaps a poor one. The steep thermal gradient would likely not be sustained by the convective cooling at the

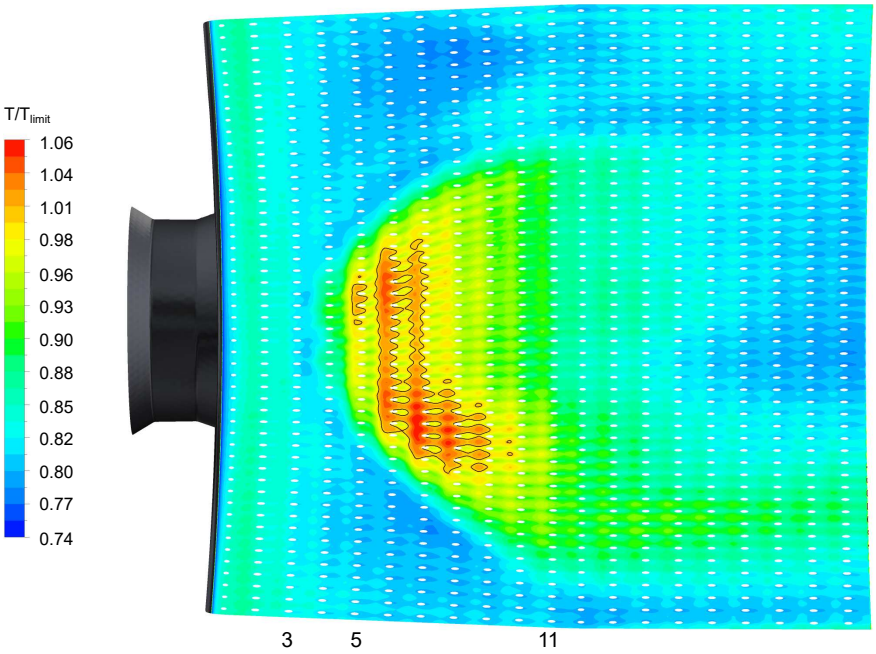

Figure 4.9: Temperature contours on the discharge side of the effusion wall.

snout. It seems more likely that the snout wall would heat up to some intermediate temperature, along with the liner leading edge. Without including this detail in the simulation, it would be difficult to improve the current approximation. Moreover, the impact was deemed insufficient to warrant repeating the simulations, given the extreme computational cost. As such, this thermal condition was maintained for all combustor simulations.

Examining the swirl interaction once again, it can be seen that shortly after film detachment at row 3, the temperature of the unprotected wall begins to rise. Following impingement at row 5, the wall temperature increases drastically, likely due to increased convective heat transfer as postulated above. The thermal effect of the swirl impingement persists, to varying extent, until the combustor outlet.

The heat flux through the effusion wall is shown in Figures 4.10a and 4.10b for the discharge and suction sides respectively. In the convention used, a positive heat flux indicates heat flowing into the wall. It should be noted that the peak heat flux from this set of results has been used as a reference value to non-dimensionalise all further heat flux plots.

As expected, the impingement zone is characterised by increased heat flux due to both the film disturbance and the increased convection. Fortunately, the higher wall temperature improves the impingement cooling on the suction side of the effusion wall, as seen in Figure 4.10b. While the liner limit temperature was exceeded, it is clear that this would have been significantly worse without the augmented convective cooling on the suction side.

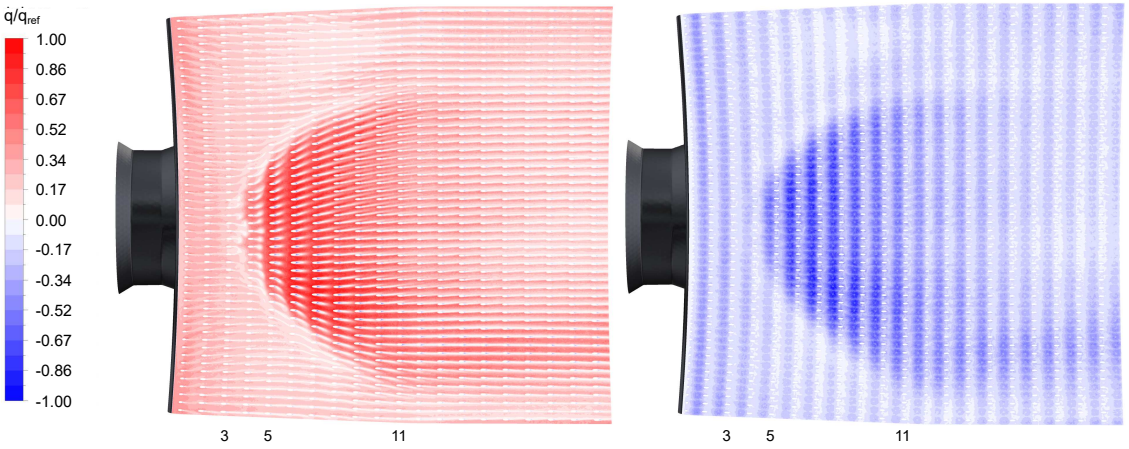

(a) Heat flux through discharge side of effusion wall.

(b) Heat flux through suction side of effusion wall.

Figure 4.10: Effusion wall heat flux.

To facilitate comparison with results from the low order code, circumferential averages of liner temperature were taken. These are plotted in Figure 4.11 with results obtained from the low order code overlaid.

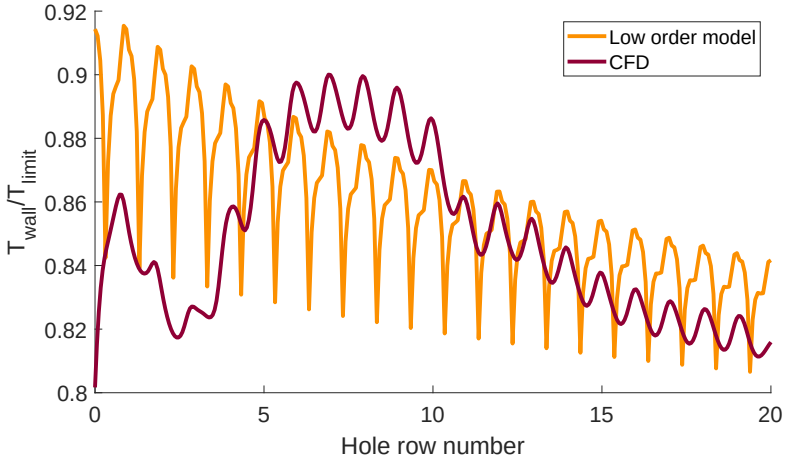

Figure 4.11: Circumferentially averaged temperature on the discharge side of the effusion wall.

Once again, the poorly selected boundary condition imposed at the leading edge is evident. It can now be seen that the induced thermal gradient is far steeper than throughout the remainder of the wall. This confirms the non-physical condition, which is a shortcoming of the present work.

Upstream of row 5, it can be seen that the low order code over-predicts wall temperature. The velocity vectors in Figure 4.6 above show negligible near wall velocity in this region. In contrast to this, the low order model assumes a constant bulk velocity throughout the wall length. As a result of this assumption, the low

order code over-predicts convective heat transfer in this region, leading to higher wall temperatures.

Between holes 5 and 10, the low order code under-predicts wall temperature. This is expected, as it cannot account for the swirl impingement which leads to the excessive wall temperature in this region.

Downstream of hole 10, the flow field tends towards the ideal case, with minimal 3D effects. As such, the temperature predictions correlate well toward the trailing edge.

A final noteworthy difference between the two analyses is the magnitude of the thermal gradients. The large thermal gradients predicted by the low order model suggest a substantially higher Biot number. Unfortunately, access to the low order code and its underlying methods and assumptions could not be attained. As such, the root cause of this discrepancy can only be speculated at this stage. One could propose that the discrepancy is due to the omission of radiation modelling in the current simulations. This will be investigated in Chapter 5 below. Alternatively, it could be due to an under-prediction of conduction in the liner plane, or an over-prediction of convective and radiative fluxes in the low order code. This will require further investigation.

While the focus of the study was the effusion wall, as it is subject to severe thermal loading, the impingement wall will be briefly discussed. Temperature contours are plotted on the suction side of the impingement wall in Figure 4.12a. Surface heat flux contours are plotted on the discharge and suction sides of the impingement wall in Figures 4.12b and 4.12c respectively.

The temperature contours reveal that the hot region on the effusion wall is transferred to the impingement wall, though to a significantly reduced extent. Recalling that this simulation did not account for radiative heat transfer, the transfer mechanism must have been convection. This can be seen in Figure 4.12b, which shows increased heat flux in this region. The structures seen on the surface reveal the transfer mechanism as being due to the vortices created by the impingement jets, similar to those discussed in Chapter 3. Having removed heat from the effusion wall, the vortices roll over and make contact with the impingement wall, transferring a portion of the heat.

Figure 4.12c reveals that the convective cooling due to the annulus flow is minimal. This is due to both the low annulus velocity, and the fact that the wall and bulk fluid temperatures are fairly similar.

A final noteworthy feature is the impingement plate trailing edge. This is somewhat hotter than the remainder of the wall, due to the thermal contact with the effusion plate. The joint connecting the walls allows conduction from the effusion to the impingement wall. As a result of the high wall temperatures, the effect of cooling can be seen in the heat flux contours at the trailing edge, on both sides of the wall.

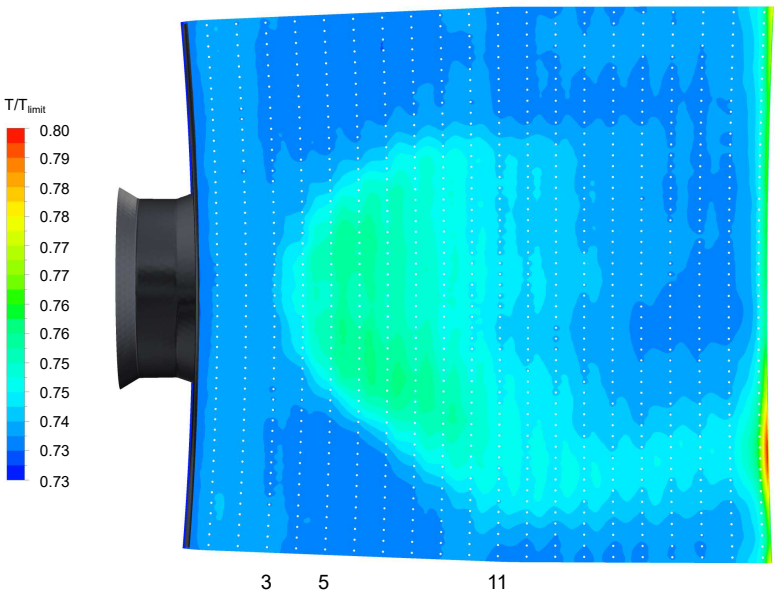

(a) Temperature contours on suction side of impingement wall.

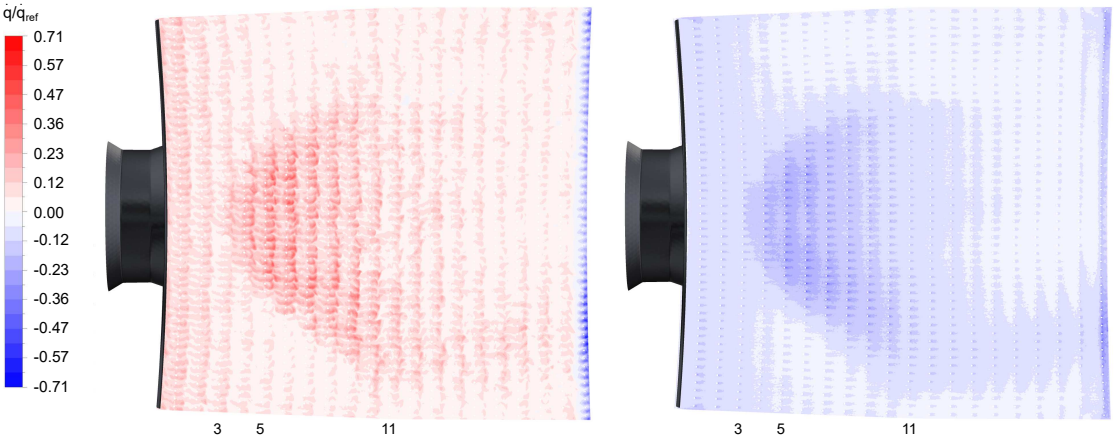

(b) Heat flux through discharge side of impingement wall.

(c) Heat flux through suction side of impingement wall.

Figure 4.12: Impingement wall temperature and heat flux.

4.7 Summary

The multiphysics modelling of a lean direct injection combustor was successfully carried out. The simulation included modelling for turbulence, spray with secondary break up and evaporation, combustion chemistry and conjugate heat transfer to an immersed solid body. Radiation modelling was omitted in the simulations discussed in this section.

The simulations revealed strong interaction between the cooling film and the swirling flow. The swirling flow impingement was shown to disturb the film and cause a local increase in convective heat transfer. As a result, the cooling mechanism was unable to maintain acceptable metal temperatures throughout the liner wall.

The results were compared to those of a low order model and four main discrepancies were highlighted. The first two were due to the inability of the low order code to account for 3D effects, namely the low velocity near the dome and the swirl impingement. This resulted in differences in liner temperature prediction between the two models. The third discrepancy was in the Biot number predicted in the two simulations. Due to a lack of information regarding the low order code, the root cause of this could not be determined. Finally, it is suspected that the low order code under-predicted the pressure drop across the liner wall. As a result, the cooling holes specified are too small and if the full system was to be modelled or tested, the design cooling mass flow rate would not be met.

Chapter 5

Impact of Radiation Modelling

The following chapter outlines a study to determine the necessity of including radiation modelling when performing CHT simulations on a combustor liner. The simulations described in Chapter 4 were repeated with the inclusion of radiation modelling. It should be noted that the geometry, mesh, boundary conditions and setup were kept consistent with those presented in Chapter 4. Any differences are summarised below, following which the results are presented.

5.1 Boundary Conditions

Given that radiation modelling was to be investigated, it was important that representative temperatures were applied to all walls in the domain. For consistency, the same boundary conditions had been applied to the simulations described in Chapter 4 above. Although they were used in the previous simulations, the boundary conditions are presented in the current section as their selection was driven by radiation modelling.

Inner Liner Wall

The inner liner wall participates in radiative exchange with the combustion gas and the outer liner wall. If left adiabatic, the extreme wall temperatures would result in an over-prediction of radiative emission. As such, representative wall temperatures are necessary when including radiation modelling. For practical purposes the inner liner wall temperature was set to the average wall temperature obtained in the simulations performed by Gent (2018). This simplification limits the accuracy of the radiation modelling, as the hot spots on the inner liner wall were not captured.

Combustor Casing

The temperature of the combustor casing was assumed to be the compressor outlet temperature. This is common practice in thermal modelling of combustor liners, and is the condition recommended by Lefebvre and Ballal (2010). This is

unlikely to have a significant impact on the temperature of the effusion wall and the sensitivity to this assumption was not investigated.

Turbine Stator Radiation

It was expected that the turbine stator would present an appreciable radiation source. While this is external to the domain, it can still be accounted for as a radiation source at the domain outlet. A metal temperature of 1250 K and emissivity of 0.6 were assumed. This would vary based on the selection of turbine alloy, as well as surface condition. The current estimate is based on typical temperature limits and emission properties for nickel-based alloys, informed by Donachie and Donachie (2002).

5.2 Material Properties

Combustion Gas

As noted in Table A.2, gas phase emissivity was calculated using the weighted sum of grey gasses model. This was selected in accordance with the findings of the literature review in Chapter 2 and was not investigated further. While this does not account for the variations in spectral content emitted by different species, it is the most comprehensive model that remains computationally tractable.

Hastelloy X

The temperature dependent radiative properties of Hastelloy X have been included in Table A.3. It should be noted that there is some uncertainty regarding the emissivity of the liner walls. Emissivity is sensitive to the surface condition of the wall, which is difficult to estimate at this stage. Among other factors, emissivity is sensitive to the wall temperature, the amount of oxidation and the level of soot fouling. A combustor wall is expected to be severely thermally oxidised, but the level of soot fouling is difficult to model or estimate. Soot deposits will blacken the wall, making the emissivity tend to a value of one, thereby maximising radiative heat transfer. As such, two extreme cases were analysed: walls with no soot fouling and walls completely covered in soot. It is expected that a realistic solution will lie within the bounds of these two solutions. It should be noted that only walls exposed to combustion gas were assumed to be affected by soot fouling.

In addition to emissivity, the Discrete Ordinate (DO) radiation model requires an estimate for the ratio of diffuse to specular reflected radiation. Unfortunately no data could be found for this, so it was estimated based on visual inspection of a typical Hastelloy X combustor. It was noted that the oxidised material exhibited almost no reflectivity or sheen, so a diffuse fraction of 1 was estimated. This has the added benefit of simplifying the radiation modelling, as specular reflections need not be tracked. The validity of and sensitivity to this assumption was not investigated further.

5.3 Solution

Radiation Modelling

As proposed in Chapter 2, the discrete ordinates radiation model was used for this study due to its compatibility with combustion modelling. The DO model requires the user to define the number of angular divisions used to discretise each octant of the unit sphere. This must be defined for each angular direction, θ and ϕ, as illustrated in Figure 5.1. The sensitivity to angular discretisation was investigated in this study. Two levels of discretisation were assessed: two and four divisions in each angular direction. This results in a total of 32 and 128 control angles respectively.

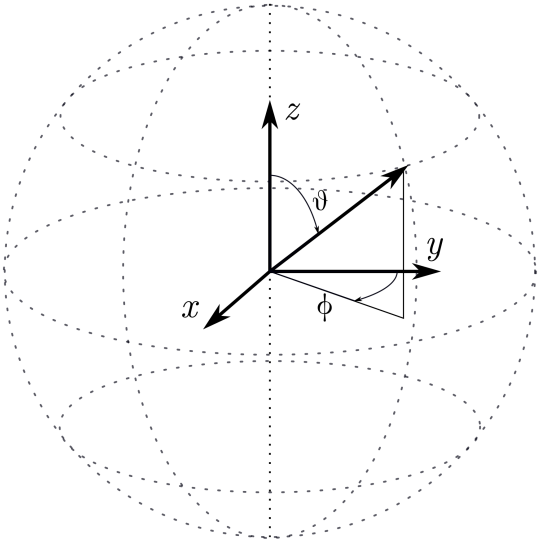

Figure 5.1: Angular coordinate convention used in the DO model.

In addition, the user must specify a number of pixels in each angular direction, which are used to prevent control volume overhang. This is particularly important when dealing with specular reflections, significant refraction or scattering. While only limited scattering due to droplets was expected in this case, the sensitivity to pixelation was investigated. Two pixel densities were assessed: one and three pixel divisions in each angular direction. These were selected as they are the default and generally recommended values respectively.

It should be noted that angular discretisation and pixel density were not assessed in isolation. To reduce the number of computations required, only two models were run: a coarse model with 32 control angles and a 1x1 pixel grid, and a fine model with 128 control angles and a 3x3 pixel grid.

Finally, the user must specify the frequency with which the radiation transport equation is solved. The default value of 10 energy iterations per DO iteration was used. The sensitivity to this was not investigated, but is expected to be low over sufficiently many iterations.

Numerical Treatment

Second order spatial discretisation was applied to the DO transport equation. The DO equation was found to be stable in all cases, and an under-relaxation factor of 0.9 was found to be suitable.

Computation

As above, the simulations were solved using 480 cores. The inclusion of radiation modelling increased computational cost substantially. The average time per iteration and RAM requirement for each simulation is summarised in Table 5.1. The impact on computation time was moderate, but the increased RAM overhead was severe. This was particularly pronounced in the fine radiation model.

Table 5.1: Summary of computational requirements for radiation modelling.

Simulation	Time per iteration [s]	RAM requirement [TB]
No radiation	18	0.8
Coarse radiation	20	1.1
Fine radiation	26	1.9

Fortunately, it was found that the radiative effects converged quickly in comparison with combustion modelling. As such, each additional simulation could be initialised from the converged combustion simulation, decreasing the number of iterations required to achieve convergence.

5.4 Results

The results from three simulations will be presented in this section. The first will be referred to as the baseline simulation. This employed the coarse radiation modelling and assumed soot-free, thermally oxidised liner walls.

The second simulation assessed the impact of increased liner emissivity due to soot fouling. This model employed the coarse radiation modelling but emissivity was set to a value of one on all walls which are exposed to combustion gas.

The final simulation assessed the impact of spacial discretisation in the DO model. This employed the fine radiation modelling and emissivity was maintained at a value of one on the walls exposed to combustion gas. This was done to maximise the radiative heat transfer, thereby emphasising any discrepancies due to radiation modelling fidelity.

5.4.1 Baseline Simulation

Flow Field

The inclusion of radiation modelling had practically no impact on the behaviour of the flow field. Contours of flow and combustion variables plotted on the mid-plane are indistinguishable from those presented above and will not be repeated.

The key sources of radiation can be seen in Figure 5.2, which shows contours of volumetric emitted radiation. It is clear that the pilot flame is a significant radiation source due to its extreme temperature. It should be noted that this simulation did not account for the soot which would likely be present in the pilot flame. As such, the radiation intensity emitted from the pilot flame would likely be even higher in reality due to the black body emission of the soot particles.

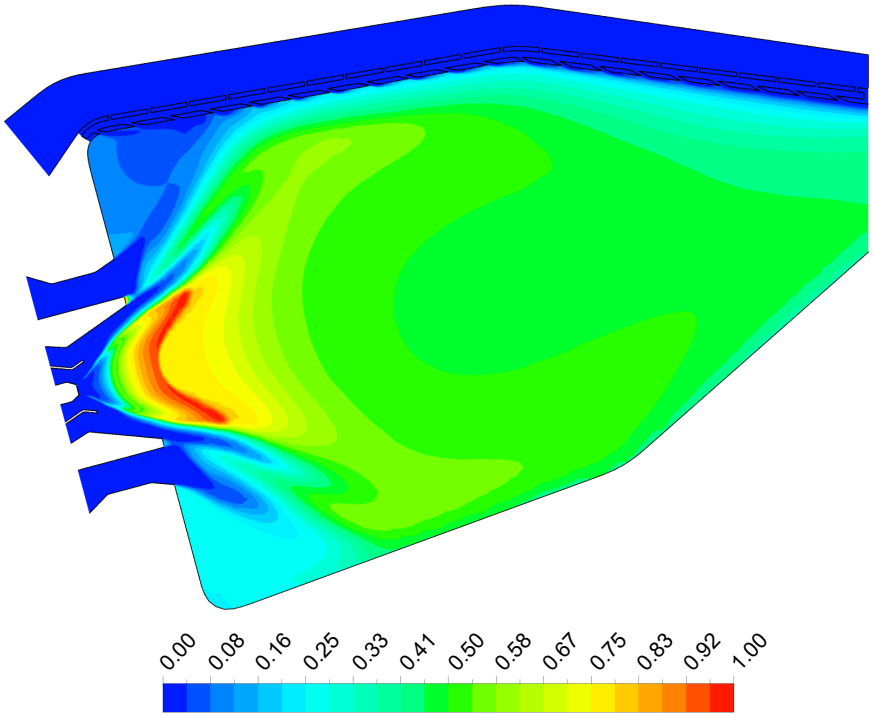

Figure 5.2: Contours of volumetric emitted radiation on the combustor mid-plane.

Downstream of the pilot flame, the combustion gas is at a fairly uniform temperature. This results in an almost constant radiation emission throughout the remainder of the combustor. One noteworthy region is where the inner liner meets the dome. This simulation predicted higher emission in this region compared with the outer corner. This is simply due to the omission of inner liner cooling air, which resulted in higher temperatures in this region.

Outer Liner Wall

Temperature contours are plotted on the discharge side of the effusion wall in Figure 5.3a. For comparison, the same plot without radiation modelling is repeated in Figure 5.3b. Comparing the two figures, an overall increase in liner temperature due to radiation modelling can be seen. Most notably, the region in which the temperature exceeds the material limit has expanded considerably. This reveals the non-conservative nature of neglecting radiation modelling when assessing combustor component temperatures.

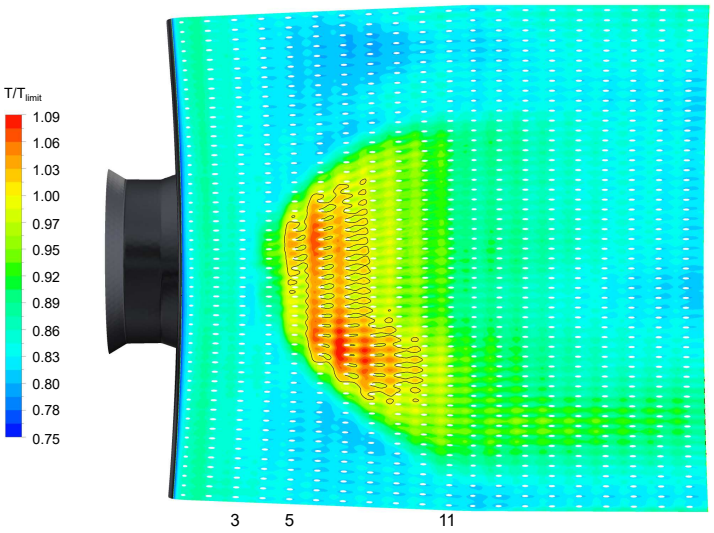

(a) Coarse radiation modelling, no soot fouling.

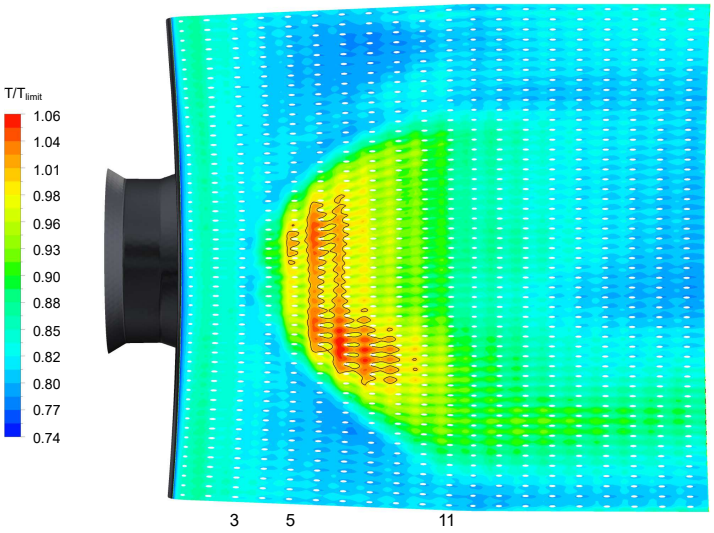

(b) No radiation modelling.

Figure 5.3: Temperature contours on the discharge side of the effusion wall with and without radiation modelling.

The reason for increased liner temperatures can be seen in Figure 5.4a and 5.4b, which plot radiative heat flux on the discharge and suction sides of the effusion wall respectively. Two features should be noted. The first is that the liner absorbs roughly an order of magnitude more radiation than it emits on the suction side. To reach thermal equilibrium, the wall temperature must increase until the convective cooling can remove the surplus heat flux. The radiative fluxes are, however, an order of magnitude lower than those due to convection. As such the increase in liner temperature is moderate.

The second noteworthy feature is that Figure 5.4a does not exhibit the characteristic pattern due to swirl impingement. The radiative heat transfer was expected to be impacted by this phenomenon as both radiative flux and liner emissivity are functions of temperature. The feint swirl impingement features

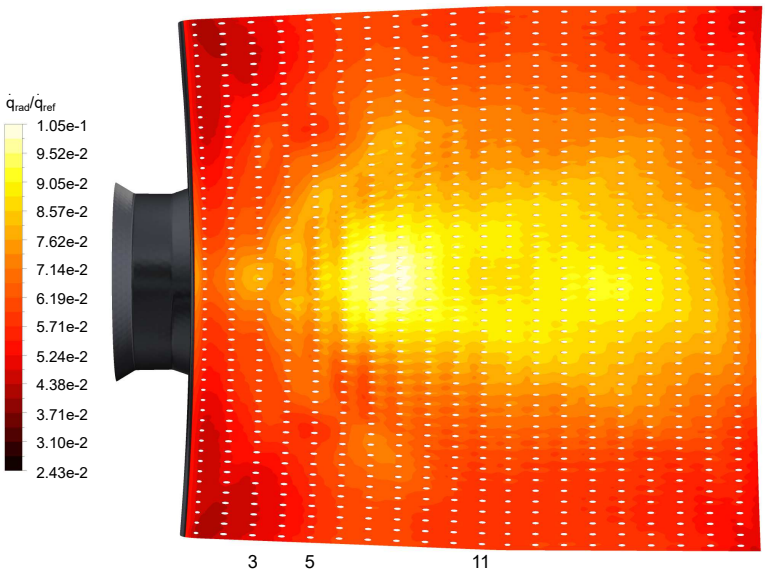

(a) Absorption on the discharge side of the effusion wall.

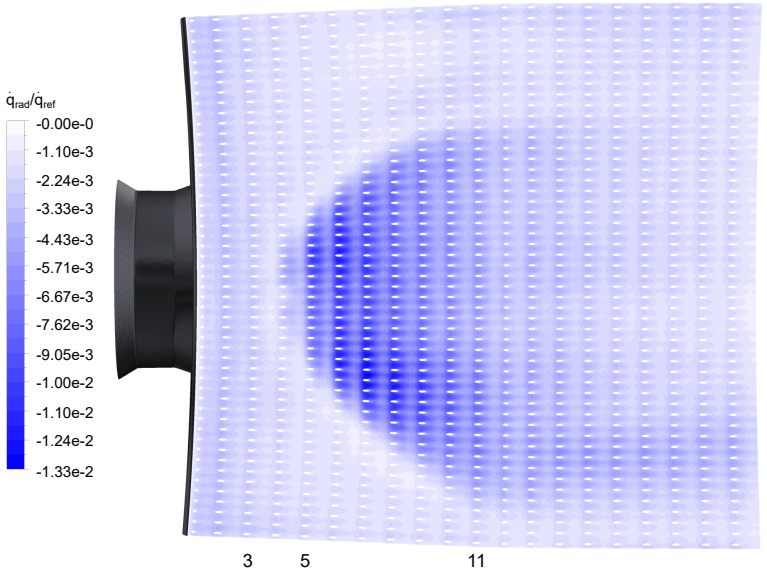

(b) Emission on the suction side of the effusion wall.

Figure 5.4: Radiative heat flux through the effusion wall.

show that these effects are present, but secondary. It seems that the driving variable is the view factor to the pilot flame. This results in a streak down the centre line, where the view of the pilot flame is largely unshielded by the swirler walls. The width spanned by this streak is, however, narrower than would be expected. This is likely due to the limited number of control angles being used in the current simulation.

Circumferentially averaged plots of wall temperature are presented in Figure 5.5. The results from the case without radiation, as well as the low order model are overlaid. As was indicated by the contours, an overall increase in temperature can be seen with the inclusion of radiation modelling.

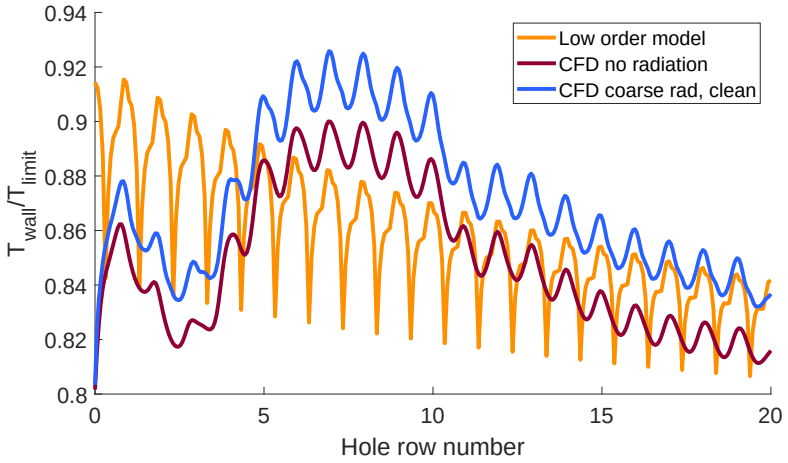

Figure 5.5: Circumferentially averaged temperature on the discharge side of the effusion wall showing impact of radiation modelling.

In addition to the increased wall temperature, comparing the two CFD solutions reveals a slight increase in Biot number. This is evident from the sharper peaks, steeper thermal gradients and larger thermal fluctuations. The increase is minor, as radiation only contributed around 15% of the total heat flux in this case. As such, the Biot number discrepancy between the low order model and CFD noted in Chapter 4 was not due to the omission of radiation modelling, and the root cause should be sought in the low order code.

5.4.2 Effect of Soot Deposits

The baseline simulation was repeated with the assumption that the inside walls of the liner were completely blackened by soot, leading to an emissivity of one. The emissivity of the remaining walls was unchanged. The changes to wall emissivity had no impact on the flow field, so only results from the liner walls will be presented in this section.

The temperature distribution on the discharge side of the effusion wall can be seen in Figure 5.6. As expected, the soot fouling led to an overall increase in wall temperature - 6.4% on average. In addition to this, the region in which the material limit temperature is exceeded has expanded further.

Contours of absorbed radiative heat flux are shown in Figure 5.7. This reveals that a soot fouled wall absorbs roughly 2.5 times more the radiative heat flux than a clean wall. This is mainly due to the fact that the emissivity approximately doubles. With the suction side remaining soot-free, it cannot efficiently reflect the incoming radiation. This leads to an increase in liner temperature until thermal equilibrium is once again reached. Contours of radiative heat flux have not been plotted on the suction side of the effusion wall as they are almost identical to those in Figure 5.4b above.

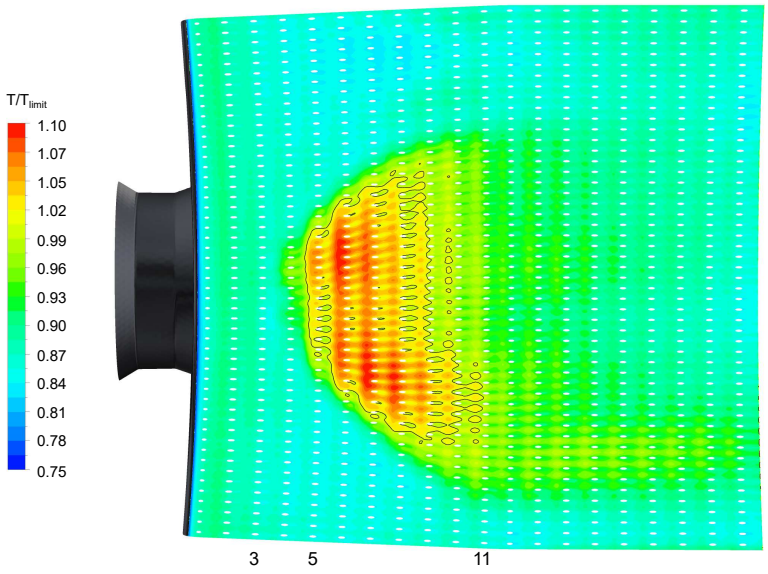

Figure 5.6: Temperature contours on the discharge side of the effusion wall with coarse radiation modelling and soot fouled walls.

As with the soot-free simulation, the peak radiative flux is confined to a narrow streak down the centre line. As discussed above, this streak seems to be artificially narrow due to the limited number of control angles used in the DO equations. In this case, however, the streak widens toward the plate trailing edge. This portion of the liner has a relatively low temperature, which led to a low emissivity in the clean wall simulation. As such, the majority of the incident radiation was previously reflected. In the current simulation, all of this incident radiation is absorbed, leading to a higher radiative flux in this region.

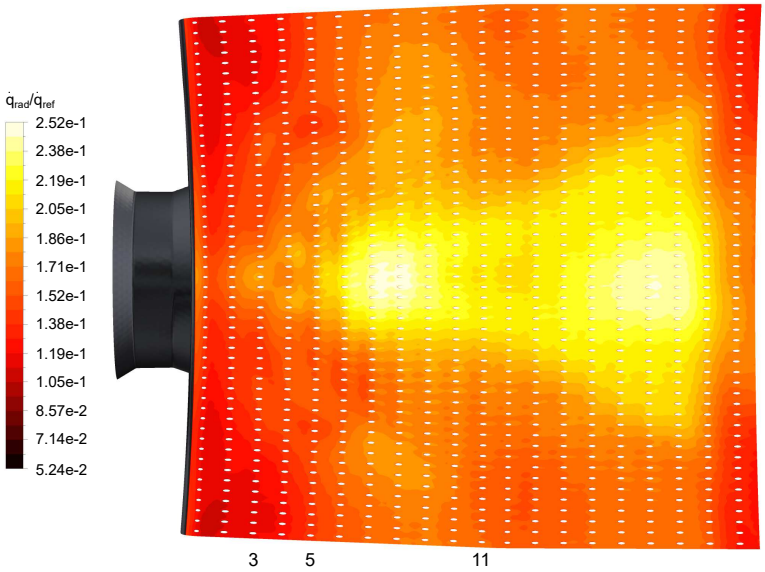

Figure 5.7: Absorbed radiative heat flux contours on the discharge side of the effusion wall with coarse radiation modelling and soot fouled walls.

These findings are supported by the plots of circumferentially averaged wall temperature in Figure 5.8. This clearly shows the substantial temperature increase due to soot fouling, which affects the entire liner. In reality, the liner wall is expected to be neither completely clean nor completely covered in soot. As such, a realistic solution would lie within the bounds of these two extreme cases. This has been represented by the shaded region in Figure 5.8.

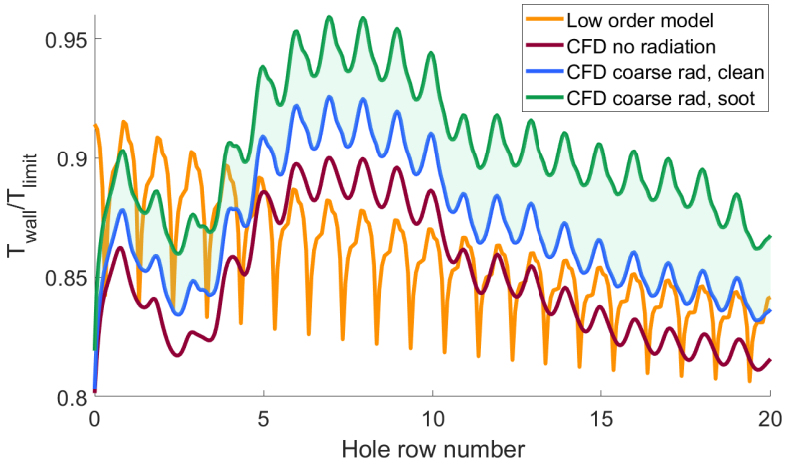

Figure 5.8: Circumferentially averaged temperature on the discharge side of the effusion wall showing sensitivity to liner emissivity.

5.4.3 Effect of DO Discretisation

The simulation with soot fouled walls was repeated with a fourfold increase in the number of control angles along which the DO RTE was integrated. While this could reasonably be expected to impact the plot of volumetric emission on the mid-plane, the results from this simulation were identical to those in Figure 5.2 above. As such, the figures have not been presented in this section.

Temperature contours are plotted on the discharge side of the effusion wall in Figure 5.9. This is practically identical to that produced by the coarse modelling, with an absolute maximum discrepancy under 0.5%. The increase in control angle count did not significantly change the temperature distribution or the size of the region of material limit exceedance. This suggests that the coarse radiation modelling was sufficient for the current work.

Contrary to this, the contours of radiative heat flux in Figure 5.10 are significantly different from those produced by the coarse modelling in Figure 5.7 above. As suspected, increasing the number of control angles resulted in a more diffused distribution of radiative heat flux. This resulted in a more intuitive radiative flux distribution, where the impact of exposure to the pilot flame is clear.

While the radiative flux was significantly altered by the increase in control angle count, Figure 5.9 showed that the liner temperature was not. This is explained through three observations. Firstly, the radiative flux contributes just

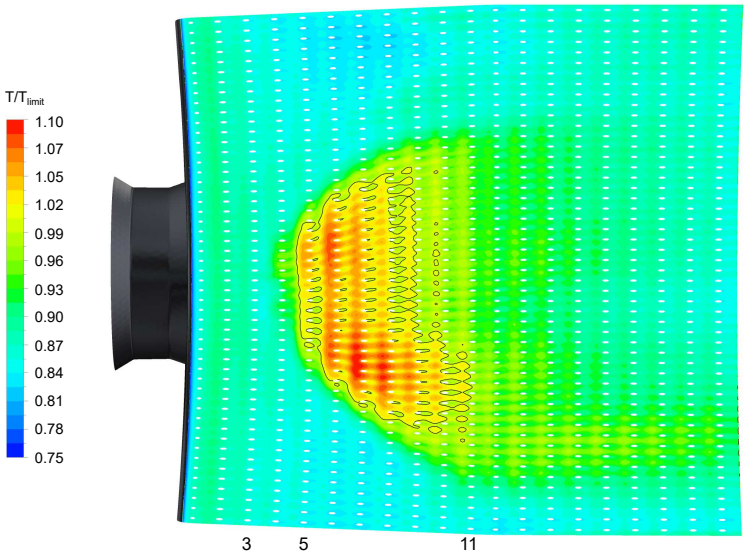

Figure 5.9: Temperature contours on the discharge side of the effusion wall with fine radiation modelling and soot covered walls.

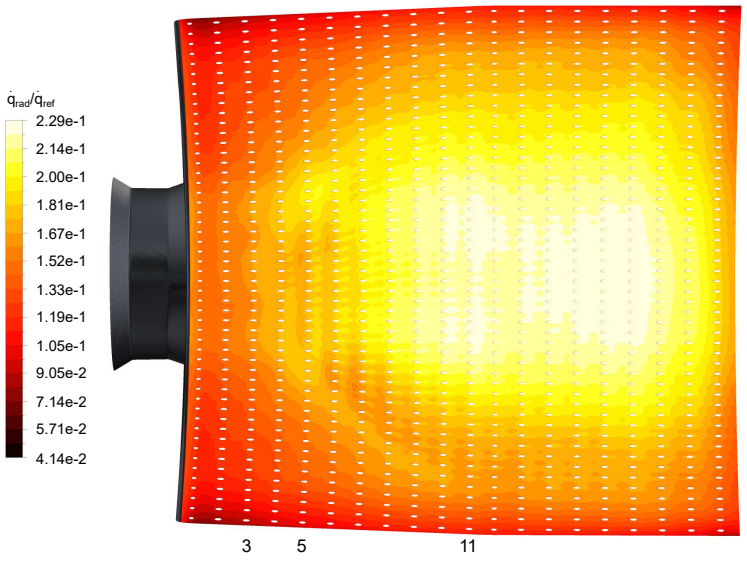

Figure 5.10: Radiative heat flux contours on the discharge side of the effusion wall with fine radiation modelling and soot covered walls.

33% of the total heat flux in this case. As such, variations to the flux distribution were not sufficient to significantly alter the temperature. Secondly, the total radiative energy transferred was conserved and equal in both cases, but more focussed along the centre line in the coarse case. As such, the total energy transfer into the liner was identical in both cases, albeit differently distributed. Finally, while the absorbed heat flux was more focussed in the coarse case, it was diffused through the liner wall by conduction. As such, the focussed streak of heat flux did not appear in the temperature contours. It should be noted, however, that in cases dominated by radiative heat transfer, or where the Biot number is high, a sensitivity to control angle count should be expected.

Circumferentially averaged wall temperature is plotted in Figure 5.11 with results from the coarse modelling overlaid. The mean discrepancy between the two solutions was in the order of 0.001%, reaffirming the insensitivity of liner temperature to control angle count in this case. It is therefore clear that the coarse modelling is sufficient for the work in this study.

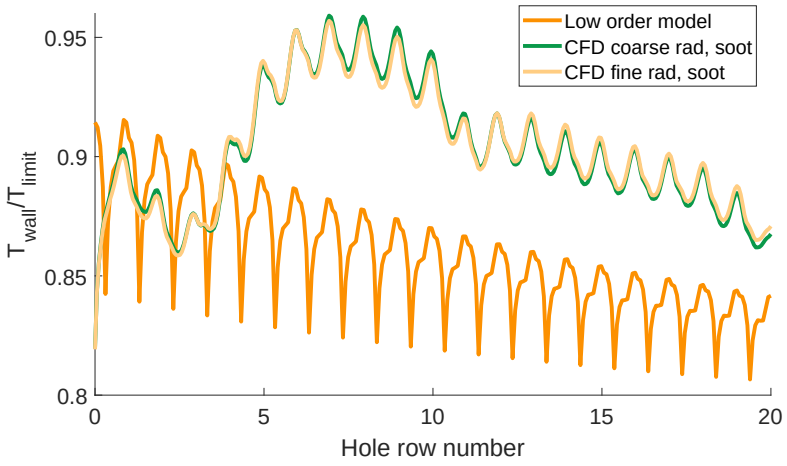

Figure 5.11: Circumferentially averaged temperature on the discharge side of the effusion wall showing sensitivity to DO discretisation.

5.5 Summary

The simulations described in Chapter 4 were repeated with the inclusion of radiation modelling. This facilitated understanding of the role of radiative heat transfer in the combustor under investigation. Further to this, the sensitivity to two key assumptions was assessed: the level of soot fouling on the inner liner walls and the number of control angles along which the DO RTE is integrated.

It was shown that radiative heat transfer contributed 15-33% of the total heat flux into the outer liner wall. This resulted in significant increases in liner temperature prediction, as well as an expansion of the region of material limit exceedance.

The increase in liner emissivity due to soot fouling resulted in a doubling of absorbed radiative flux. Soot fouling is incredibly difficult to predict, so only the extreme cases were analysed in order to bound the solution.

Finally, a fourfold increase in control angles, from the minimum of 32 to 128, had no significant impact on the solution. While the heat flux distribution was notably different, the total energy transfer was identical and flux distribution discrepancies were diffused by conduction. This would not, however, be the case if radiative heat transfer was the dominant mechanism, or if the Biot number was sufficiently high to prevent diffusion of the localised heating.

Chapter 6

Conclusions & Recommendations

6.1 Conclusions

In response to the research objectives posed in Section 1.3, the following conclusions are drawn.

Use of CHT CFD Simulations for Liner Temperature Prediction

The CHT CFD methodology has been shown to be a feasible means of making temperature predictions of an impingement/effusion cooled combustor liner. In Chapter 3 the method was used to replicate an experimental case, showing its validity and good predictive capability for this application. It was then successfully applied to a representative combustor case study in Chapters 4 and 5. Evidence of similar studies could not be found in literature.

While the application of this method was technically feasible, the practicality is questionable - particularly in the context of the preliminary design phase. The requirement for sufficient resolution in the liner gap led to very large cell counts - roughly an order larger than previous work in the overarching project. The practicality of this extreme computational cost at such an early stage in the design cycle must be considered.

The high fidelity simulations did, however, demonstrate value in revealing important interactions that could not be captured by low order modelling. Most significant was the deleterious effect of the swirling flow on the film cooling, as was shown experimentally by Andreini *et al.* (2017*b*) and others for the pure effusion case. In addition to this, the simulations revealed other areas of concern in the results produced by low order code, prompting further investigation. As such, the computational cost must be weighed against the potential contribution when assessing the practicality of implementing this method.

Impact of Boundary Layer Treatment on Liner Wall Temperature Predictions

A detailed mesh sensitivity study in Chapter 3 revealed that the inclusion of an inflation layer did not substantially improve predictive capability when analysing the temperature of an impingement/effusion cooled wall. This is fortuitous, as previous work in the overarching project had been carried out without the inclusion of inflation layers. Furthermore, it resulted in a significant reduction in cell count, thereby decreasing the computational cost.

It was shown that the requirement for acceptable hole resolution resulted in sufficiently small values of y^+ that the EWT blending was still significantly biased toward the low Reynolds solution. Wall function performance was therefore not assessed in the current study. While the study of Mazzoni *et al.* (2015) suggested that wall functions had high predictive capability for similar applications, it was carried out on a non-commercial code. As such, the y^+ value of existing and future simulations should be scrutinised and the suitability of wall functions should be assessed if implemented.

Mesh Resolution Trade-off

In addition to near wall resolution, the systematic mesh resolution study in Chapter 3 investigated the sensitivity to resolution of the cooling holes and the gap between the walls. Further to this, the selection of meshing topology was assessed. This was undertaken with the intention of finding a compromise between computational cost and predictive capability.

It was found that little compromise in gap resolution could be attained. Using 10 cells to span the gap produced results which compared well with experimental data, but fewer cells failed to converge.

When assessing mesh topology, it was found that polyhedral cells were unsuitable for this problem unless an inflation layer was used. The requirement of an inflation layer for near wall resolution increased the computational cost. As such, polyhedra were not found to be the optimal solution in this case.

Reasonable compromise was found with reduction in cooling hole resolution. For the experimental case, it was found that 18 cells resolving the circumference of each hole yielded the optimal trade-off.

The result of the trade-off study was a meshing methodology with a computational cost of under 10% of the benchmark case, and an increase in mean square error of under 1.5%. This was shown to be the optimal trade-off between computational cost and predictive capability.

Impact of Radiation Modelling

The impact of radiation modelling was assessed in Chapter 5, addressing a significant gap in literature. This study showed that radiation modelling should be included when conducting CHT CFD simulations for the purpose of liner temperature prediction. While radiation is not the dominant heat transfer mechanism,

its inclusion resulted in a 6.4% increase of average liner temperature. As such, neglecting radiation is a non-conservative assumption which would have a negative impact on the design optimisation process.

It was further shown that there is a severe sensitivity to liner emissivity, which cannot be accurately estimated at the preliminary design stage. As such, it is recommended that the extreme cases be studied to band a feasible solution until soot fouling can be reliably modelled.

Finally, it was shown that two angular divisions per octant and one pixel in each angular direction provided sufficient resolution for the DO equations in this case. While the radiative flux distribution was artificially concentrated, this had minimal impact on the liner temperature distribution. It was noted that this will not be the case if radiative heat flux is the dominant heat transfer mechanism, or if liner conduction is insufficient to diffuse the concentrated radiative flux.

In addition to these findings, it was noted that the inclusion of radiative heat transfer had negligible impact on the combusting flow field. As such, it is not necessary to include this unless the objective of the simulation is liner temperature prediction.

6.2 Future Work

The following work is recommended to correct, improve or expand on the current study:

1. Future simulations should attempt to resolve both walls. If this is not feasible, it is recommended that more detail be included at the non-resolved wall:

    a) The temperature distribution should be more accurately described in order to capture hot spots which will be strong radiation sources. The CHT results from previous simulations could be used to define temperature profiles for the non-resolved boundary.

    b) The coolant discharge through the wall not being resolved should be accounted for, as it impacts the temperature distribution in the combustor. This could be modelled as a series of mass flow inlets at the non-resolved wall boundary.

2. The sensitivity to all assumed thermal boundary conditions should be investigated.

    a) It is recommended that detail of the snout and dome be included to account for the thermal interaction with these components. This would remove the need for the boundary condition at the liner leading edge, which induced an unquantified error in the current work.

    b) The temperature at the liner trailing edge should be estimated, including the effect of conduction to external components. This would

remove the adiabatic boundary condition which induced an unquantified error in the current work.

3. The impact of omitting swirler detail should be investigated. This can be performed without resolving liner cooling to make the problem computationally tractable. The results could inform more realistic swirler inlet conditions for future simulations.

4. The mesh dependency study in Chapter 3 should be repeated for the combustor geometry. This will highlight any case-specific sensitivities which were not found in the current work.

5. The value used for the diffuse fraction of a typical Hastelloy X combustor liner with a thermally oxidised surface should be verified. Further to this, a sensitivity study should be preformed on this parameter.

6. The impact of incorporating a temperature dependent viscosity model should be investigated. It is recommended that high temperature viscosity data be collected for each of the species, allowing a piecewise linear or polynomial relationship to be defined. The viscosity of the mixture can then be modelled as the mass weighted average of the constituent viscosities.

7. Further investigation into the source-sink method should be undertaken to reconcile this method with the FGM combustion model. While the mesh count will still be dominated by resolution in the wall gap, the removal of cooling hole detail will simplify the geometry and mesh preparation process, as well as reducing the cell count somewhat. This may make the high fidelity analysis more practical for inclusion in the multi-fidelity optimisation process.

8. The root cause for the incompatibility of k-ω SST and the FGM combustion model should be investigated in order to circumvent this. If compatibility can be achieved, the current simulations should be repeated using k-ω SST, as it has been shown to be more accurate in predicting wall temperatures.

9. The predictive capability of wall functions should be investigated in the context of CHT simulations of impingement/effusion cooled walls. This would provide better understanding of the allowable range of y^+ values for these simulations.

10. Soot formation and deposition should be included in the high fidelity simulations. While the state of the art is currently limited to empirical modelling, it is rapidly progressing. This prompts further investigation into including this in the multiphysics simulation, though validation may require additional experimental work.

11. The effect of unsteady modelling should be assessed. The study of Hwang *et al.* (2016), discussed in Chapter 2, suggested that unsteady effects have a significant impact on the cooling performance.

12. The solid body temperatures obtained from the CHT CFD analysis should be transferred to an FEA simulation to assess the mechanical impact. This would allow conclusions to be drawn regarding thermal stress and provide inputs into the fatigue life model of the optimisation tool.

13. In future studies, it should be noted that the number of energy iterations per DO iteration can be decreased to achieve quicker convergence. This may, however, lead to solution instability. If many simulations are to be performed, the lowest stable value should be found.

6.3 Improvements to Low Order Model

In addition to the above recommendations, the following improvements to the low order modelling suite are proposed. These proposals are based on the findings from the CFD simulations, and should be used to improve the fidelity of the low order model. Following the update of the low order code, optimisation studies should be repeated to assess the impact of this update on the Pareto front.

Firstly, improvements to the near wall velocity model are recommended. The low order model currently assumes bulk fluid velocity throughout the length of the liner wall. The most important phenomenon not captured due to this assumption is swirl impingement. It is recommended that a physics-based model for the spread rate of the swirling jet be built. This would facilitate prediction of the impingement region, in which the near wall velocity could be set to that of the swirling jet. This would assist in capturing the increased convective heat transfer in this region. While the disturbance of the cooling film would not be modelled, the predictive capability of the low order model would likely be improved.

In addition to the above, the current near wall velocity model did not capture the velocity deficiency near the dome. In fact, the CFD results show almost zero bulk fluid velocity between the dome and the swirl impingement point. As such, once the impingement point is predicted, the near wall velocity model can be updated to reflect this.

The pressure drop calculation across the impingement/effusion cooled wall should be investigated and refined, if possible. If the current approach cannot be improved with analytical methods, it is recommended that sufficient data be collected to build a case-specific empirical model for impingement/effusion walls. The data could be collected experimentally or numerically.

Finally, the convective, conductive and radiative heat fluxes should be investigated to determine the root cause of the Biot number discrepancy. This is vital, as the steep thermal gradients predicted by the low order model will result in artificially high thermal stresses and reduced fatigue life predictions. If left unresolved, this would lead to an over-designed liner at the end of the optimisation process. To assist with this process, circumferentially averaged plots of heat transfer data are provided in Appendix B.

Appendices

Appendix A

Material Properties

A.1 Validation Study

The material properties for stainless steel AISI 304 used in the validation study are summarised in Table A.1.

Table A.1: Material properties of AISI 304

Property	Unit	Value
Density	$\mathrm{kg\,m^{-3}}$	7900
Specific Heat	$\mathrm{J\,kg^{-1}\,K^{-1}}$	500
Thermal Conductivity	$\mathrm{W\,m^{-1}\,K^{-1}}$	13.5

A.2 Combustor Case Study

The material property relations used to model the combustion gas are summarised in Table A.2.

Table A.2: Summary of combustion gas material modelling

Property	Dependencies	Value / Model
Density	Temperature	Incompressible ideal gas
Emissivity	Temperature, composition	WSGG
Viscosity	None	2.5e-5 $[\mathrm{kg\,m^{-1}\,s^{-1}}]$
Specific heat	Composition	Mixing law
Thermal conductivity	Temperature, composition	Mixing law

The temperature dependent material properties for the Hasteloy X liner are given in Table A.3.

Table A.3: Temperature dependent material properties of Haselloy X

T [K]	ρ^1 [kg m^{-3}]	$C_p{}^1$ [J kg^{-1} K^{-1}]	k^1 [W m^{-1} K^{-1}]	ε^2 [-]
298	8240	439	10.3	0.230
373	8221	454	11.5	0.235
473	8193	473	13.2	0.242
573	8162	493	15.0	0.265
673	8130	512	16.9	0.293
773	8095	532	18.8	0.321
873	8058	551	20.9	0.349
973	8019	582	22.8	0.378
1073	7978	604	23.8	0.409
1173	7934	626	25.9	0.559
1273	7889	648	28.0	0.650
1373	7841	670	30.2	-
1473	7792	692	32.4	-
1533	7761	710	33.7	-

[1] Obtained from Mills (2002).
[2] Obtained from Maynard *et al.* (2010).

Appendix B

Additional Plots

Averaged Heat Flux Summary

To assist with the investigation into discrepancies between the high and low order analyses, additional plots are provided below. Circumferentially averaged plots of convective and radiative flux, as well as wall temperature are provided. These plots have been created for both the suction and discharge sides of the impingement wall in Figures B.1 and B.2, and for the effusion wall in Figures B.3 and B.4. The data presented have been taken from simulations without soot fouling, as the effects of soot fouling were not accounted for in the low order model.

Care should be taken when dealing with the values at the leading and trailing edges, as these have been impacted by unrealistic boundary conditions. Further to this, node-averaging was employed when generating these plots. As such, the exact values at the extremities have not been captured. This is particularly clear at the trailing edges, where heat flux appears to have a non-zero value in spite of the adiabatic boundary condition.

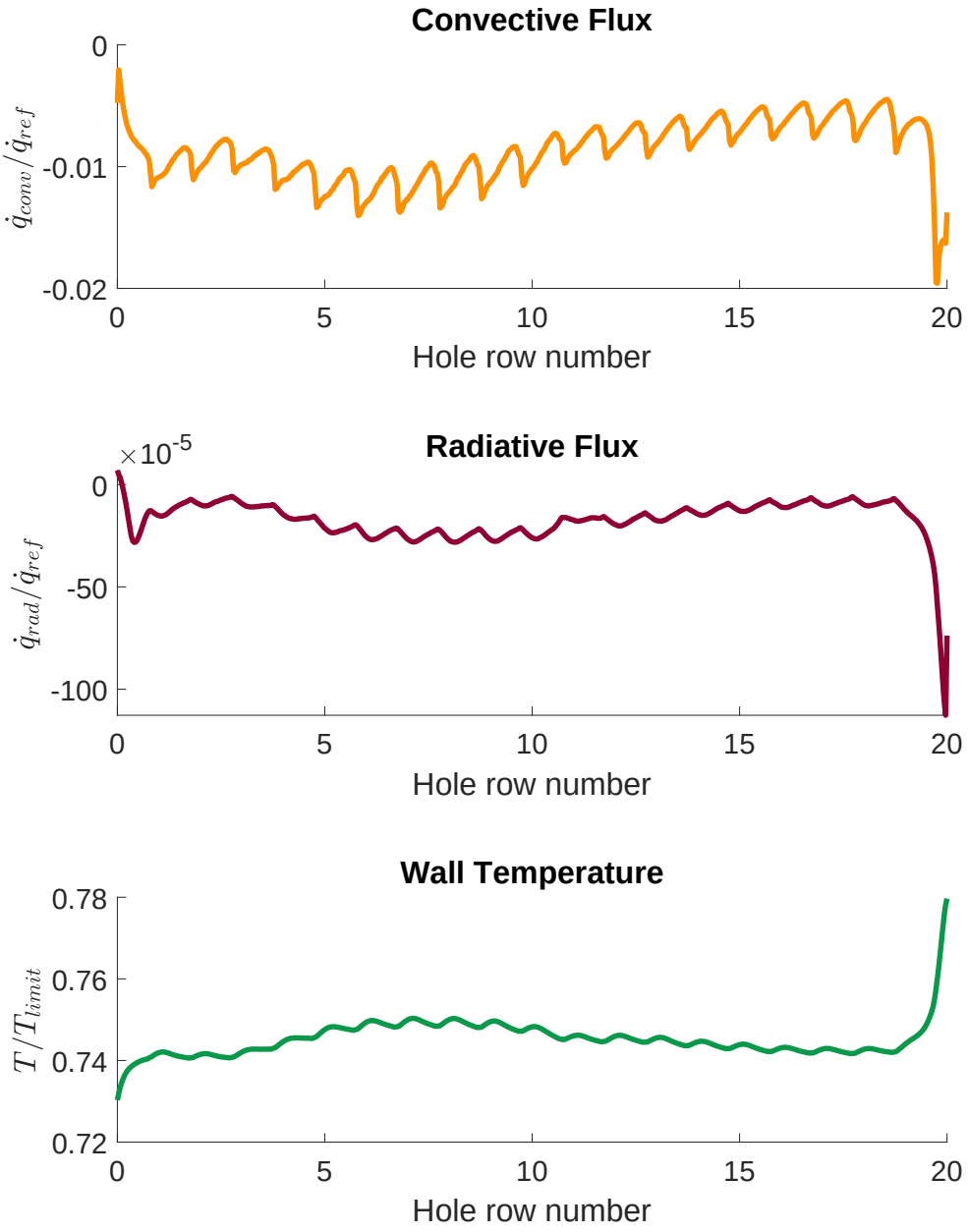

Figure B.1: Circumferentially averaged thermodynamic quantities on the suction side of the impingement wall.

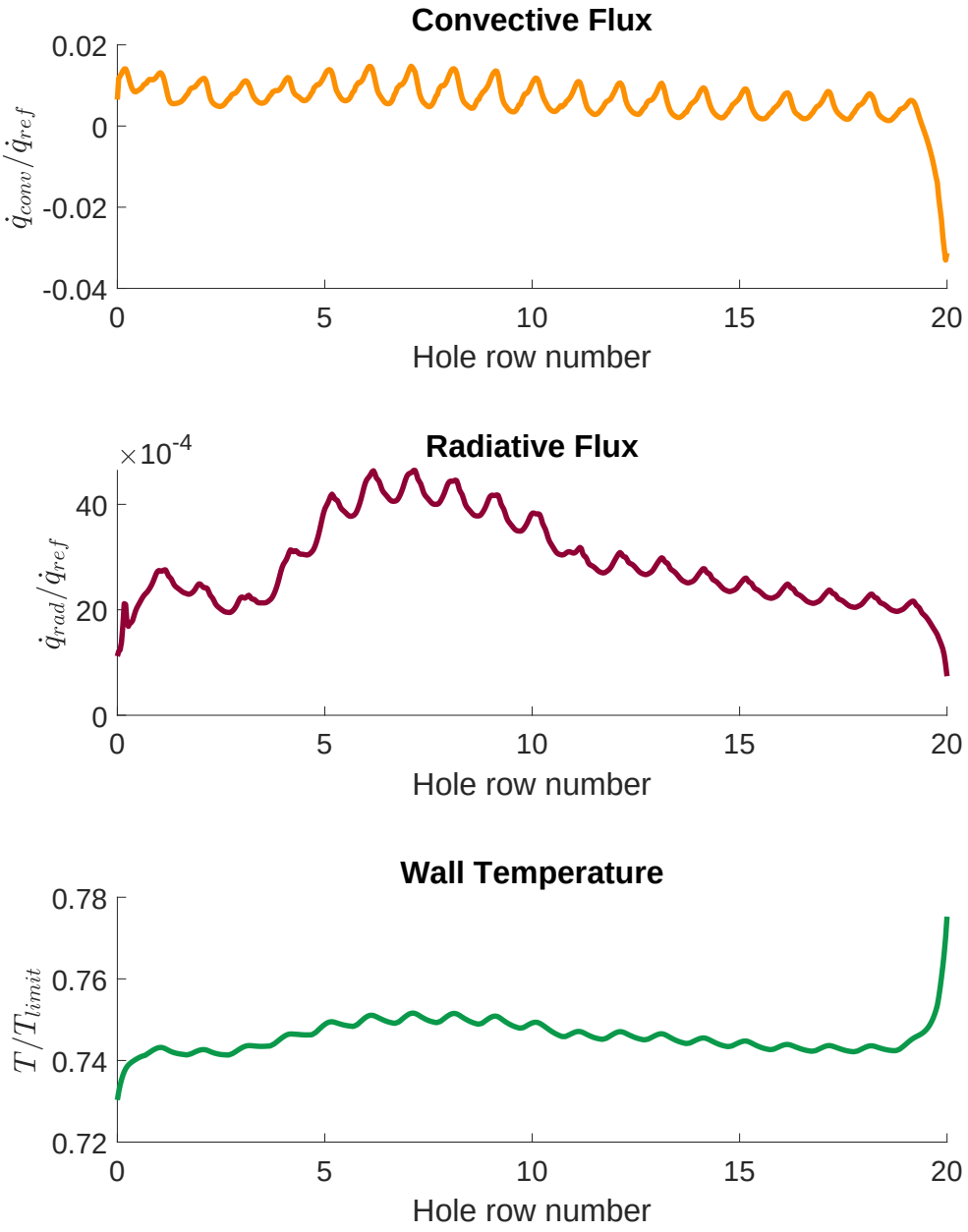

Figure B.2: Circumferentially averaged thermodynamic quantities on the discharge side of the impingement wall.

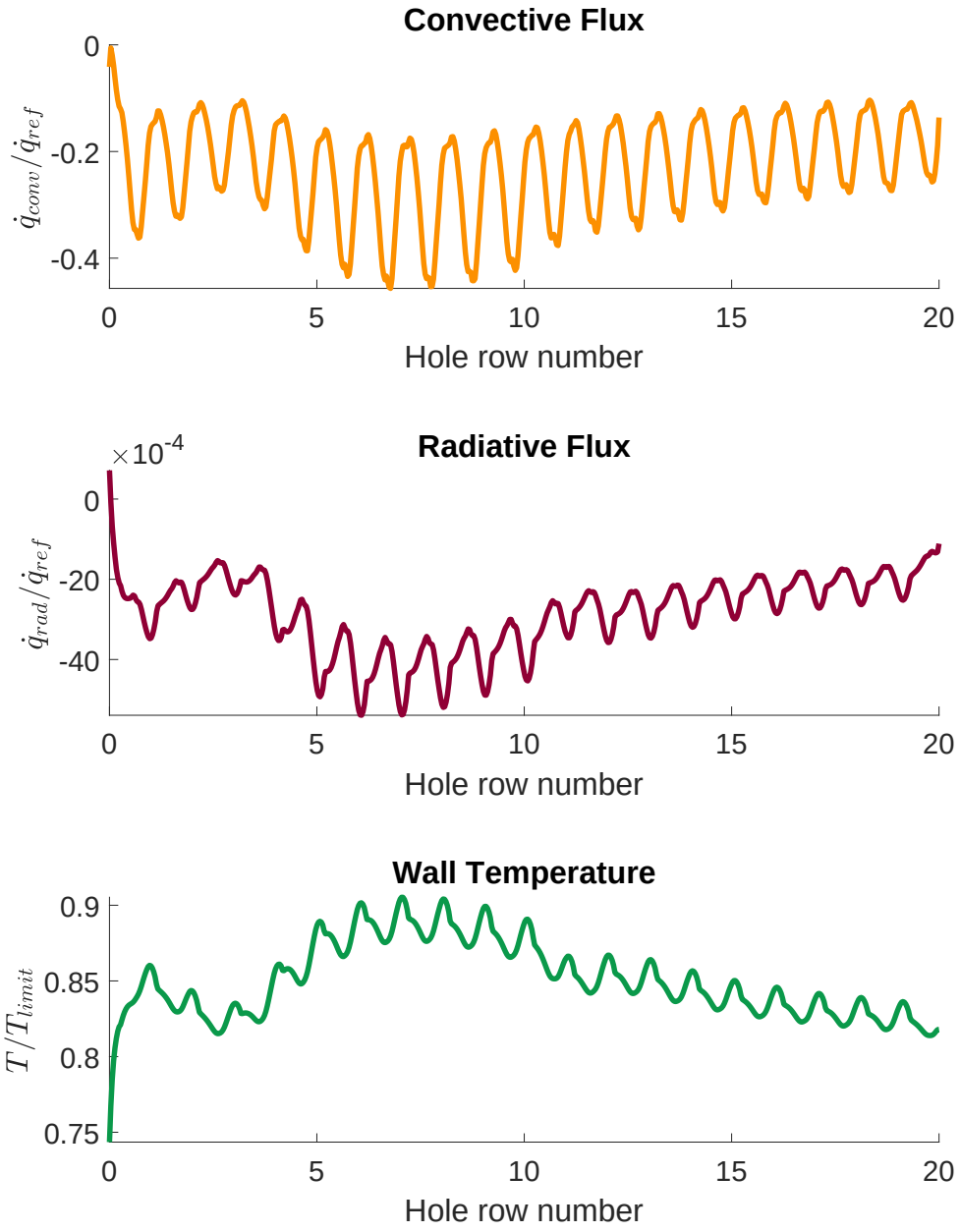

Figure B.3: Circumferentially averaged thermodynamic quantities on the suction side of the effusion wall.

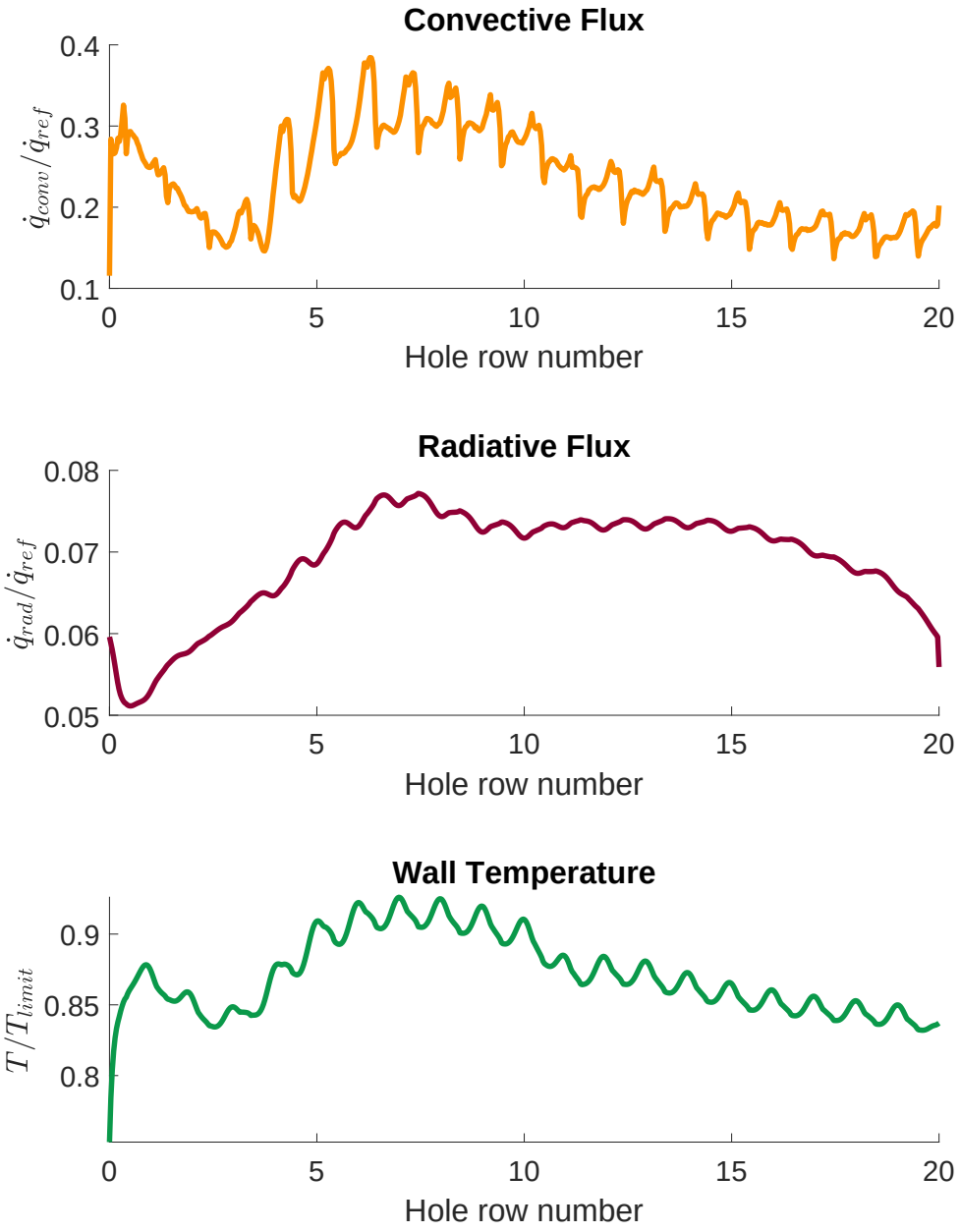

Figure B.4: Circumferentially averaged thermodynamic quantities on the discharge side of the effusion wall.

List of References

Andreini, A., Becchi, R., Facchini, B., Mazzei, L., Picchi, A. and Turrini, F. (2015*a*). Adiabatic Effectiveness and Flow Field Measurements in a Realistic Effusion Cooled Lean Burn Combustor. *Journal of Engineering for Gas Turbines and Power*, vol. 138, no. 3, p. 031506. ISSN 0742-4795.

Andreini, A., Becchi, R., Facchini, B., Mazzei, L., Picchi, A., Vitale, I. and Tolpadi, A. (2017*a*). Experimental & Numerical Investigation of the Mutual Interaction Between Liner Film Cooling & Combustor Swirl Flow. *Proceedings of the ASME Turbo Expo*, vol. 5C-2017, pp. 1–13.

Andreini, A., Becchi, R., Facchini, B., Picchi, A. and Peschiulli, A. (2017*b*). The Effect of Effusion Holes Inclination Angle on the Adiabatic Film Cooling Effectiveness in a Three-Sector Gas Turbine Combustor Rig with a Realistic Swirling Flow. *International Journal of Thermal Sciences*, vol. 121, no. x, pp. 75–88. ISSN 12900729.

Andreini, A., Bertini, D., Facchini, B. and Puggelli, S. (2015*b*). Large-Eddy Simulation of a turbulent spray flame using the flamelet generated manifold approach. *Energy Procedia*, vol. 82, pp. 395–401.

Andreini, A., Cocchi, L., Facchini, B., Mazzei, L. and Picchi, A. (2018). Experimental and Numerical Investigation on the Role of Holes Arrangement on the Heat Transfer in Impingement/Effusion Cooling Schemes. *International Journal of Heat and Mass Transfer*, vol. 127, pp. 645–659. ISSN 00179310.

Andreini, A., Da Soghe, R., Facchini, B., Mazzei, L., Colantuoni, S. and Turrini, F. (2013). Local Source Based CFD Modeling of Effusion Cooling Holes: Validation and Application to an Actual Combustor Test Case. *Journal of Engineering for Gas Turbines and Power*, vol. 136, no. 1. ISSN 0742-4795.

ANSYS (2019*a*). *ANSYS Fluent Theory Guide*. ANSYS, Inc.

ANSYS (2019*b*). *ANSYS Fluent Users Guide*. ANSYS, Inc.

Bahador, M. and Sundén, B. (2006). A Conjugate Heat Transfer Model for Heat Load Prediction in Combustion Devices. *AIAA/ASME Joint Thermophysics and Heat Transfer Conference 2006*.

Bailey, J.C., Intile, J., Fric, T.F., Tolpadi, A.K., Nirmalan, N.V. and Bunker, R.S. (2002). Experimental and Numerical Study of Heat Transfer in a Gas Turbine Combustor Liner. *Journal of Engineering for Gas Turbines and Power*, vol. 125, no. October 2003, pp. 994–1002. ISSN 07424795.

Crocker, D.S., Nickolaus, D.A. and Smith, C.E. (2000). Piloted Airblast Lean Direct Fuel Injector.

Da Soghe, R., Bianchini, C., Andreini, A., Mazzei, L., Riccio, G. and Marini, A. (2016). Metal Temperature Prediction of a Dry Low NO x Class Flame Tube by Computational Fluid Dynamics Conjugate Heat Transfer Approach. *Journal of Engineering for Gas Turbines and Power*, vol. 138, no. 3. ISSN 0742-4795.

Dauptain, A. and Duchaine, F. (2017). Large Eddy Simulation of Conjugate Heat Transfer Around a Multi-Perforated Plate with Deviation. *Proceedings of ASME Turbo Expo 2017*.

De Santis, A., Ingham, D.B., Ma, L. and Pourkashanian, M. (2016). CFD Analysis of Exhaust Gas Recirculation in a Micro Gas Turbine Combustor for CO2 Capture. *Fuel*, vol. 173, pp. 146–154. ISSN 00162361.

Donachie, M.J. and Donachie, S.J. (2002). *Superalloys: A Technical Guide*. ASM International.

El-Jummah, A.M., Abdul Husain, R.A.A., Andrews, G.E. and Staggs, J.E.J. (2014). Conjugate Heat Transfer Computational Fluid Dynamic Predictions of Impingement Heat Transfer: The Influence of the Number of Holes for a Constant Pitche-to-Diameter Ratio. *Proceedings of ASME Turbo Expo 2014*. ISSN 0889-504X.

El-jummah, A.M., Andrews, G.E. and Staggs, J.E.J. (2013). Conjugate Heat Transfer CFD Predictions of Impingement Jet Array Flat Wall Cooling Aerodynamics with Single Sided Flow Exit. *Proceedings of ASME Turbo Expo 2013*.

El-jummah, A.M., Andrews, G.E. and Staggs, J.E.J. (2016). Impingement/Effusion Cooling Wall Heat Transfer: Conjugate Heat Transfer Computational Fluid Dynamic Predictions. *Proceedings of ASME Turbo Expo 2016*.

Gauthier, P. (2019). Personal Communication, Royal Academy of Engineering Visiting Professor of Low Emissions Combustion Modelling, Cranfield University, Bedfordshire, United Kingdom.

Ge, B., Ji, Y., Chi, Z. and Zang, S. (2017). Effusion CoolingCharacteristics of a Model Combustor Liner at Non-Reacting/Reacting Flow Conditions. *Applied Thermal Engineering*, vol. 113, pp. 902–911. ISSN 13594311.

Gent, G. (2018). *3D CFD Conjugate Heat Transfer Analysis of the Cooling System of an LDI Combustor*. Ph.D. thesis, Cranfield University.

Guildenbecher, D., López-Rivera, C. and Sojka, P. (2009 03). Secondary atomization. *Experiments in Fluids*, vol. 46, pp. 371–402.

Hossainpour, S. and Binesh, A.R. (2009). Investigation of fuel spray atomization in a DI heavy-duty diesel engine and comparison of various spray breakup models. *Fuel*, vol. 88, no. 5, pp. 799–805. ISSN 0016-2361.
Available at: `http://dx.doi.org/10.1016/j.fuel.2008.10.036`

Hwang, S., Son, C., Seo, D., Rhee, D.H. and Cha, B. (2016). Comparative Study on Steady and Unsteady Conjugate Heat Transfer Analysis of a High Pressure Turbine Blade. *Applied Thermal Engineering*, vol. 99, pp. 765–775. ISSN 13594311.

Jaure, S., Duchaine, F., Staffelbach, G. and Gicquel, L.Y. (2013). Massively Parallel Conjugate Geat Transfer Methods Relying on Large Eddy Simulation Applied to an Aeronautical Combustor. *Computational Science and Discovery*, vol. 6, no. 1. ISSN 17494680.

Jeromin, A., Eichler, C., Noll, B. and Aigner, M. (2008). Full 3D Conjugate Heat Transfer Simulation and Heat Transfer Coefficient Prediction for the Effusion-Cooled Wall of a Gas Turbine Combustor. *Proceedings of ASME Turbo Expo 2008*.

Ji, Y., Ge, B., Chi, Z. and Zang, S. (2018). Overall Cooling Effectiveness of Effusion CooledAnnular Combustor Liner at Reacting Flow Conditions. *Applied Thermal Engineering*, vol. 130, pp. 877–888. ISSN 13594311.

Johansson, R., Leckner, B., Andersson, K. and Johnsson, F. (2011). Account for Variations in the H2O to CO2 Molar Ratio When Modelling Gaseous Radiative Heat Transfer with the Weighted-Sum-of-Grey-Gases Model. *Combustion and Flame*, vol. 158, no. 5, pp. 893–901. ISSN 00102180.

Jones, W.P. and Paul, M.C. (2005). Combination of DOM with LES in a Gas Turbine Combustor. *International Journal of Engineering Science*, vol. 43, no. 5, pp. 379–397.

Jung, E.Y., Chung, H., Choi, S.M., Woo, T.-k. and Cho, H.H. (2017). Conjugate Heat Transfer on Full-Coverage Film Cooling With Array Fet Impingements with Various Biot Numbers. *Experimental Thermal and Fluid Science*, vol. 83, pp. 1–8. ISSN 0894-1777.

Kim, K.M., Moon, H., Park, J.S. and Cho, H.H. (2014). Optimal Design of Impinging Jets in an Impingement/Effusion Cooling System. *Energy*, vol. 66, pp. 839–848. ISSN 03605442.

Kuo, K.K. (2005). *Principles of Combustion*. 2nd edn. John Wiley & Sons. ISBN 0-471-04689-2.

Lefebvre, A.H. and Ballal, D.R. (2010). *Gas Turbine Combustion: Alternate Fuels and Emissions*. 3rd edn. CRC Press. ISBN 978-1-4200-8604-1.

Ligrani, P., Ren, Z., Liberatore, F., Patel, R., Srinivasan, R. and Ho, Y.-H. (2017). Double Wall Cooling of a Full-Coverage Effusion Plate, Including Internal Impingement Array Cooling. *Journal of Engineering for Gas Turbines and Power*, vol. 140, no. 5, p. 051901. ISSN 0742-4795.

Ligrani, P., Ren, Z., Vanga, S.R., Allgaier, C., Liberatore, F., Patel, R., Srinivasan, R. and Ho, Y.-H. (2018). Double Wall Cooling of a Full Coverage Effusion Plate With Cross Flow Supply Cooling and Main Flow Pressure Gradient. *Journal of Engineering for Gas Turbines and Power*, vol. 141, no. 3, p. 031015. ISSN 0742-4795.

Liu, C., Xie, G., Wang, R. and Ye, L. (2018). Study on Analogy Principle of Overall Cooling Effectiveness for Composite Cooling Structures with Impingement and Effusion. *International Journal of Heat and Mass Transfer*, vol. 127, pp. 639–650. ISSN 0017-9310.

Liu, Y. (2018). *Development of Preliminary Design and Optimisation Methodology of a Low Emissions Combustor for Civil Application*. Ph.D. thesis, Cranfield University, Cranfield, UK.

Maynard, R.K., Tushar K. Ghos and, R.V.T., Viswanath, D.S. and Loyalka, S.K. (2010). Total hemispherical emissivity of potential structural materials for very high temperature reactor systems: Hastelloy x. *Nuclear Technology*, vol. 172, no. 1.

Mazzei, L., Picchi, A., Andreini, A., Facchini, B. and Vitale, I. (2017). Unsteady CFD Investigation of Effusion Cooling Process in a Lean Burn Aero-Engine Combustor. *Journal of Engineering for Gas Turbines and Power*, vol. 139. ISSN 0742-4795.

Mazzoni, C.M., Luque, S. and Rosic, B. (2015). Capabilities of Thermal Wall Functions To Predict Heat Transfer on the NGVs of a Gas Turbine with Multiple Can Combustors. *Proceedings of ASME Turbo Expo 2015*, pp. 1–12. ISSN 1385-3449.

Mills, K.C. (2002). *Recommended Values of Thermophysical Properties for Selected Commercial Alloys*. Woodhead Publishing.

Modest, M.F. (2013). *Radiative Heat Transfer*. 3rd edn. Elsevier.

NREC (1980). *The Design and Development of Gas Turbine Combustors Volume I: Component Theory and Practice*. Northern Research and Engineering Corporation.

Oijen, J.A.V., Donini, A., Bastiaans, R.J.M., Boonkkamp, J.H.M.T. and Goey, L.P.H.D. (2016). State-of-the-art in premixed combustion modeling using flamelet generated manifolds. *Progress in Energy and Combustion Science*, vol. 57, pp. 30–74. ISSN 0360-1285.
Available at: `http://dx.doi.org/10.1016/j.pecs.2016.07.001`

Paul, M.C. and Jones, W.P. (2006). Radiative Heat Transfer in a Model Gas Turbine Combustor. *WIT Transactions on Engineering Sciences*, vol. 53, pp. 413–421. ISSN 17433533.

Piskin, A. and Topal, A. (2016). Coupled CFD and Heat Transfer Analysis for a Small Scale Gas Turbine Combustor. *Proceedings of ASME Turbo Expo 2016*.

Porter, R., Liu, F., Pourkashanian, M., Williams, A. and Smith, D. (2010). Evaluation of Solution Methods for Radiative Heat Transfer in Gaseous Oxy-Fuel Combustion Environments. *Journal of Quantitative Spectroscopy and Radiative Transfer*, vol. 111, no. 14, pp. 2084–2094. ISSN 00224073.

Proch, F. and Kempf, A.M. (2015). ScienceDirect Modeling heat loss effects in the large eddy simulation of a model gas turbine combustor with premixed flamelet generated manifolds. *Proceedings of the Combustion Institute*, vol. 35, no. 3, pp. 3337–3345. ISSN 1540-7489.
Available at: `http://dx.doi.org/10.1016/j.proci.2014.07.036`

Puggelli, S., Bertini, D., Mazzei, L. and Andreini, A. (2016). Scale Adaptive Simulations of a swirl stabilized spray flame using Flamelet Generated Manifold. *Energy Procedia*, vol. 101, no. September, pp. 1143–1150. ISSN 1876-6102.
Available at: `http://dx.doi.org/10.1016/j.egypro.2016.11.155`

Rogers, N., Ren, Z., Buzzard, W., Sweeney, B., Tinker, N., Ligrani, P., Hollingsworth, K., Liberatore, F., Patel, R., Ho, S. and Moon, H.-K. (2017). Effects of Double Wall Cooling Configuration and Conditions on Performance of Full-Coverage Effusion Cooling. *Journal of Turbomachinery*, vol. 139, no. 5, p. 051009. ISSN 0889-504X.

Saravanamuttoo, H., Rogers, G. and Cohen, H. (2006). *Gas Turbine Theory*. Fith edn. Pearson Education.

Saygin, Y., Can Kocaman, O. and Uslu, S. (2016). Effect of Radiation on Gas Turbine Combustor Liner Temperature with Conjugate Heat Transfer (CHT) Methodology. *52nd AIAA/SAE/ASEE Joint Propulsion Conference*. ISSN 2295-3337.

Shrager, A.C., Thole, K.A. and Mongillo, D. (2018*a*). Effects of Effusion Cooling Pattern Near the Dilution Hole for a Double-Walled Combustor Liner - Part 1: Overall Effectiveness Measurements. *ASME Paper No. GT2018-77288*, pp. 1–10. ISSN 15288919.

Shrager, A.C., Thole, K.A. and Mongillo, D. (2018*b*). Effects of Effusion Cooling Pattern Near the Dilution Hole for a Double-Walled Combustor Liner - Part 2: Flowfield Measurements. *ASME Paper No. GT2018-77288*, vol. 141, no. January, pp. 1–10. ISSN 15288919.

Singh, P. and Ekkad, S.V. (2017). Effects of Spent Air Removal Scheme on Internal-Side Heat Transfer in an Impingement-Effusion System at Low Jet-to-Target Plate Spacing. *International Journal of Heat and Mass Transfer*, vol. 108, pp. 998–1010. ISSN 00179310.

Sun, X. (2018). *Application of CFD Zooming for Preliminary Design of a Low Emissions Combustor*. Ph.D. thesis, Cranfield University, Cranfield, UK.

Vié, A., Franzelli, B., Gao, Y., Lu, T., Wang, H. and Ihme, M. (2015). Analysis of Segregation and Bifurcation in Turbulent Spray Flames: A 3D Counterflow Configuration. *Proceedings of the Combustion Institute*, vol. 35, no. 2, pp. 1675–1683.

Wang, P., Fan, F. and Li, Q. (2014). Accuracy Evaluation of the Gray Gas Radiation Model in CFD Simulation. *Case Studies in Thermal Engineering*, vol. 3, pp. 51–58. ISSN 2214157X.

Warnatz, J., Maas, U. and Dibble, R.W. (2006). *J. Warnatz · U. Maas · R.W. Dibble Combustion*. ISBN 9783540259923.

Xiao-ming, T., Jing-zhou, Z. and Hua-sheng, X. (2015). Experimental Investigation on Impingement/Effusion Cooling with Short Normal Injection Holes. *International Communications in Heat and Mass Transfer*, vol. 69, pp. 1–10. ISSN 0735-1933.